

ÇUKUROVA UNIVERSITY
INSTITUTE OF NATURAL AND APPLIED SCIENCES

M. Sc. THESIS

Çetin CANPOLAT

Vortex Formation over a Nonslender Delta Wing

DEPARTMENT OF MECHANICAL ENGINEERING

ADANA, 2008

ÇUKUROVA ÜNİVERSİTESİ
FEN BİLİMLERİ ENSTİTÜSÜ

VORTEX FORMATION OVER A NONSLENDER DELTA WING

Çetin CANPOLAT

YÜKSEK LİSANS TEZİ

MAKİNA MÜHENDİSLİĞİ ANABİLİMDALI

**Bu tez/...../2008 Tarihinde Aşağıdaki Jüri Üyeleri Tarafından
Oybirliği/Oyçokluğu ile Kabul Edilmiştir.**

İmza:.....İmza:.....İmza:.....
Prof.Dr. Beşir ŞAHİN Doç.Dr. Hüseyin AKILLI Doç.Dr. Galip SEÇKİN
DANIŞMAN ÜYE ÜYE

Bu tez Enstitümüz Makine Mühendisliği Anabilim Dalında Hazırlanmıştır
Kod. No:

Prof. Dr. Aziz ERTUNÇ
Enstitü Müdürü

**Bu Çalışma Türkiye Bilimsel ve Teknolojik Araştırma Kurumu (TÜBİTAK)
tarafından desteklenmiştir. Proje No: 105M225**

Not: Bu tezde kullanılan özgün ve başka kaynaktan yapılan bildirişlerin, çizelge, şekil ve fotoğrafların
kaynak gösterilmeden kullanımı, 5486 sayılı Fikir ve Sanat Eserleri Kanunundaki Hükümlere tabidir

ABSTRACT
M. Sc. THESIS

VORTEX FORMATION OVER A NONSLENDER DELTA WING

Çetin CANPOLAT

**DEPARTMENT OF MECHANICAL ENGINEERING
INSTITUTE OF NATURAL AND APPLIED SCIENCES
UNIVERSITY OF ÇUKUROVA**

Supervisor : Prof. Dr. Beşir ŞAHİN
Year : 2008, Pages:101
Jury : Prof. Dr. Beşir ŞAHİN
Assoc. Prof. Dr. Hüseyin AKILLI
Assoc. Prof. Dr. Galip SEÇKİN

In this work, vortical flow structure of a delta wing of low sweep angle was investigated both qualitatively and quantitatively using dye visualization and a laser based Particle Image Velicimetry (PIV) technique. Firstly, the flow structure in close region of the stationary delta wing and formation of the vortex breakdown were studied by varying the angle of attack within the range of $7^{\circ} \leq \alpha \leq 17^{\circ}$. Secondly, changes in flow structure were observed varying the yaw angle of the delta wing within the range of $0^{\circ} \leq \theta \leq 15^{\circ}$. In summary, patterns of time-averaged vorticity, $\langle \omega \rangle$, streamline, $\langle \Psi \rangle$, distribution of velocity vectors, $\langle V \rangle$, and transverse velocity component, $\langle v \rangle / U$, for various angles of attack and yaw angles were obtained in order to reveal the flow mechanism in plan-view plane adjacent to the surface of the wing and over the crossflow planes.

Keywords: Delta wing, yaw angle, PIV, vortex breakdown

ÖZ
YÜKSEK LİSANS TEZİ

SÜPÜRME AÇISI KÜÇÜK DELTA KANAT ÜZERİNDE
GİRDAP OLUŞUMU

Çetin CANPOLAT

ÇUKUROVA ÜNİVERSİTESİ
FEN BİLİMLERİ ENSTİTÜSÜ
MAKİNA MÜHENDİSLİĞİ ANABİLİM DALI

Danışman : Prof. Dr. Beşir ŞAHİN
Yıl : 2008, Pages:101
Jüri : Prof. Dr. Beşir ŞAHİN
Doç. Dr. Hüseyin AKILLI
Doç. Dr. Galip SEÇKİN

Bu çalışmada, düşük süpürme açısına sahip delta kanadın akış yapısı boya görüntüleme yöntemiyle nitel olarak, Parçacık Görüntülemeli Hız Ölçme (PIV) yöntemiyle nicel olarak incelenmiştir. İlk olarak, sabit kanadın yüzeyine yakın bölgedeki akış yapısı ve girdap çökmesi oluşumu hücum açısı, $7^{\circ} \leq \alpha \leq 17^{\circ}$ aralığında değiştirilerek incelenmiştir. İkinci olarak da, sapma açısı $0^{\circ} \leq \theta \leq 15^{\circ}$ aralığında değiştirilerek akış yapısındaki değişimler gözlemlenmiştir. Özetle, kanat yüzeyine yakın bölgedeki üstten görünüş düzleminde ve akış yönüne dik düzlemde hücum ve sapma açılarına göre akış mekanizmasını incelemek için zaman ortalama eş değer girdap eğrileri, $\langle \omega \rangle$, akım çizgileri, $\langle \Psi \rangle$, hız vektörlerinin dağılımı, $\langle V \rangle$, akış istikametine dik yöndeki hız bileşeni, $\langle v \rangle / U$, değişkenleri hesaplanmıştır

Anahtar Kelimeler: Delta Kanat, sapma açısı, PIV, girdap çökmesi

ACKNOWLEDGEMENTS

Words are inadequate to express my sincere and special thanks to my advisor, Prof. Dr. Beşir ŞAHİN, for his motivation, help, wisdom, patience and encouragement both in my undergraduate and master education.

Also, I would like to express sincere and special thanks to Assoc. Prof. Dr. Hüseyin AKILLI for his motivation, support and sharing his valuable experiences with me.

I would like to thank to Assoc. Prof. Dr. Galip SEÇKİN for his additional support to my thesis.

I would like to thank to Asist. Prof. Dr. Cuma KARAKUŞ for his moral support, help and friendship.

I would like to thank to Research Assistants M. Atakan AKAR and Sedat YAYLA for moral support, help and friendship.

I would like to thank to Engin PINAR, Kamil PAYDAŞ, Selim SAÇMA, M. Arda MATUR, Burcu Elveren OĞUZ for moral support, help and friendship.

I would like to thank to Research Assistant İlyas KACAR for his moral support, help and friendship.

In addition, I would like to thank all staffs of Department of Mechanical Engineering of Çukurova University.

I would like to express my sincere and special thanks to all members of my family individually for their thrust, motivation, moral support, wisdom, patience and encouragement during this hard and laboured study.

I would like to thank to everyone who I can not call their names for their support during this study.

NOMENCLATURE

U	: Free stream velocity
C	: Delta wing chord
α	: Angle of attack
θ	: Yaw angle
Λ	: Sweep angle
S	: Saddle point
F	: Focus
N	: Nodal point
$\langle\omega\rangle$: Time-averaged vorticity
$\langle\Psi\rangle$: Time-averaged streamline
$\langle V\rangle$: Time-averaged velocity distribution
$\langle v\rangle/U$: Time-averaged component of transverse velocity
X/C	: The dimensionless chord axis
Re_c	: Reynolds number depending on the delta wing chord
K	: Sychev similarity parameter

TABLE OF CONTENTS	Page
ABSTRACT.....	III
ÖZ.....	IV
ACKNOWLEDGEMENTS.....	V
NOMENCLATURE.....	VI
TABLE OF CONTENTS.....	VII
LIST OF FIGURES.....	IX
1. INTRODUCTION.....	1
2. PREVIOUS STUDIES.....	12
2.1. Flow Structure around Delta Wings.....	12
2.1.1 Delta Wings with High Sweep Angle.....	12
2.1.2 Delta Wings Having Low-Moderate Sweep Angle....	17
2.2. Vortex Breakdown.....	21
3. METERIAL METHOD.....	26
3.1. Channel System.....	26
3.1.1. Experimental Apartures.....	27
3.2. Dye and Particle Image Velocimetry (PIV) Experiments.....	28
3.2.1. Dye Visualization Experiments.....	28
3.2.2. Particle Image Velocimetry (PIV) Experiments	29
3.2.2.1. Measurement Principle.....	29
3.2.2.2. Illumination.....	31
3.2.2.3 Adaptive Cross-Correlation Technique and Further Analysis.....	32
3.3 Experimental System.....	33
4. RESULT AND DISCUSSIONS.....	36
4.1. Flow Structure on a Delta Wing of Low Sweep Angle	36
4.1.1. Dye Visualization Results.....	36
4.1.2. Particle Image Velocimetry (PIV) Results	47
4.1.2.1 Patterns of Time-Averaged Vorticity, Streamline and Velovity Vectors Topology	47

	(End-View).....	
4.1.2.2	Patterns of Time-Averaged Vorticity, Streamline and Velocity Vectors Topology (Plan-View).....	63
4.1.2.3	Patterns of Time-Averaged Component of Transverse Velocity.....	84
5.	CONCLUSIONS.....	89
	REFERENCES.....	91
	CIRRICULUM VITAE.....	96
	APPENDIX.....	97

LIST OF FIGURES		Page
Figure 1.1.	Sketch of vortical flow around a delta wing	2
Figure 1.2.	Vortex breakdown flow visualization around NASA's F-18 High Angle of Attack Research Vehicle (HARV) using smoke to seed the vortex emanating from the nose of the aircraft at $\alpha=20^\circ$ incidence	4
Figure 1.3.	Influence of Reynolds number on dual vortex structure (a) $Re=10000$, (b) $Re=20000$, (c) $Re=50000$	5
Figure 1.4.	Variation of wing tip rms acceleration as a function of angle of attack for a $\Lambda=60^\circ$ sweep half delta wing model	5
Figure 1.5.	Schematic of the subsonic flow field over the top of a delta wing at angle of attack	7
Figure 1.6.	Dye streaks following primary LEVs for 50-deg wing: $\alpha = 5, 10, \text{ and } 20$ deg; planform and side views	8
Figure 1.7.	Characteristic of delta wing turbulence intensity distributions and power spectral densities for the leading-edge vortex breakdown flow field; $\Lambda=76^\circ$, $Re_C=1.07 \times 10^6$	9
Figure 1.8.	Current and future unmanned combat air vehicles and fixed-wing micro air vehicles	11
Figure 2.1.	Types of vortex breakdown	22
Figure 3.1.	Schematic of the water channel	26
Figure 3.2.	Sketch of the special aperture	27
Figure 3.3.	Servo Motor and its control Unit	28
Figure 3.4.	Schematics view of channel and its mechanism	29
Figure 3.5.	Schematic view of 3D	30
Figure 3.6.	A Nd.YAG Laser Source	31
Figure 3.7.	Schematic of experimental arrangement showing delta wing, laser sheet location, and definition of key parameters.	35
Figure 4.1.	Dye visualization of flow in side-view plane over the delta wing	36

Figure 4.2.	Formation and development of spiral vortex and vortex breakdown observed in plan-view plane.	38
Figure 4.3.	Formation and development of spiral vortex, vortex breakdown and separation flow region against yaw angle.	41
Figure 4.4.	Formation and development of spiral vortex, vortex breakdown and separation flow region against yaw angle	42
Figure 4.5.	A representative images of vortex breakdown locations at $\theta=0^\circ$.	44
Figure 4.6.	Formation and development of vortex structure in end-view plane at $X/C=0.6$, $\theta=0^\circ$.	45
Figure 4.7.	Formation and development of vortex structure in end-view plane at $X/C=0.8$, $\theta=0^\circ$.	45
Figure 4.8.	Formation and development of vortex structure in end-view plane at $X/C=1$, $\theta=0^\circ$.	53
Figure 4.9.	Figure 4.9. Patterns of time-averaged vorticity, $\langle\omega\rangle$, streamline, $\langle\Psi\rangle$, and distribution of velocity vectors, $\langle V\rangle$, for angle of attack $\alpha=7^\circ$, $\theta=0^\circ$. Laser sheet is located at $x/C = 0.8$. For contours of time-averaged vorticity, minimum and incremental values are $[\langle\omega\rangle]_{\min} = 0.3 \text{ s}^{-1}$ and $\Delta[\langle\omega\rangle] = 0.3 \text{ s}^{-1}$.	48
Figure 4.10.	Patterns of time-averaged vorticity, $\langle\omega\rangle$, streamline, $\langle\Psi\rangle$, and distribution of velocity vectors, $\langle V\rangle$, for angle of attack $\alpha=7^\circ$, $\theta=6^\circ$. Laser sheet is located at $x/C = 0.8$. For contours of time-averaged vorticity, minimum and incremental values are $[\langle\omega\rangle]_{\min} = 0.3 \text{ s}^{-1}$ and $\Delta[\langle\omega\rangle] = 0.3 \text{ s}^{-1}$.	49
Figure 4.11.	Patterns of time-averaged vorticity, $\langle\omega\rangle$, streamline, $\langle\Psi\rangle$, and distribution of velocity vectors, $\langle V\rangle$, for angle of attack $\alpha=7^\circ$, $\theta=8^\circ$. Laser sheet is located at $x/C = 0.8$. For contours of time-averaged vorticity, minimum and incremental values are $[\langle\omega\rangle]_{\min} = 0.3 \text{ s}^{-1}$ and $\Delta[\langle\omega\rangle] = 0.3 \text{ s}^{-1}$.	51
Figure 4.12.	Patterns of time-averaged vorticity, $\langle\omega\rangle$, streamline, $\langle\Psi\rangle$, and distribution of velocity vectors, $\langle V\rangle$, for angle of attack $\alpha=10^\circ$, $\theta=0^\circ$. Laser sheet is located at $x/C = 0.8$. For contours of time-averaged vorticity, minimum and incremental values are $[\langle\omega\rangle]_{\min} = 0.3 \text{ s}^{-1}$ and $\Delta[\langle\omega\rangle] = 0.3 \text{ s}^{-1}$.	52
Figure 4.13.	Patterns of time-averaged vorticity, $\langle\omega\rangle$, streamline, $\langle\Psi\rangle$, and distribution of velocity vectors, $\langle V\rangle$, for angle of attack $\alpha=10^\circ$, $\theta=6^\circ$. Laser sheet is located at $x/C = 0.8$. For contours of time-averaged vorticity, minimum and incremental values are $[\langle\omega\rangle]_{\min} = 0.3 \text{ s}^{-1}$ and $\Delta[\langle\omega\rangle]$	54

$$=0.3 \text{ s}^{-1}.$$

- Figure 4.14. Patterns of time-averaged vorticity, $\langle\omega\rangle$, streamline, $\langle\Psi\rangle$, and distribution of velocity vectors, $\langle V\rangle$, for angle of attack $\alpha=10^\circ$, $\theta=8^\circ$. Laser sheet is located at $x/C = 0.8$. 55
 For contours of time-averaged vorticity, minimum and incremental values are $[\langle\omega\rangle]_{\min} = 0.3 \text{ s}^{-1}$ and $\Delta[\langle\omega\rangle] = 0.3 \text{ s}^{-1}$.
- Figure 4.15. Patterns of time-averaged vorticity, $\langle\omega\rangle$, streamline, $\langle\Psi\rangle$, and distribution of velocity vectors, $\langle V\rangle$, for angle of attack $\alpha=13^\circ$, $\theta=0^\circ$. Laser sheet is located at $x/C = 0.8$. 56
 For contours of time-averaged vorticity, minimum and incremental values are $[\langle\omega\rangle]_{\min} = 0.3 \text{ s}^{-1}$ and $\Delta[\langle\omega\rangle] = 0.3 \text{ s}^{-1}$.
- Figure 4.16. Patterns of time-averaged vorticity, $\langle\omega\rangle$, streamline, $\langle\Psi\rangle$, and distribution of velocity vectors, $\langle V\rangle$, for angle of attack $\alpha=13^\circ$, $\theta=6^\circ$. Laser sheet is located at $x/C = 0.8$. 57
 For contours of time-averaged vorticity, minimum and incremental values are $[\langle\omega\rangle]_{\min} = 0.3 \text{ s}^{-1}$ and $\Delta[\langle\omega\rangle] = 0.3 \text{ s}^{-1}$.
- Figure 4.17. Patterns of time-averaged vorticity, $\langle\omega\rangle$, streamline, $\langle\Psi\rangle$, and distribution of velocity vectors, $\langle V\rangle$, for angle of attack $\alpha=13^\circ$, $\theta=8^\circ$. Laser sheet is located at $x/C = 0.8$. 58
 For contours of time-averaged vorticity, minimum and incremental values are $[\langle\omega\rangle]_{\min} = 0.3 \text{ s}^{-1}$ and $\Delta[\langle\omega\rangle] = 0.3 \text{ s}^{-1}$.
- Figure 4.18. Patterns of time-averaged vorticity, $\langle\omega\rangle$, streamline, $\langle\Psi\rangle$, and distribution of velocity vectors, $\langle V\rangle$, for angle of attack $\alpha=17^\circ$, $\theta=0^\circ$. Laser sheet is located at $x/C = 0.8$. 59
 For contours of time-averaged vorticity, minimum and incremental values are $[\langle\omega\rangle]_{\min} = 0.3 \text{ s}^{-1}$ and $\Delta[\langle\omega\rangle] = 0.3 \text{ s}^{-1}$.
- Figure 4.19. Patterns of time-averaged vorticity, $\langle\omega\rangle$, streamline, $\langle\Psi\rangle$, and distribution of velocity vectors, $\langle V\rangle$, for angle of attack $\alpha=17^\circ$, $\theta=6^\circ$. Laser sheet is located at $x/C = 0.8$. 60
 For contours of time-averaged vorticity, minimum and incremental values are $[\langle\omega\rangle]_{\min} = 0.3 \text{ s}^{-1}$ and $\Delta[\langle\omega\rangle] = 0.3 \text{ s}^{-1}$.
- Figure 4.20. Patterns of time-averaged vorticity, $\langle\omega\rangle$, streamline, $\langle\Psi\rangle$, and distribution of velocity vectors, $\langle V\rangle$, for angle of attack $\alpha=17^\circ$, $\theta=8^\circ$. Laser sheet is located at $x/C = 0.8$. 61
 For contours of time-averaged vorticity, minimum and incremental values are $[\langle\omega\rangle]_{\min} = 0.3 \text{ s}^{-1}$ and $\Delta[\langle\omega\rangle] = 0.3 \text{ s}^{-1}$.

Figure 4.21.	Patterns of time-averaged vorticity, $\langle\omega\rangle$, streamline, $\langle\Psi\rangle$, and distribution of velocity vectors, $\langle V\rangle$, for angle of attack $\alpha=7^\circ$, $\theta=0^\circ$. For contours of time-averaged vorticity, minimum and incremental values are $[\langle\omega\rangle]_{\min}=0.4\text{ s}^{-1}$ and $\Delta[\langle\omega\rangle]=1\text{ s}^{-1}$.	66
Figure 4.22.	Patterns of time-averaged vorticity, $\langle\omega\rangle$, streamline, $\langle\Psi\rangle$, and distribution of velocity vectors, $\langle V\rangle$, for angle of attack $\alpha=7^\circ$, $\theta=6^\circ$. For contours of time-averaged vorticity, minimum and incremental values are $[\langle\omega\rangle]_{\min}=0.4\text{ s}^{-1}$ and $\Delta[\langle\omega\rangle]=1\text{ s}^{-1}$.	67
Figure 4.23.	Patterns of time-averaged vorticity, $\langle\omega\rangle$, streamline, $\langle\Psi\rangle$, and distribution of velocity vectors, $\langle V\rangle$, for angle of attack $\alpha=7^\circ$, $\theta=8^\circ$. For contours of time-averaged vorticity, minimum and incremental values are $[\langle\omega\rangle]_{\min}=0.4\text{ s}^{-1}$ and $\Delta[\langle\omega\rangle]=1\text{ s}^{-1}$.	68
Figure 4.24.	Patterns of time-averaged vorticity, $\langle\omega\rangle$, streamline, $\langle\Psi\rangle$, and distribution of velocity vectors, $\langle V\rangle$, for angle of attack $\alpha=7^\circ$, $\theta=15^\circ$. For contours of time-averaged vorticity, minimum and incremental values are $[\langle\omega\rangle]_{\min}=0.4\text{ s}^{-1}$ and $\Delta[\langle\omega\rangle]=1\text{ s}^{-1}$.	69
Figure 4.25.	Patterns of time-averaged vorticity, $\langle\omega\rangle$, streamline, $\langle\Psi\rangle$, and distribution of velocity vectors, $\langle V\rangle$, for angle of attack $\alpha=10^\circ$, $\theta=0^\circ$. For contours of time-averaged vorticity, minimum and incremental values are $[\langle\omega\rangle]_{\min}=0.4\text{ s}^{-1}$ and $\Delta[\langle\omega\rangle]=1\text{ s}^{-1}$.	72
Figure 4.26.	Patterns of time-averaged vorticity, $\langle\omega\rangle$, streamline, $\langle\Psi\rangle$, and distribution of velocity vectors, $\langle V\rangle$, for angle of attack $\alpha=10^\circ$, $\theta=6^\circ$. For contours of time-averaged vorticity, minimum and incremental values are $[\langle\omega\rangle]_{\min}=0.4\text{ s}^{-1}$ and $\Delta[\langle\omega\rangle]=1\text{ s}^{-1}$.	73
Figure 4.27.	Patterns of time-averaged vorticity, $\langle\omega\rangle$, streamline, $\langle\Psi\rangle$, and distribution of velocity vectors, $\langle V\rangle$, for angle of attack $\alpha=10^\circ$, $\theta=8^\circ$. For contours of time-averaged vorticity, minimum and incremental values are $[\langle\omega\rangle]_{\min}=0.4\text{ s}^{-1}$ and $\Delta[\langle\omega\rangle]=1\text{ s}^{-1}$.	74
Figure 4.28.	Patterns of time-averaged vorticity, $\langle\omega\rangle$, streamline, $\langle\Psi\rangle$, and distribution of velocity vectors, $\langle V\rangle$, angle of attack $\alpha=10^\circ$, $\theta=15^\circ$. For contours of time-averaged vorticity, minimum and incremental values are $[\langle\omega\rangle]_{\min}=0.4\text{ s}^{-1}$ and $\Delta[\langle\omega\rangle]=1\text{ s}^{-1}$.	75
Figure 4.29.	Patterns of time-averaged vorticity, $\langle\omega\rangle$, streamline,	76

	$\langle\Psi\rangle$, and distribution of velocity vectors, $\langle V\rangle$, for angle of attack $\alpha=13^\circ$, $\theta=0^\circ$. For contours of time-averaged vorticity, minimum and incremental values are $[\langle\omega\rangle]_{\min}=0.4\text{ s}^{-1}$ and $\Delta[\langle\omega\rangle]=1\text{ s}^{-1}$.	
Figure 4.30.	Patterns of time-averaged vorticity, $\langle\omega\rangle$, streamline, $\langle\Psi\rangle$, and distribution of velocity vectors, $\langle V\rangle$, for angle of attack $\alpha=13^\circ$, $\theta=6^\circ$. For contours of time-averaged vorticity, minimum and incremental values are $[\langle\omega\rangle]_{\min}=0.4\text{ s}^{-1}$ and $\Delta[\langle\omega\rangle]=1\text{ s}^{-1}$.	77
Figure 4.31.	Patterns of time-averaged vorticity, $\langle\omega\rangle$, streamline, $\langle\Psi\rangle$, and distribution of velocity vectors, $\langle V\rangle$, for angle of attack $\alpha=13^\circ$, $\theta=8^\circ$. For contours of time-averaged vorticity, minimum and incremental values are $[\langle\omega\rangle]_{\min}=0.4\text{ s}^{-1}$ and $\Delta[\langle\omega\rangle]=1\text{ s}^{-1}$.	78
Figure 4.32.	Patterns of time-averaged vorticity, $\langle\omega\rangle$, streamline, $\langle\Psi\rangle$, and distribution of velocity vectors, $\langle V\rangle$, for angle of attack $\alpha=13^\circ$, $\theta=15^\circ$. For contours of time-averaged vorticity, minimum and incremental values are $[\langle\omega\rangle]_{\min}=0.4\text{ s}^{-1}$ and $\Delta[\langle\omega\rangle]=1\text{ s}^{-1}$.	79
Figure 4.33.	Patterns of time-averaged vorticity, $\langle\omega\rangle$, streamline, $\langle\Psi\rangle$, and distribution of velocity vectors, $\langle V\rangle$, for angle of attack $\alpha=17^\circ$, $\theta=0^\circ$. For contours of time-averaged vorticity, minimum and incremental values are $[\langle\omega\rangle]_{\min}=0.4\text{ s}^{-1}$ and $\Delta[\langle\omega\rangle]=1\text{ s}^{-1}$.	80
Figure 4.34.	Patterns of time-averaged vorticity, $\langle\omega\rangle$, streamline, $\langle\Psi\rangle$, and distribution of velocity vectors, $\langle V\rangle$, for angle of attack $\alpha=17^\circ$, $\theta=6^\circ$. For contours of time-averaged vorticity, minimum and incremental values are $[\langle\omega\rangle]_{\min}=0.4\text{ s}^{-1}$ and $\Delta[\langle\omega\rangle]=1\text{ s}^{-1}$.	81
Figure 4.35.	Patterns of time-averaged vorticity, $\langle\omega\rangle$, streamline, $\langle\Psi\rangle$, and distribution of velocity vectors, $\langle V\rangle$, for angle of attack $\alpha=17^\circ$, $\theta=8^\circ$. For contours of time-averaged vorticity, minimum and incremental values are $[\langle\omega\rangle]_{\min}=0.4\text{ s}^{-1}$ and $\Delta[\langle\omega\rangle]=1\text{ s}^{-1}$.	82
Figure 4.36.	Patterns of time-averaged vorticity, $\langle\omega\rangle$, streamline, $\langle\Psi\rangle$, and distribution of velocity vectors, $\langle V\rangle$, for angle of attack $\alpha=17^\circ$, $\theta=15^\circ$. For contours of time-averaged vorticity, minimum and incremental values are $[\langle\omega\rangle]_{\min}=0.4\text{ s}^{-1}$ and $\Delta[\langle\omega\rangle]=1\text{ s}^{-1}$.	83
Figure 4.37.	Patterns of time-averaged component of transverse, $[\langle v\rangle/U]$, velocity for attack angle $\alpha=7^\circ$. Minimum and incremental values are $[\langle v\rangle/U]_{\min}=0.03\text{ s}^{-1}$ and $\Delta[\langle v\rangle/U]=0.03\text{ s}^{-1}$.	85

Figure 4.38.	Patterns of time-averaged component of transverse velocity, $[\langle v \rangle / U]$, for attack angle $\alpha = 10^\circ$. Minimum and incremental values are $[\langle v \rangle / U]_{\min} = 0.03 \text{ s}^{-1}$ and $\Delta[\langle v \rangle / U] = 0.03 \text{ s}^{-1}$	86
Figure 4.39.	Patterns of time-averaged component of transverse velocity, $[\langle v \rangle / U]$, for attack angle $\alpha = 13^\circ$. Minimum and incremental values are $[\langle v \rangle / U]_{\min} = 0.03 \text{ s}^{-1}$ and $\Delta[\langle v \rangle / U] = 0.03 \text{ s}^{-1}$	87
Figure 4.40.	Patterns of time-averaged component of transverse velocity, $[\langle v \rangle / U]$, for attack angle $\alpha = 17^\circ$. Minimum and incremental values are $[\langle v \rangle / U]_{\min} = 0.03 \text{ s}^{-1}$ and $\Delta[\langle v \rangle / U] = 0.03 \text{ s}^{-1}$	88
Figure 1.	Principle of stereo-vision.	97
Figure 2.	Example of calibration images recorded from camera 1 and camera 2.	98
Figure 3.	Overlapping fields of view.	99
Figure 4.	3D PIV data reconstruction	100
Figure 5.	Scheimpflug condition camera plane.	100
Figure 6.	Standard calibration target mounted on traverse.	101

1. INTRODUCTION

Many flows in nature have time-dependent (unsteady) free stream velocity. For example; flow around bridges, towers, automobiles, miscellaneous regions of aircraft body and in compressors, turbines, pumps, heat exchangers. If brief research has been made for these type of flows, the separated and vortex dominated flows can be seen frequently. Unmanned Combat Aerial Vehicles are used in variety of missions that require high maneuverability over a wide range of speed. Unsteady aerodynamics of non-slender delta wings, consisted of shear layer instabilities, structure of vortices, occurrence of breakdown, and fluid/structure interactions were extensively reviewed by Gursul et. al. (2005). They emphasized on the sensitivity of the vortical flow structures with attack angle of the delta wing. Yaniktepe and Rockwell (2004) stated that the non-slender delta wings exhibit distinctive features than slender delta wings especially at a higher angle of attack. Yavuz et. al.(2004) studies the vortical flow structure on a plane immediately adjacent to the surface of non-slender delta wing with $\Lambda=38.9^\circ$ sweep angle using the Particle Image Velocimetry (PIV) technique. Their main finding are;

- i. The time-averaged flow data distributions are symmetric with respect to the plane of symmetry of the delta wing.
- ii. The time- averaged flow data presents well-defined critical points occurring on both side of central axis of the wing. The pattern of instantaneous vorticity varies rapidly and indicates critical points at different locations comparing the time-averaged streamline topology. But vorticity concentrations are not present in both instantaneous and time-averaged streamline topology. High rate of velocity fluctuations occur in regions of the vortex breakdown.

The flow is dominated by two large and counter-rotating vortices at considerable high angle of attack shown in Figure 1.1 (Taylor and Gursul, 2004).

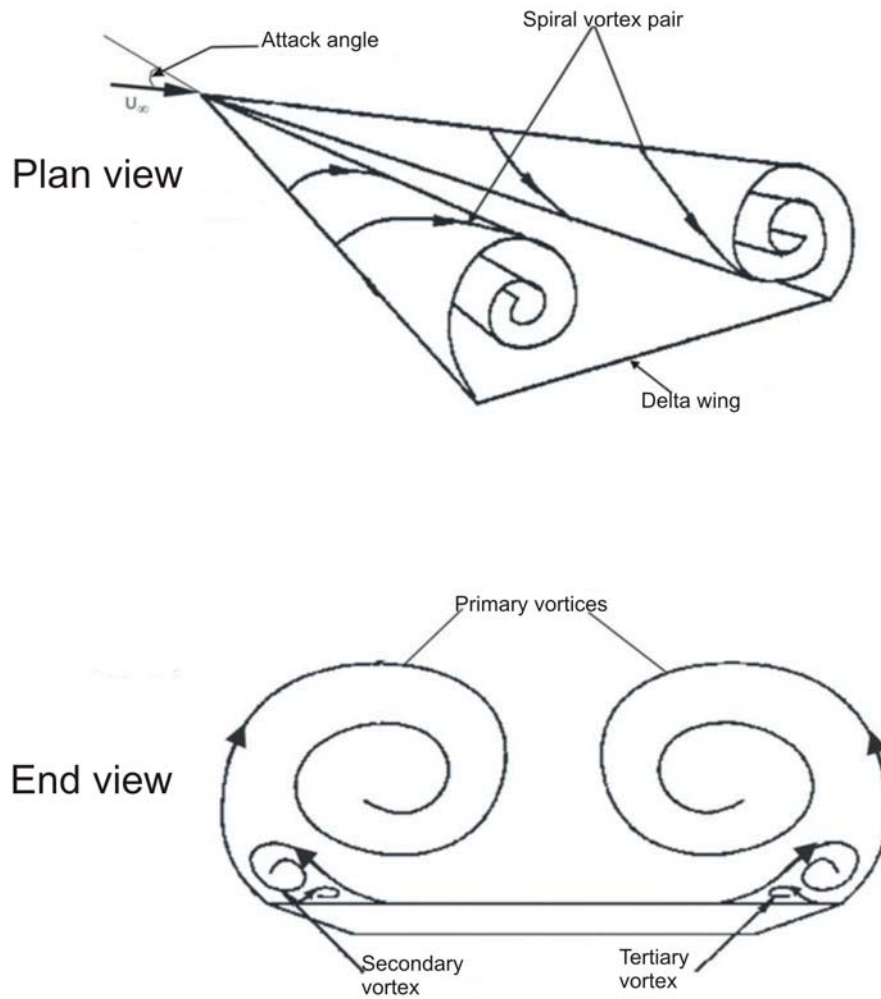


Figure 1.1. Sketch of vortical flow around a delta wing (Taylor and Gursul, 2004)

These types of flows over delta wings cause decrease in maneuverability of aircrafts and material fatigue and eventually crack in the materials. To be able to obtain good aircraft maneuverability, the understanding of these types of flows is considerably important. Sarpkaya (1971) performed experiments in swirling flows in a diverging cylindrical tube in which various types of vortex breakdown were observed. He stated that there are three basic types of stationary vortex breakdown: double helix, spiral and axisymmetric or bubble. Then, he (1995) declared that at high Reynolds numbers ($Re=22500$), vortex breakdown geometry gradually arrives at its-cone-like form. He considered fourth fundamental type of vortex breakdown (the conical type) in addition to the double-type, spiral and nearly axisymmetric type. The swirling flow is

highly unstable to spiral disturbances for Reynolds numbers between approximately 1000 and 2000. The axisymmetric breakdown evolves either from double helix, or from a spiral, or directly from an axisymmetric swelling of the vortex core. He also suggested that the vortex breakdown phenomenon is governed by two basic and conceptually different mechanisms, hydrodynamic instability and finite-transition to sequent state. Delery (1994) stated that the three-dimensional flows, boundary-layer separation leads to the formation of vortices formed by the roll up of the viscous flow sheet, previously confined in a thin layer attached to the wall-which suddenly springs into the outer non-dissipative flow. Such vortices appear in a large number of circumstances and they often play dominant role in the overall flow properties. The strength of primary vortex steadily increases with the angle of attack, until disorganization occurs in the case of a delta wing. Gursul (2005) reviewed a wide range of unsteady phenomena relevant to slender vortex flows over stationary and maneuvering delta wings and dynamic response of leading edge vortices for maneuvering wings and mechanisms of hysteresis and time lag effects. He discussed the origin, characteristics, and physical mechanisms of these unsteady phenomena and their role in buffeting. He led to researchers about unresolved and well-understood issues. For example, he stated that although the main features of the unsteady phenomena related to slender delta wings are relatively well understood, many aspects require further study. The details of the shear layer instabilities, steady and unsteady substructures, and transition need to be investigated further. He counted lots of things which should observe in details about unsteady aerodynamics. Also, in the same year, Gursul et. al. reviewed unsteady aerodynamics of nonslender delta wings, covering topics of shear layer instabilities, structure of nonslender vortices, breakdown, maneuvering wings, and fluid/structure interactions. They stated that vortical flows develop at very low angles of attack, and form close to the wing surface. This results in strong interactions with the upper surface boundary layer and in a pronounced dependence of the flow structure on Reynolds number shown in Figure 1.3. Vortex breakdown is observed to be much less abrupt compared to breakdown over slender wings. This results in challenges for the precise determination of vortex breakdown location and the interpretation of flow

visualizations. One of the distinct features of nonslender wings is the location of the primary attachment zone outboard of the symmetry plane. Reattachment location correlates with the wing stall process and increased buffeting. Dramatic fluid/structure interactions (Figure 1.4) emerge with increasing wing flexibility and result in substantial lift enhancement in the post-stall region. This recently discovered phenomenon appears to be a feature of nonslender wings. Rigid delta wings undergoing small amplitude oscillations in the post-stall region exhibit many similarities to flexible wings, including reattachment and re-formation of the leading-edge vortices. Unusual self-excited roll oscillations have also been observed for free-to-roll nonslender wings.

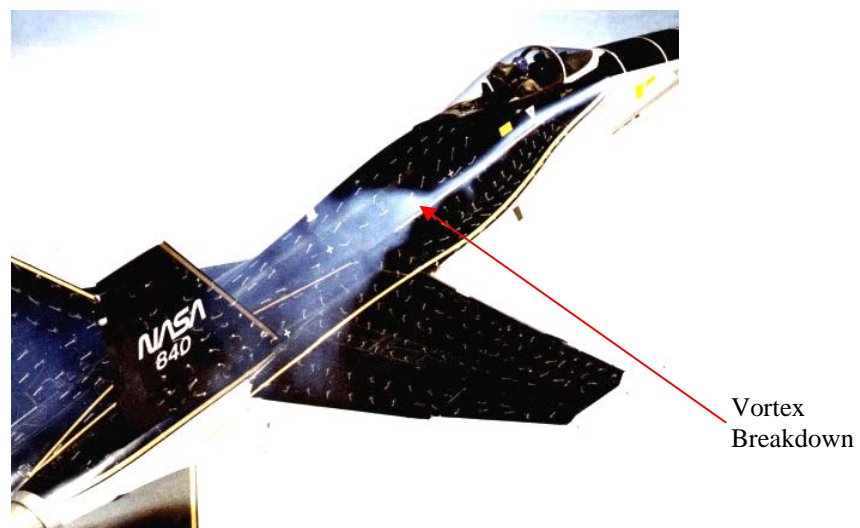


Figure 1.2. Vortex breakdown flow visualization around NASA's F-18 High Angle of Attack Research Vehicle (HARV) using smoke to see the vortex emanating from the nose of the aircraft at $\alpha=20^\circ$ incidence (Yanktepe, 2006).

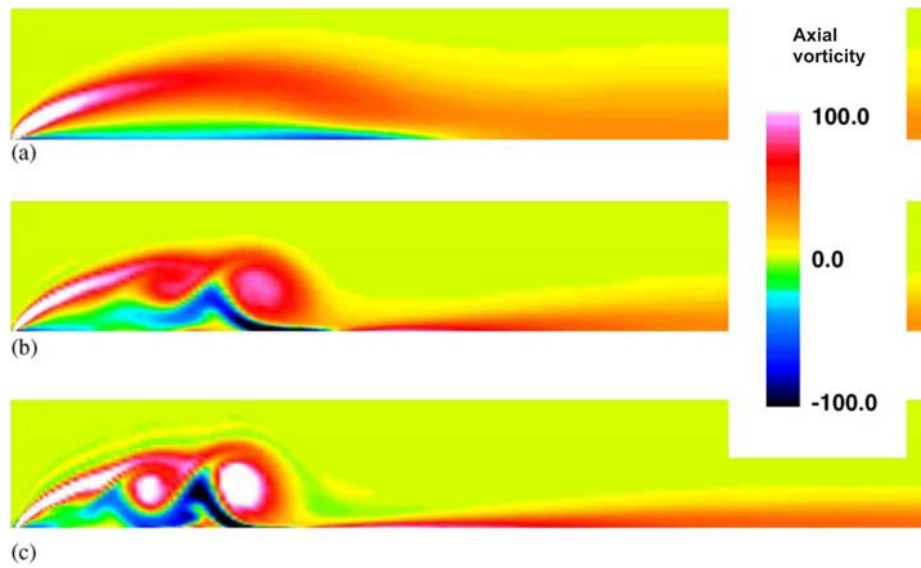


Figure 1.3. Influence of Reynolds number on dual vortex structure (a) $Re=10000$, (b) $Re=20000$, (c) $Re=50000$ (Gursul et. al. 2005).

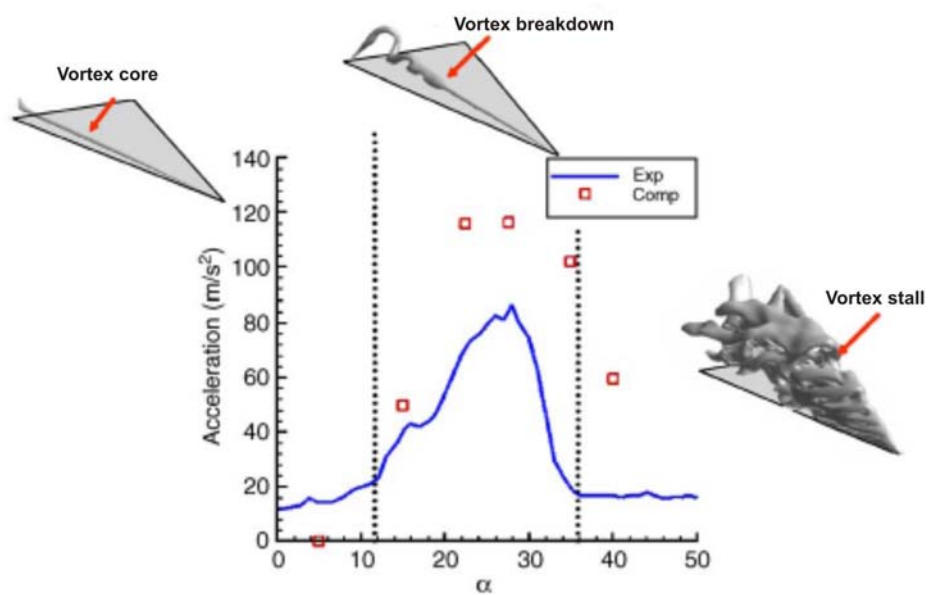


Figure 1.4. Variation of wingtip rms acceleration as a function of angle of attack for a $\Lambda=60^\circ$ sweep half delta wing model (Gursul et al.2005).

The leading edge vortices are strong and stable. Shih and Ding (1996) have identified the importance of the secondary LEV (Leading Edge Vortex) in affecting the

primary LEV and, in particular, in interacting with identifiable vortical structures within the leading-edge shear layer for a 60-deg wing. Indeed, there has been a considerable recent interest in the role of such structures. At the low incidence angles involved, the LEVs are close to the wing surface, and vortex breakdown regions interact strongly with flow near the leeward surface. Anderson (2001), shown in Figure 1.5, stated that being a source of high energy, relatively high vortical flow, the local static pressure in the vicinity of the vortices is small. Hence, the surface pressure on the top surface of the delta wing is reduced near the leading edge and is higher and reasonably constant over the middle of the wing. The qualitative variation of the pressure coefficient in the spanwise direction is sketched in this figure. The spanwise variation of pressure over the bottom surface is essentially constant and higher than the freestream pressure (a positive C_p). Over the top of surface, the spanwise variation in the midsection of the wing is essentially constant and lower than the freestream pressure (a negative C_p). Ol and Gharib (2003) measured the velocity field near the apex region of moderately swept delta wings in a water tunnel, using a version of stereoscopic digital particle imaging velocimetry. Flow visualization was also used to verify these results shown in Figure 1.6. Delta wings of 50-deg and 65-deg leading-edge sweep and 30-deg windward-side bevels were tested at Reynolds numbers of $6 \times 10^3 - 1.5 \times 10^4$. At these low Reynolds numbers, secondary leading edge vortices were weak, giving way to essentially stagnant flow outboard of the primary leading edge vortices at the higher angles of attack. Otherwise, velocity data for the 65-deg wing were consistent with well-known observations for slender delta wings. The 50-deg wing exhibited unexpectedly strong primary leading-edge vortices at low angles of attack, with a generally conical velocity field. Upstream progression of vortex breakdown with increasing angle of attack exhibited extensive regions of streamwise undulation. Leading edge shear layer rollup was observed in cross flow planes well downstream of the breakdown region, but with an increased occurrence of paired vortical structures of opposite sign inside the shear layer itself.

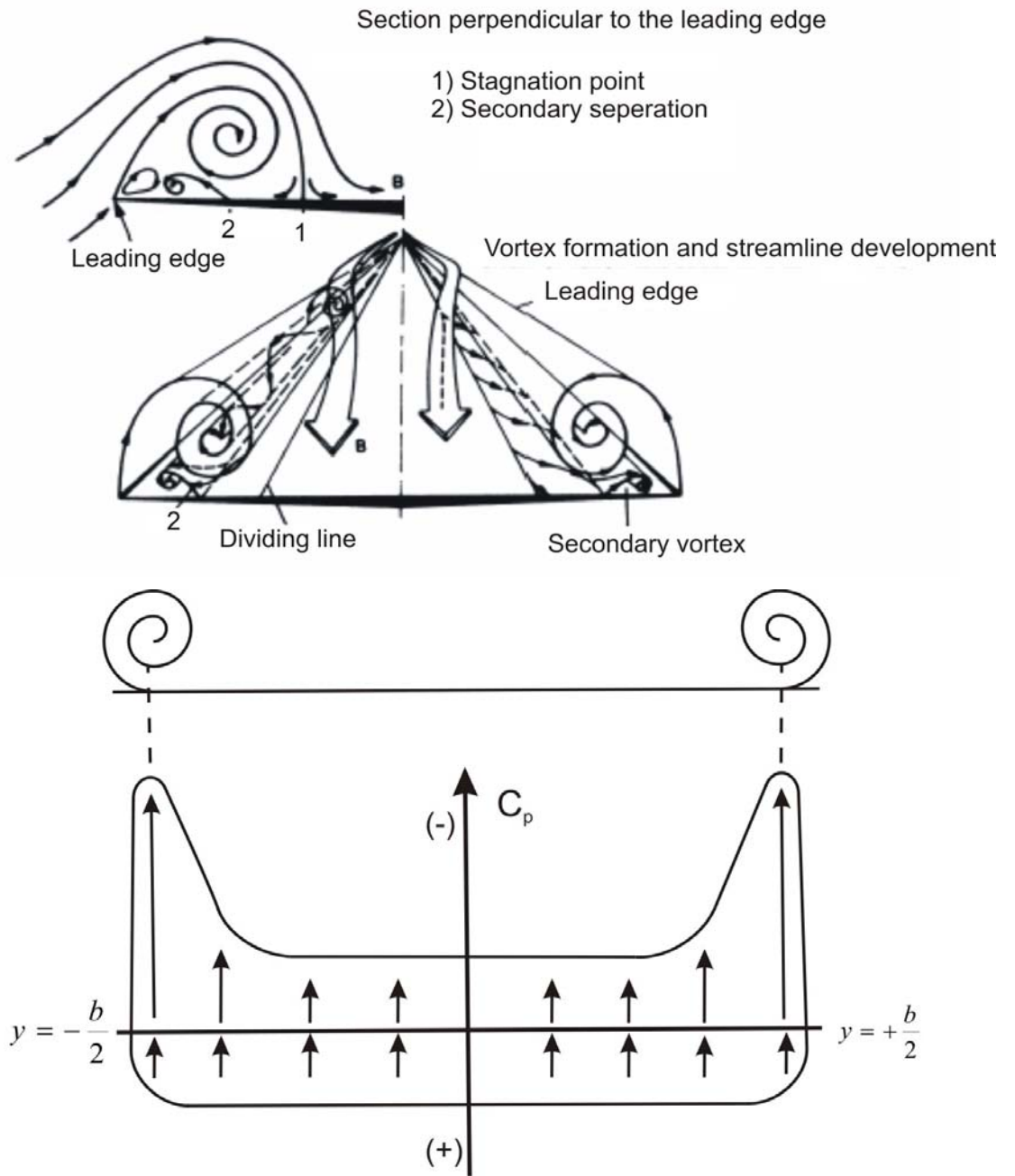


Figure 1.5. Schematic of the subsonic flow field over the top of a delta wing at angle of attack (Anderson, 2001).

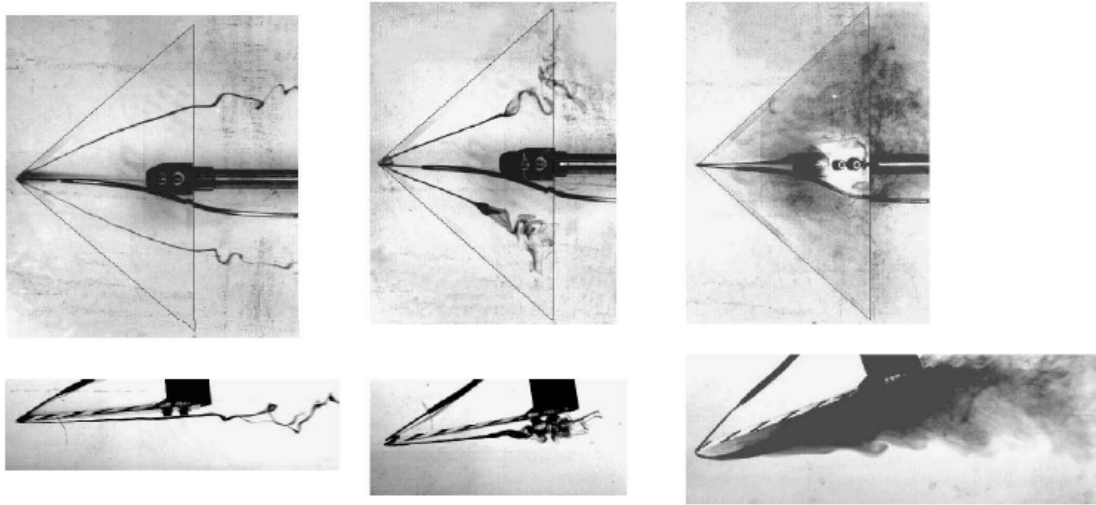


Figure 1.6. Dye streaks following primary LEVs for 50-deg wing: $\alpha = 5, 10,$ and 20 deg; planform and side views (Ol and Gharib, 2003).

Breitsamter (2008) presented selected results from extensive experimental investigations on turbulent flow fields and unsteady surface pressures caused by leading-edge vortices, in particular, for vortex breakdown flow. Such turbulent flows may cause severe dynamic aero-elastic problems like wing and/or fin buffeting on fighter-type aircraft. The wind tunnel models used include a generic delta wing as well as a detailed aircraft configuration of canard-delta wing type. The turbulent flow structures are analyzed by root-mean-square and spectral distributions of velocity shown in Figure 1.7 and pressure fluctuations. Downstream of bursting local maxima of velocity fluctuations occur in a limited radial range around the vortex center. The corresponding spectra exhibit significant peaks indicating that turbulent kinetic energy is channeled into a narrow band. These quasi-periodic velocity oscillations arise from helical mode instability of the breakdown flow. Due to vortex bursting there is a characteristic increase in surface pressure fluctuations with increasing angle of attack, especially when the burst location moves closer to the apex. The pressure fluctuations also show dominant frequencies corresponding to those of the velocity fluctuations. Using the measured flow field data, scaling parameters are derived for design purposes. It is shown that a frequency parameter based on the local semi-span and the sinus of angle of attack can be used to estimate the frequencies of dynamic loads evoked by vortex bursting.

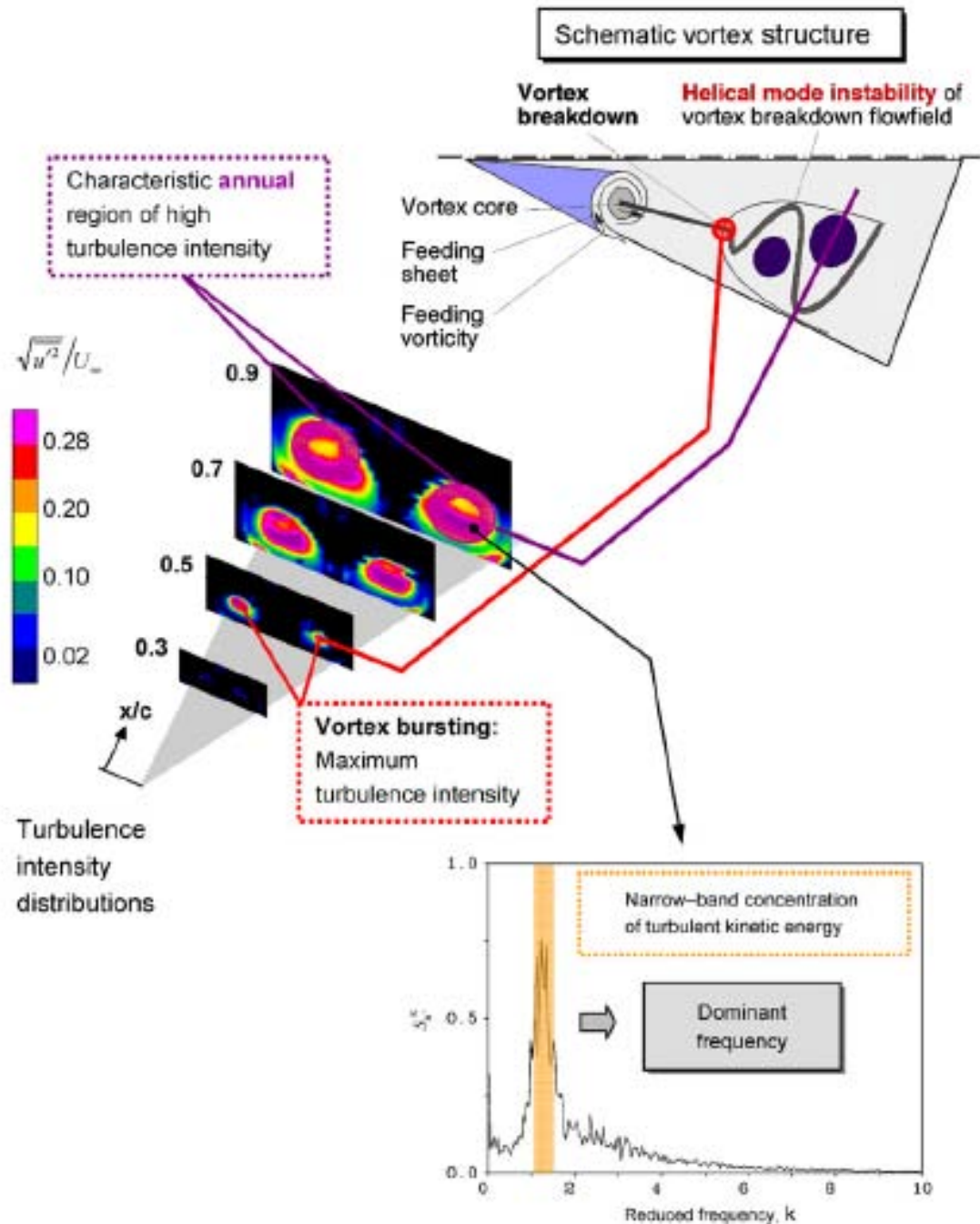


Figure 1.7. Characteristic of delta wing turbulence intensity distributions and power spectral densities for the leading-edge vortex breakdown flow field; $\Lambda=76^\circ$, $Re_C=1.07 \times 10^6$ (Breitsamter, 2008).

Yaniktepe and Rockwell (2005) performed experimentally investigations on the flow structures at trailing-edge regions of diamond and lambda type wings. In both wings vortical flow structures in the cross-flow planes of trailing edge vary rapidly with the

attack angles. Vortical flow structure and flow topology in regions close to the plane surface of a delta wing are characterized under the trailing-edge blowing by Yavuz and Rockwell (2005). It was found that the trailing-edge blowing can significantly alter the topological flow patterns in close region proximity to the delta wing surface. Sohn et. al. (2004) visually investigated the development and interaction of vortices in cross-flow planes at various locations on the delta wing with leading-edge extension (LEX) using micro water droplets and a laser beam sheet. The range of attack angle was taken as $12^\circ \leq \alpha \leq 24^\circ$ at yaw angles of $0^\circ, -5^\circ$ and -10° . In general, when the angle of attack increases the wing vortex and LEX vortex coiled around with higher strength and the cores of this combined vortices shifted inboard and upward. It was indicated that introducing yaw angle the coiling, the merging and diffusion of the wing and LEX vortices increased and the windward side, whereas they become delayed significantly on the leeward side. Their study conformed that the yaw angle has a profound effect on the vortex structures. It is worth to mentioned that there is only this article which reports the effect of yaw angle of the delta wing on the vortical flow structure. The non-slender wing which has an angle of $\Lambda \geq 55^\circ$ has recently takes attention of researches immensely.

Unmanned Combat Air Vehicles (UCAVs) capable of undergoing severe maneuvers would be a major tactical advantage. Current and future configurations of the UCAVs are presented in Figure 1.8. The assumption is that the maneuverability of all these configurations will be limited by the onset of vortex breakdown and stall phenomenon, which, in turn, dictates both the overall forces and moments on the aircraft. Moreover, with the current trend towards lighter aircraft, an increasingly important limitation will be the onset of vibration and potential failure of aerodynamic surfaces of the UCAV arising from buffeting.



Figure 1.8. Current and future unmanned combat air vehicles and fixed-wing micro air vehicles, (Gursul et. al., 2005).

2. PREVIOUS STUDIES

2.1. Flow Structure around Delta Wings

2.1.1. Delta Wings with High Sweep Angle

There is considerable knowledge about the unsteady flow structure around slender delta wings. For example, Erickson et al. (1989) made a series of experiments with a sweep angle $\Lambda=65^\circ$ cropped delta wing with and without LEX (Leading Edge Extension) at Mach numbers from 0.40 to 1.60 as a freestream. Obtained data and performed analysis improved the understanding of the vortex development, interaction, and breakdown characteristics of a delta wing with LEX. Kegelmann and Roos (1989) investigated systematically the effects of leading-edge profiles on the flow over delta wings with a sweep angle $\Lambda=70^\circ$. They concluded that the shapes of the leading edges significantly affect the burst of leading-edge vortices. They found that the leading edge of a delta wing with positive camber generated greater vortex lift than that with the negative camber based on the force measurement results. Ericsson (1995) reviewed the existing data on the evolution of aerospace vehicles towards ever-increasing maneuverability, including flight at high angles of attack and vehicle motions of large amplitudes and high angular rates: His extensive review work divides the available literature, on the topic of predictions of vehicle aerodynamics that are dominated by unsteady separated flow effect, into four categories: i) Cause and effect of asymmetric forebody flow separation with associated vortices. ii) Cause of slender wing rock. iii) Effect of vehicle motion on dynamic airfoil stall. iv) Extrapolation from subscale tests to full-scale free flight. Gong et al.(1998) made experiments for a better understanding of the vortical flow past a highly swept delta wing equipped with double vortex-flaps. Two optical techniques including the Laser-lightsheet with artificial particulates put in the test-section and the Schlieren photography were used for steady/unsteady flow visualization in the low and high speed wind-tunnel respectively. They made a comparison between these two types of experimental results and stated that the

Laser-light-sheet and Schlieren techniques are good measures appropriate for visualization tests. It is possible to get photographs with satisfactory quality showing the complex phenomena of the vertical flow by careful manipulation, but it needs making further efforts to have more effective new technologies developed to promote the investigation of fine structures, mechanism and the evolution of the vertical and turbulent flow. The quantitative, time-averaged features of occurrence of small-scale vortical (sub-vortical) structures have been assessed in detail by Riley and Lawson (1998), who undertook an extensive study, using Laser Doppler Anemometry (LDA), of the flow structure on a wing of sweep angle $\Lambda = 85^\circ$. On the basis of averaged vorticity measurements, they revealed a system of steady, co-rotating, small-scale vortices. Özgören et al.(2002) proposed a criteria for onset of vortex breakdown and vorticity fluctuations at high angle of attack by using global and instantaneous vorticity results which were computed from the high-image-density particle image velocimetry (PIV) data. Their delta wing model was highly swept which had $\Lambda=75^\circ$ and they observed the flow structure at angle of attacks of $\alpha=24^\circ, 30^\circ, 32^\circ$ and 35° . The coexisting concentrations of azimuthal vorticity had been identified by using an equation suggested in the article and Particle Image Velocimetry (PIV) results. They concluded that there are three basic classes of vorticity concentrations summarized as follows:

- 1) Concentrations of azimuthal vorticity due to a centrifugal instability of the vortex have relatively small values of wavelength and circulation. The wavelength normalized by the local vortex diameter is in general accord with the recent numerical simulation of Sreedhar and Ragab for a free vortex in absence of a leading edge.
- 2) Concentrations due to vortex breakdown have significantly larger values of wavelength and large values of circulation. They are associated with the classical helical mode instability of breakdown.
- 3) Concentrations due to an unsteady instability from the leading edge have relatively large values of wavelength and moderate values of circulation. They apparently arise from reorientation of the unsteady layer vorticity shed from the leading edge.

Sohn et. al (2004) examined the vortical flow at sideslip of a delta wing with LEX through off-surface visualization of the wing leeward flow region. Angles of attack of 12° , 16° , 20° , and 24° were tested at sideslip angles of 0° , -5° , and -10° . The flow Reynolds number based on the main-wing chord was 1.82×10^5 . The wing vortex and the LEX vortex coiled around each other while maintaining comparable strength and identity at a zero sideslip. The increase of angle of attack intensified the coiling and shifted the cores of the wing and LEX vortices inboard and upward. By sideslip, the coiling, the merging and, the diffusion of the wing and LEX vortices increased on the windward side, whereas they became delayed significantly on the leeward side. Also the migration behavior of vortices on the windward and leeward sides of the wing changed considerably. The present study confirms that the sideslip angle has a profound effect on the vortex structure and interaction of a delta wing with LEX, which characterized the vortex-induced aerodynamic load. Atashbaz and Ommian (2006) made a series of qualitative and quantitative experimental investigations into the effect of angle of attack and sideslip on the aerodynamic behavior of a sharp leading-edge with $80^\circ/60^\circ$ sweep angles of double delta wing. Surface oil-flow and laser light sheet visualizations, as well as surface pressure measurements, were performed on the strake and wing upper surface. The following observations are made:

- A) Suction peak increases with increasing angle of attack symmetrically on both sides of the double delta wing before vortex breakdown occurs.
- B) Increasing sideslip causes strong asymmetric vortices over starboard and port sides of the wing, which develops different lift characteristics and as a result causes rolling moment. This may produce difficulties in stability and control of the wing.

Konrath et al.(2008) aimed, first, to describe the problems to cope with when applying these measurement techniques under difficult conditions as they arise in transonic wind tunnel facilities, and second, to show possibilities of a combined PSP (Pressure Sensitive Paint)/PIV application for flow visualizations. The measurements were split into two test groups. The first group comprised PSP measurements, which serve as “pathfinder” tests. Their results provide first information of the flow

topology over the delta-wing for a large range of angles of attack. In a second test group PIV measurements were performed for which specific angles of attack and locations of the measurement planes above the delta wing were selected on the basis of a first analysis of the PSP results. The measured velocity fields provide detailed information of the flow field.

There are more researches to simulate the flow structure of slender delta wings. For example, Pidd and Smith (1991) introduced a small change in the positions of the originally stationary symmetric/ asymmetric conical vortices into the flow near the body tip. Under the assumptions of the slender-body theory, they studied the growth of such disturbances in the downstream direction. They showed that the stationary symmetric vortex pairs were convectively stable in a narrow band of values of the incidence parameter, whereas the stationary asymmetric vortex pairs are convectively stable, with insignificant exceptions. Degani (1991,1992) and Levy et al. (1996) studied the separation of vortices over a 3.5-caliber tangent-ogive-cylinder body of revolution at low speeds by numerical computations using a time-accurate Navier– Stokes method. They found that it is necessary to maintain a fixed small geometric disturbance near the body apex to obtain and keep an asymmetric vortex pattern from the originally symmetric vortex pattern in their numerical computations. This numerical finding coupled with an experimental observation of Degani and Tobak (1992) led them to believe that a convective instability mechanism was responsible for the onset of asymmetry of the otherwise symmetric vortices over a slender body of revolution with a pointed nose. Cai et. al. (2003) developed a general stability condition for vortices in an arbitrary two-dimensional flow. A conical slender-body theory is then developed to reduce the study of stability of symmetric vortices over slender conical bodies at high angles of attack to a two-dimensional problem where the general stability condition may be applied. Slender circular cones and highly swept delta wings with and without fins, and slender elliptic cones of various eccentricities are studied. Cai et. al. (2004) extended their previous stability analysis to include asymmetric vortices over slender conical bodies. Theoretical analyses were presented for the stability of symmetric and asymmetric vortex pairs over slender conical wings and bodies under small

perturbations in an inviscid incompressible flow at high angles of attack and sideslip. The three-dimensional problem of a pair of vortices over slender conical wings and bodies is reduced to a problem in two dimensions by using the conical flow assumption and classical slender-body theory. The stability of symmetric and asymmetric vortex pairs over flat-plate delta wings, slender circular cones, and elliptic cones of various thickness ratios are examined. Results are compared with available experimental data. The following conclusions are drawn.

1. Stationary symmetric vortex pairs over a flat-plate delta wing at zero sideslip are always stable. No stationary asymmetric vortex pairs exist for a flat-plate delta wing without sideslip. With nonzero sideslip, the originally symmetric vortex pairs become asymmetric but remain stable under any small perturbations.
2. Both symmetric and asymmetric conical vortex pairs exist over slender circular cones at large angles of attack with either symmetric or asymmetric separations but none of them are stable. An implication is that a stable asymmetric vortex pair over a circular cone at sufficiently high angles of attack shall be in general non-conical or curved. This may explain the large number of experiments where asymmetric curved vortices appear over circular cones and ogive cylinders. However, it also conflicts with the observation of some symmetric and asymmetric conical vortex pairs in a few limited experiments of circular cones. Further investigation is needed to clarify this discrepancy.
3. Flattening the cross section of a circular cone in the transverse direction improves the stability of the vortices. There exists an elliptic cone with an intermediate finite thickness ratio between the circular cone and the flat-plate delta wing across which the symmetric vortex pair changes from being unstable to stable for a fixed K and fixed symmetric separation lines. For any fixed K , there is also a critical thickness ratio below which no asymmetric stationary vortex pair can be found under the condition of symmetric separations.

4. The locations and the stability of the stationary vortex pair over a highly swept thin delta wing with round leading edges are sensitive to slight shifts of the separation positions around the leading edge. When the separation positions on the leading edges are slightly asymmetric the originally symmetric stationary vortex pair becomes largely asymmetric, which can be stable within a certain range of separation angles. This sensitivity can be used for control purposes.

Cai et. al. (2008) studied a time-accurate three-dimensional Euler code to validate and confirm the stability analysis of Cai et. al. (2003, 2004). Complete three-dimensional flows at typical flow conditions that vary from stable to unstable regimes as determined by the stability analysis in (2003, 2004) are computed by an Euler flow solver. Stationary vortex configurations are first captured by running the Euler code in its steady-state mode until the residual in the continuity equation is reduced by more than 11 orders of magnitude, starting from the uniform free stream condition. After a stationary-vortex-flow configuration is obtained, a transient asymmetric perturbation consisting of suction and blowing of short duration on the left- and right-hand sides of the wing is introduced to the flow and the Euler code is run in time-accurate mode to determine if the flow will return to its original undisturbed condition or evolve into a different steady or unsteady solution. The former case indicates that the original stationary vortex configuration is stable to the applied perturbations, whereas the latter case proves it unstable or neutrally stable if the flow would continue oscillating around the original stationary solution. Strict conical bodies are studied to avoid confusion with other types of axisymmetric but non-conical slender bodies.

2.1.2. Delta Wings Having Low-Moderate Sweep Angle

Honkan and Adreopoulos (1997) determined patterns of instantaneous vorticity on a delta wing of sweep angle, $\Lambda = 45^\circ$ via a pointwise technique, and identified the existence of stationary discrete vortical structures, within the feeding

sheet and the primary vortex. Furthermore, they determined turbulence intensity in regions of shear layer attachment and secondary separation. Miao et al. (1995) investigated the flow patterns on a wing of sweep angle, $\Lambda = 50^\circ$, with a focus on the consequences of leading-edge profile. Yaniktepe and Rockwell (2004) aimed at investigating the unresolved concepts which are averaged structure of shear layer from leading edge of wing, unsteady features of separated layer adjacent to the surface of wing and control of flow structure by leading edge perturbations about flow structure of low sweep delta wings using of a technique of high-image-density Particle Image Velocimetry (PIV) and appropriate processing of selected and cinema sequences of images. They concluded that The flow structure on a delta wing of low sweep angle exhibits a number of distinctive characteristics relative to the case of a slender delta wing. Their conclusions are;

- 1) The time-averaged flow structure shows a number of distinctive features relative to the structure on wings of relatively high sweep angle. Patterns of averaged velocity show a relatively narrow elongated region of low velocity immediately adjacent to the surface of the wing, which is bounded by a higher speed region.
- 2) Unsteadiness of the flow structure is represented by patterns of rms velocity fluctuation w_{rms}/U normal to the surface of the wing, as well as Reynolds stress correlation $(v'w')/U^2$, both of which are essentially coincident with maxima of the averaged vorticity (ω) of the separated layer.
- 3) The instantaneous structure of the flow is represented by patterns of instantaneous vorticity, which take the form of well-defined concentrations. At sufficiently low angle of attack, these individual concentrations of vorticity retain their identity, whereas at moderate and moderately high values of angle of attack, both smaller-scale and larger-scale concentrations are evident.
- 4) When the wing is subjected to small-amplitude perturbations, substantial alterations of both the instantaneous and time-averaged structure were observed. The most effective frequency of excitation corresponds to the subharmonic of the broadband fluctuations in the region of the shear layer

closest to the leading edge, though this criterion is not necessarily universal for other geometric and flow parameters.

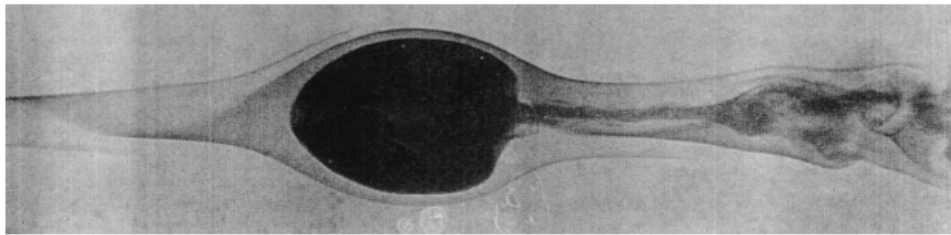
Yaniktepe and Rockwell (2005) characterized the instantaneous and averaged flow structure on diamond and lambda planforms by using a technique of high-image-density particle image velocimetry. Emphasis is on the structure in the trailing-edge region, over a range of angle of attack. Elongated layers of vorticity in the crossflow plane exhibit well-defined mean (time-averaged) and instantaneous concentrations of vorticity. These features are interpreted in conjunction with patterns of streamline topology, as well as images of rms velocity fluctuation and velocity spectra obtained from space–time imaging. The abrupt change in sweep angle, which is characteristic of both diamond and lambda planforms, along with the different trailing edge configurations of these planforms, yields distinctive features of the patterns, relative to the case of a simple delta wing. Woods and Wood(2000) investigated factors which define the buffet excitation with particular reference to planforms with low-observable characteristics of $\alpha=40^\circ$ swept semispan lambda planform for the cases of forward and reverse flow directions. They had carried out the experiments in wind tunnel to measure the surface pressure of lambda wing. They realized the experiment at 25 m/s of free stream velocity and acquired data for 60 seconds. Mean pressure distributions and RMS pressure distributions were plotted on semi-span wing for both forward and reverse flow directions. They concluded that, vortex burst is certainly present forward of the trailing edge at incidences greater than 10° . In reverse orientation similar levels of lift are produced but strong, stable asymmetries are present in the flow. Also, they stated that, maximum buffet is located in board of the leading edge vortex core and three distinct frequencies are detected in this area. Ghee and Taylor (2004) investigated a semi-span lambda wing with high-lift configuration which have same part to induce the lift coefficient called as trailing edge and leading edge flap and shroud. The result showed the dependence of flap height and overhang which can be defined as the horizontal distance from the trailing edge of the shroud to the leading edge of the trailing edge flap, trailing edge flap angle, shroud angle, Reynolds number and Mach number on aerodynamic

performance. The required data were acquired in the topics of force, moment, surface pressure and surface flow visualization. They stated that, the wing had a significant pitch up that would limit the usable lift of the air vehicle. The lift coefficient at the pitch up was found to increase with increasing Reynolds number at constant Mach number. There is no significant effect when Reynolds number is kept constant with changing in Mach number. Also, shroud angle had a detrimental effect on lift coefficient at pitch up but a benefit to the maximum lift to drag ratio. Ol and Gharib (2001, 2003) undertook an experimental investigation of wings of $\Lambda = 50^\circ$ and 65° . They characterized the onset of vortex breakdown using dye visualization and, via a stereo PIV technique, characterized various features of the leading edge vortex structure, including a large-scale collapse of the rolled-up, leading-edge vortex. Taylor et al. (2003) characterized the vortex flow patterns on a wing of low sweep angle and in a further investigation. Yavuz et al. (2004) investigated the near-surface topology and flow structure for a wing of sweep angle $\Lambda=38.7^\circ$, including the effect of wing perturbations and transient motion of the wing; a near-surface technique of PIV was employed. Elkhoury et al. (2004) have investigated to provide various measurements of the visualized dye patterns, including the degree of interaction of vortices, the onset of vortex breakdown, and the effective sweep angle of the wing root vortex, as a function of both Reynolds number and angle of attack Elkhoury et al. (2005) has investigated about the Reynolds number dependence of the near-surface flow structure and topology on a representative UCAV planform using a technique of high-image-density particle image velocimetry, in order to complement classical dye visualization. He expressed that Reynolds number is a critical effect on the double delta wing aerodynamics. Gursul et al. (2002) summarized recent investigations of low aspect ratio wings and planforms and, furthermore, provide insight into the phenomena of vortex breakdown visualized by dye injection. Gursul et al. (2005) reviewed unsteady aerodynamics of nonslender delta wings, covering topics of shear layer instabilities, structure of nonslender vortices, breakdown, maneuvering wings, and fluid/structure interactions. They compared experimental and computational results cited there in.

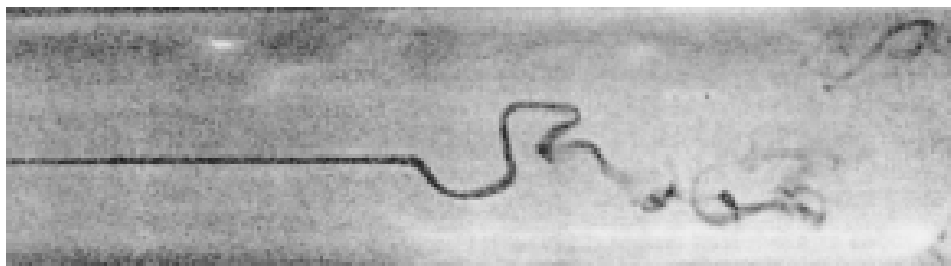
2.2. Vortex Breakdown

One of the most important formations of vertical flow on the delta wing surface is vortex breakdown. There are more studies, both experimentally and theoretically, for understanding formation mechanism and controlling the vortex breakdown. Studies about vortex breakdown can be summarized as follows:

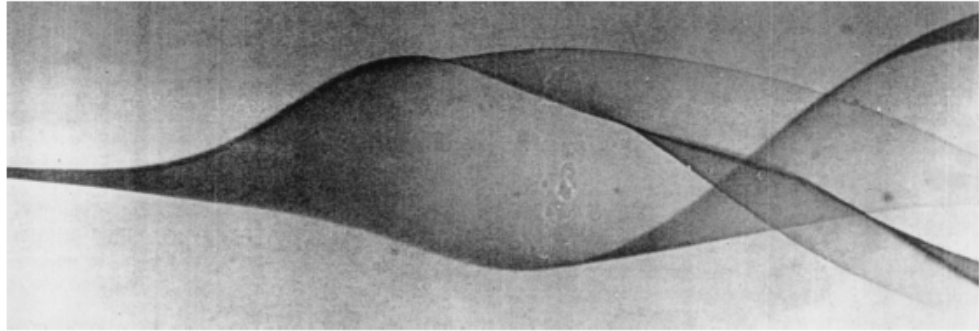
Sarpkaya (1971) performed experiments in swirling flows in a diverging cylindrical tube in which various types of vortex breakdown were observed. He stated that there are three basic types of stationary vortex breakdown: double helix, spiral and axisymmetric or bubble. Then, he (1995) declared that at high Reynolds numbers ($Re=22500$), vortex breakdown geometry gradually arrives at its cone-like form. He considered fourth fundamental type of vortex breakdown (the conical type) in addition to the double-type, spiral and nearly axisymmetric type.



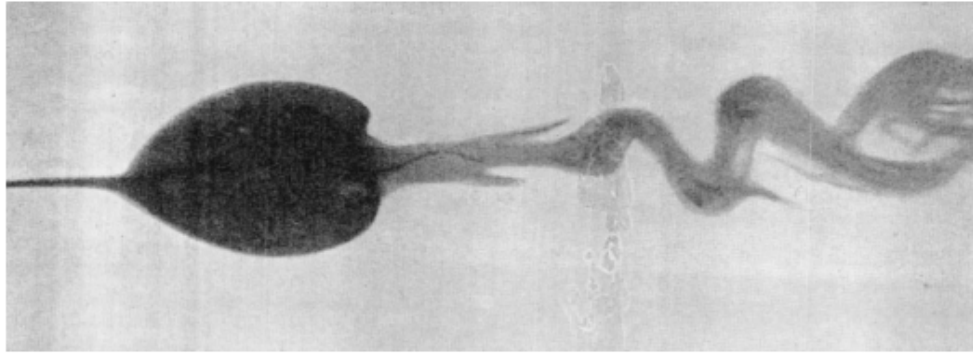
a) Bubble type breakdown



b) Spiral type breakdown



c) Double helix breakdown



d) Bubble breakdown followed by a spiraling tail

Figure 2.1. Types of vortex breakdown (Sarpkaya, 1971)

Payne et al. (1988), proposed an interpretation in a study of vortex breakdown over a delta wing. The core in a bubble form of breakdown seems to expand around an oval-shaped recirculation zone, at the exit of which it appears to shed in the form of vortex rings that are then convected downstream. The authors believed that these 'vortex rings' were actually a consequence of a tightly wound spiral tail originating from the downstream end of the bubble. Delery (1994) stated that the three-dimensional flows, boundary-layer separation leads to the formation of vortices formed by the roll up of the viscous flow sheet, previously confined in a thin layer attached to the wall which suddenly springs into the outer non-dissipative flow. Such vortices appear in a large number of circumstances and they often play dominant role in the overall flow properties. The strength of primary vortex steadily increases with the angle of attack, until disorganization occurs in the case of a delta wing. It is known as "vortex breakdown". Akilli et al. (2001) have investigated the sensitivity

of vortex breakdown. They have studied that a small wire oriented orthogonally to the axis of the leading-edge vortex on a delta wing at high angle-of-attack generates substantial changes in the vortex structure, which is characterized using a technique of high-image-density particle image velocimetry. They have used a wire having a diameter two orders of magnitude smaller than the diameter of the leading-edge vortex prior to the onset of vortex breakdown. They concluded that a wire can substantially advance the onset of breakdown by as much as fifteen vortex diameters. They have found that depending upon the dimensionless diameter of the wire and wire location along the axis of the vortex, the onset of vortex breakdown can occur either upstream or downstream of the wire. They also showed that contours of constant velocity indicating the rate of decrease of streamwise velocity along the centerline of the vortex is substantially enhanced, even for locations well upstream of the wire, relative to the case of vortex breakdown in absence of a wire. They also conclude that patterns of instantaneous vorticity in presence of the wire typically exhibit a form characteristic of either a spiral- or bubble-like mode of breakdown that occurs in absence of the wire. It is possible to classify the pressure fluctuations on the surface of the delta wing in terms of dimensionless frequencies which, in turn, represent various features of the flow unsteadiness, including the onset of vortex breakdown. Gursul and Yang (1995) were studied the relationship between the helical mode instability and the unsteadiness of vortex breakdown location. Flow visualization and velocity measurements using Laser Doppler Anemometry (LDA) were carried out over a delta wing. The results of this investigation showed that the fluctuations of vortex breakdown location occurred at much lower frequencies than the frequency of the hydrodynamic instability of the flow in the wake of the vortex breakdown in their investigation. And, they recommended that the helical mode instability does not affect the unsteady nature of breakdown location. Şahin et al. (2001) concluded that substantial retardation, or delay, in the onset of vortex breakdown, and there by development of large-scale concentration of vorticity due to the helical mode of vortex breakdown, are attainable when the leading edge of the positioned in the wake-flow region is perturbed at a natural frequency of vortex breakdown. In their experiment, a leading-edge vortex, which was generated from a

delta wing, impinged upon a plate having a sharp leading edge. The distance between the trailing edge of the delta wing and the leading edge of the plate was maintained at $L=73$ mm. They also found out that upstream movement of the onset of vortex breakdown in the leading-edge of the delta wing can also be substantially altered by insertion of a wire oriented orthogonally to the axis of the vortex and aligned with the centerline of the leading edge vortex. Akilli et al. (2001) used a small wire oriented orthogonally to the axis of the leading-edge vortex on a delta wing at high angle of attack generates substantial changes in the vortex structure, which is characterized using a technique of high-image-density particle image velocimetry. It is demonstrated that an extremely small wire having a diameter two order of magnitude smaller than the diameter of the leading-edge vortex prior to the onset of vortex breakdown can substantially advance the onset of breakdown by as much as fifteen-vortex, the onset of vortex breakdown by as much as fifteen-vortex diameter depending upon the diameter of the wire and wire location along the axis at the vortex, the onset of vortex breakdown can occur either upstream or downstream of the wire. They concluded that a wire can substantially advance the onset of breakdown by as much as fifteen vortex diameters. They have found that depending upon the dimensionless diameter of the wire and wire location along the axis of the vortex, the onset of vortex breakdown can occur either upstream or downstream of the wire. They also showed that contours of constant velocity indicating the rate of decrease of streamwise velocity along the centerline of the vortex is substantially enhanced, even for locations well upstream of the wire, relative to the case of vortex breakdown in absence of a wire. It is also concluded that patterns of instantaneous vorticity in presence of the wire typically exhibit a form characteristic of either a spiral- or bubble-like mode of breakdown that occurs in absence of the wire. Cui et al. (2007) proposed a control method which is referred to as freebody slot blowing that exploits the benefits of both the spanwise slot blowing and the effectiveness of canards. Flow visualizations show that this technique can be used to delay vortex breakdown on a delta wing more effectively than some existing blowing techniques. However, due to the constraints of the experimental setup, the study did not resolve the issue of why a single sided blowing delays the formation of vortex breakdown on

the blowing side but has an opposite effect on the non-blowing side. Then, Cui et. al. (2008) attempted to address this issue by systematically isolating the possible causes. To this end, a delta wing-body configuration model that effectively incorporates two separate compartments for blowing was fabricated. This model also enables them to carry out force measurement and to evaluate the aerodynamic effects of symmetrical and differential forebody slot blowing.

3. MATERIAL AND METHODS

3.1. Channel System

Experiments were conducted in a large scale and circulating free-surface water channel. The internal dimensions of the water channel are of 8000 mm \times 1000 mm \times 750 mm which is made from 15 mm thick transparent plexiglass sheet with upstream and downstream fiberglass reservoirs. Before reaching the test chamber, the water was pumped into a settling chamber and passed through a honeycomb section and a 2:1 channel contraction. These reservoirs and honeycomb screen arrangements are used to maintain the turbulence intensity below 0.1 %. The water pump was driven by an electric motor with a variable speed controller. A schematic of the test chamber of present study is shown in Figure 3.1.

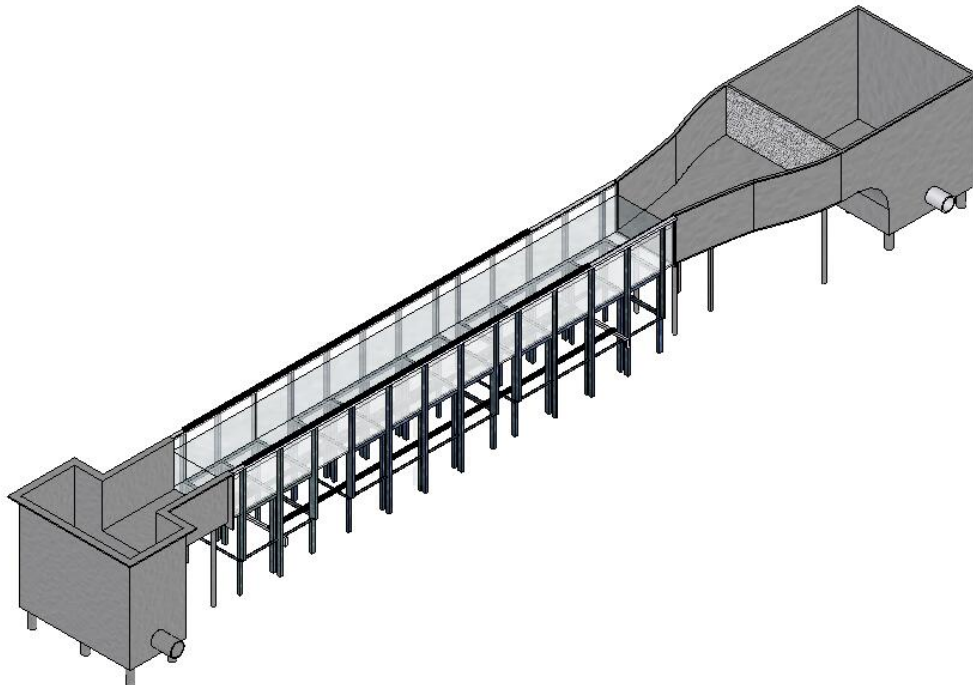


Figure.3.1. Schematic of the water channel

3.1.1. Experimental Apertures

In the present study, the delta wing was kept stable in water by using servo motor. A special aperture shown in Figure 3.2 was designed for servo motor and attack angles of the delta wing was adjusted by using specially designed mechanism which was connected to the servo motor. Servo system unit contained one servo motor, servo motor driver and control unit as shown in Figure 3.3. If a brief fundamental description of the servo system should be done, it can be explained as follows:

A servo motor has an output shaft which can be positioned to specific angular positions by sending the servo a coded signal. As long as the coded signal exists on the input line, the servo will maintain the angular position of the shaft. As the coded signal changes, the angular position of the shaft changes. The desired position of motor shaft can be provided by a control unit by sending suitable signals. Servo motor's shaft can be rotated by 180° .

The wing was maintained in a nominally horizontal position by a slender support strut that extended vertically from the midchord of the wing. This strut has a width of 4 mm and a streamwise length of 35 mm. Assessment of this type of strut arrangement involved comparison with complementary experiments involving a nominally horizontal sting and comparison of the location of vortex breakdown for wings of different attack and yaw angles. As a consequence, this strut arrangement has an insignificant effect on the flow structure on the leeward side of the wing.

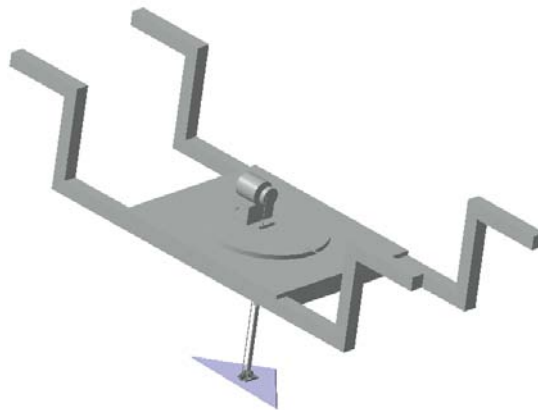


Figure 3.2. Sketch of the special aperture

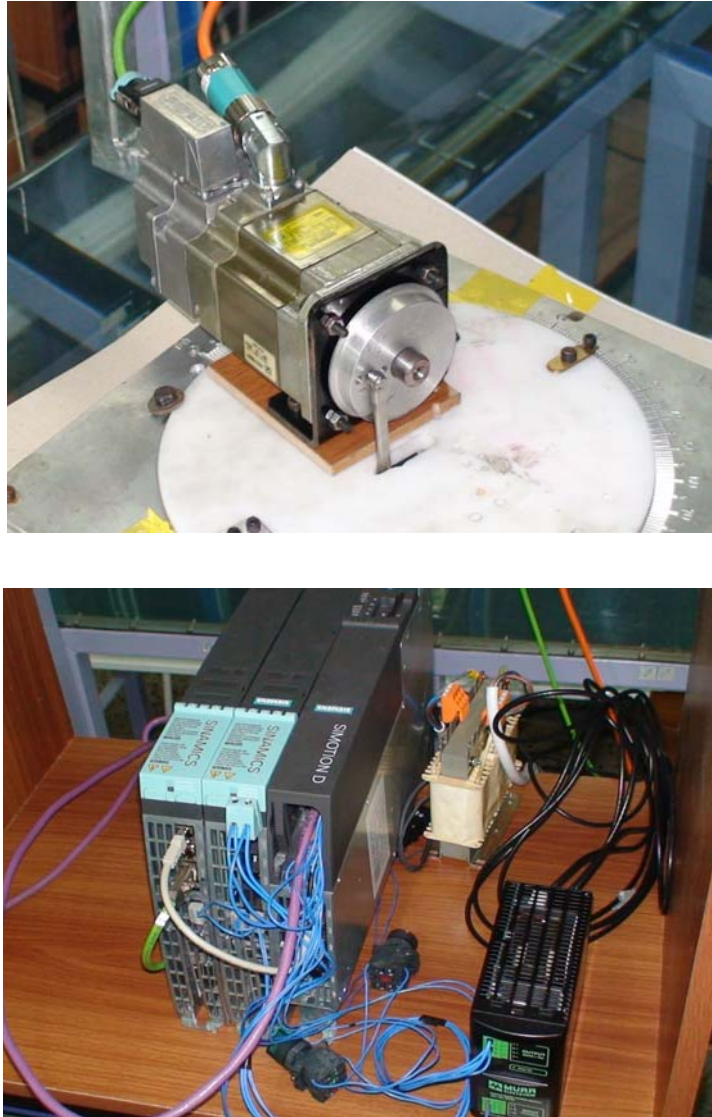


Figure 3.3. Servo Motor and its control Unit

3.2. Dye and Particle Image Velocimetry (PIV) Experiments

3.2.1. Dye Visualization Experiments

A fluorescent dye which shines under laser sheet was used to create color change in water to visualize flow characteristics over the delta wing during the dye experiments. Dye was located in a small container which is located 500 mm above

the free surface of the water channel. Dye was injected near field of the delta wing trailing edge by plastic pipe and dye was passed through a narrow and close channel in the delta wing to its apex. The video camera which was SONY HD-SR1 was used to capture the instantaneous video images of the vortex flow structures. The images were captured by frame grabber software of camera. The dye visualization technique gives no numerical information about flow structure of vortical flow, but demonstrates a brief and rough idea about flow structure over the delta wing.

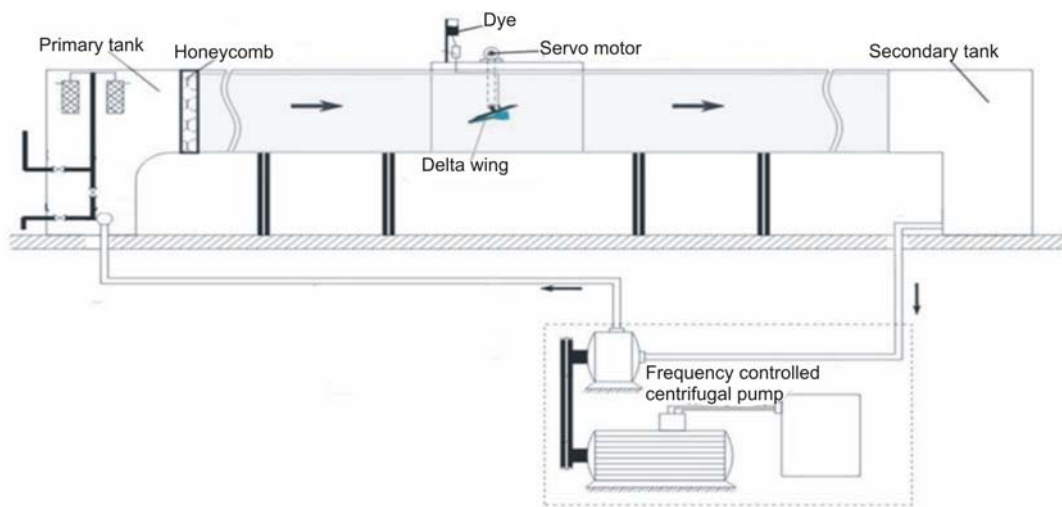


Figure 3.4. Schematics of channel and its mechanism

3.2.2. Particle Image Velocimetry (PIV) Experiments

3.2.2.1. Measurement Principle

Particle Image Velocimetry (PIV) is a Flow Measurement Technique which can be used to obtain the time dependent field velocity distributions of a single and multi-phase flows. Two-dimensional velocity field distribution can be obtained. The particle image velocimetry (PIV) technique provides a global view of the instantaneous flow field in a quantitative fashion. This allows the user to examine the presence of small flow structures and their influence, obtain vorticity fields quantitatively and, finally, obtain mean, turbulence and stresses globally. Particle

Image Velocimetry (PIV) determines the distance that the particles have moved in the time between laser illuminations. In general, a PIV system consists of illumination, image acquisition, particle seeding, and image processing and data analysis sub-systems. Laser light is commonly used as the illumination source in PIV systems. The particles are illuminated by pulsed sheets of light at precise time intervals to produce images that are recorded on a photographic film. Ideal tracer particles should be very small and follow the flow field. The most common methods to determine the distance are particle tracking and correlation methods. The correlation field shows the dominant distance between each particle and every other particle within the interrogation spot. The maximum intensity spot, which represents the correlation of each particle image with itself, is located in the center. A second peak, called the positive displacement peak that corresponds to the dominant particle spacing. After calculation of displacement of particles in a certain time, the velocity of flow field could be found. Using instantaneous velocity vector field, vorticity, streamline topology and turbulent statistics could be found by this technique. Average velocity field, vorticity contours, streamline topology and turbulent statistics could be calculated using instantaneous data. Measurement principle of stereoscopic (3D) PIV system is shown in Figure 3.5.

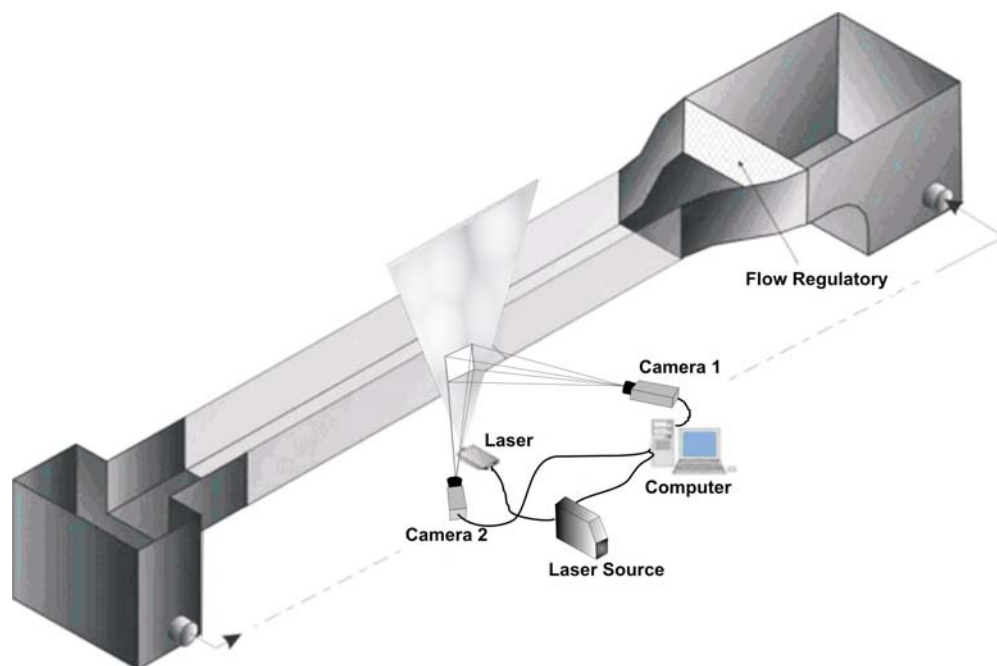


Figure 3.5. Schematic view of 3D PIV

3.2.2.2. Illumination

The illumination is realized by laser which is shown in Figure 3.6. In general laser is selected for this purpose to capture the images efficiently. In gas flow applications a high light source must be readily available for better illumination. The light is scattered by tracer particles to help taking images by the camera. Large tracer particles are used for this purpose because of their high scattering efficiency. Particles flowing with fluid simultaneously are very important parameter for selecting the type of tracer particle. Small particles achieve this parameter very easily than the large tracer particles. But generally this option is decided in the experiment by researcher. The duration of illumination light pulse must be as short as possible in order to prevent image blurring. There is a time delay between illumination pulses. This delay time must be as long as possible for determination of the displacement between images of tracer particles with enough resolution. But the time delay must be short enough to avoid particles with an out-of-plane velocity component leaving the light sheet between subsequent illuminations. The location and dimensions of the measurement plane should be well defined.



Figure 3.6. A Nd.YAG Laser Source

3.2.2.3. Adaptive Cross-Correlation Technique and Further Analysis

Historically, auto-correlation has been the most widespread method used because in the past it was not possible to separate the initial and final particle-positions on separate camera frames. Therefore, successive light-sheet pulses exposed the one camera image map. Inherently, this lead to an ambiguity in the measurements, since it was not possible to tell which of two recorded particle images was the initial and which was the final position. In recent years advances in camera technology have allowed initial and final particle positions to be registered on separate camera frames, and thus cross-correlation than adaptive correlation are be used without the directional ambiguity of auto-correlation (Dantec Dynamics Software Manual).

The fundamental principle of Adaptive correlation is an iterative procedure: From an initial guessed offset value, an offset is introduced from the first window (the interrogation area in the image frame from laser pulse one) to the second window. The obtained vector is validated and is used as a new estimate for the window offset. A new run is made, but this time with a smaller window (interrogation area). The main benefit derived from using the shifted window is capturing the particle images that left the interrogation area during the time between the two light pulses. Loss of these particle images is known as the "in-plane dropout", which reduces signal strength and, as a result, the number of successful vectors that can be obtained. Capturing more particle images for each vector permits the interrogation area to be refined while still obtaining an adequate number of successful vectors without increasing the seeding density in the flow. Images were received from CCD camera which has resolution of 1600×1186 pixels at a rate of 15 frames per second. The time delay changes from 2 ms and 3 ms between frames. Digital image was analyzed using FLOWMAP software. The image was recorded on a CDD array. A Frame Grabber in the computer read the camera image from CCD camera and stored it as the digital image file format (TIFF) in the RAM. This digital image was processed and analyzed using the FLOWMAP software. During each continuous run, a total 350 images were taken. In order to determine the velocity

field, a cross- correlation technique, with 32×32-interrogation window, was employed, with an overlap of % 50 (Dantec Dynamics Software Manual).

3.3. Experimental System

The test section consists of a delta wing has $C=101$ mm chord for PIV experiments and $C=140$ mm for dye experiments with sweep angle $\Lambda=40^\circ$ for both test models. The thickness of delta wing was 3mm. The delta wings which have 45° chamfer from windward side to its leeward side are made of plexiglas material. The depth of the water in the test section was adjusted to 530 mm height for the present experiments. Vortex breakdown formed in the various Reynolds numbers were observed qualitatively and quantitatively. Then, Reynolds number according to delta wings chord was kept constant for all experiment at $Re_c=10000$. Free-stream velocity of water is 97 mm/s for PIV experiments and 72 mm/s for dye experiments. Using the PIV technique, instantaneous velocity vectors were measured in a region illuminated by a two-dimensional laser sheet. Velocity vector measurements were carried out using Dantec PIV system. The flow field illumination was provided by two Nd:Yag pulsed laser sources of a wavelength of 532 nm, each with a maximum energy output of 120 mJ. Dantec Flow Map Processor which controlled the timing of the data acquisition was used for synchronizing the camera and laser units. The movements of the particles were recorded using a CCD camera with a resolution of 1600 x 1186 pixels. The camera was equipped with a 60 mm focal-length lens. Dantec flow grabber digital PIV software employing frame-to-frame adaptive correlation technique was used to calculate the raw displacement vector field from the particle image velocity data. In the image processing, 32 x 32 pixels with rectangular effective interrogation windows was used. During the interrogation process, an overlap of 50% was employed in order to satisfy Nyquist criterion. For the present investigation, the PIV experiments were conducted for two different crossflow planes which is called as plan-view and end-view, shown in Figure 3.13, respectively. The flow characteristics over the delta wing in plan-view plane was presented for both attack (α) and yaw(θ) angles for $\alpha = 7^\circ, 10^\circ, 13^\circ, 17^\circ$; $\theta = 0^\circ, 6^\circ,$

8° and 15°. The location of the laser sheet for end-view measuring planes was determined using the dye visualization technique in order to capture the major features of the flow structure. This end-view measuring locations corresponds to the streamwise location of $X/C=0.8$ in PIV experiments. To be able to understand the development of vortex structure over delta wing from end-view, the dye visualization experiments were done at $X/C=0.6, 0.8$ and 1 . On the other hand, for plan-view measuring planes the laser sheet was located at a location 0.5mm away the wing surface.

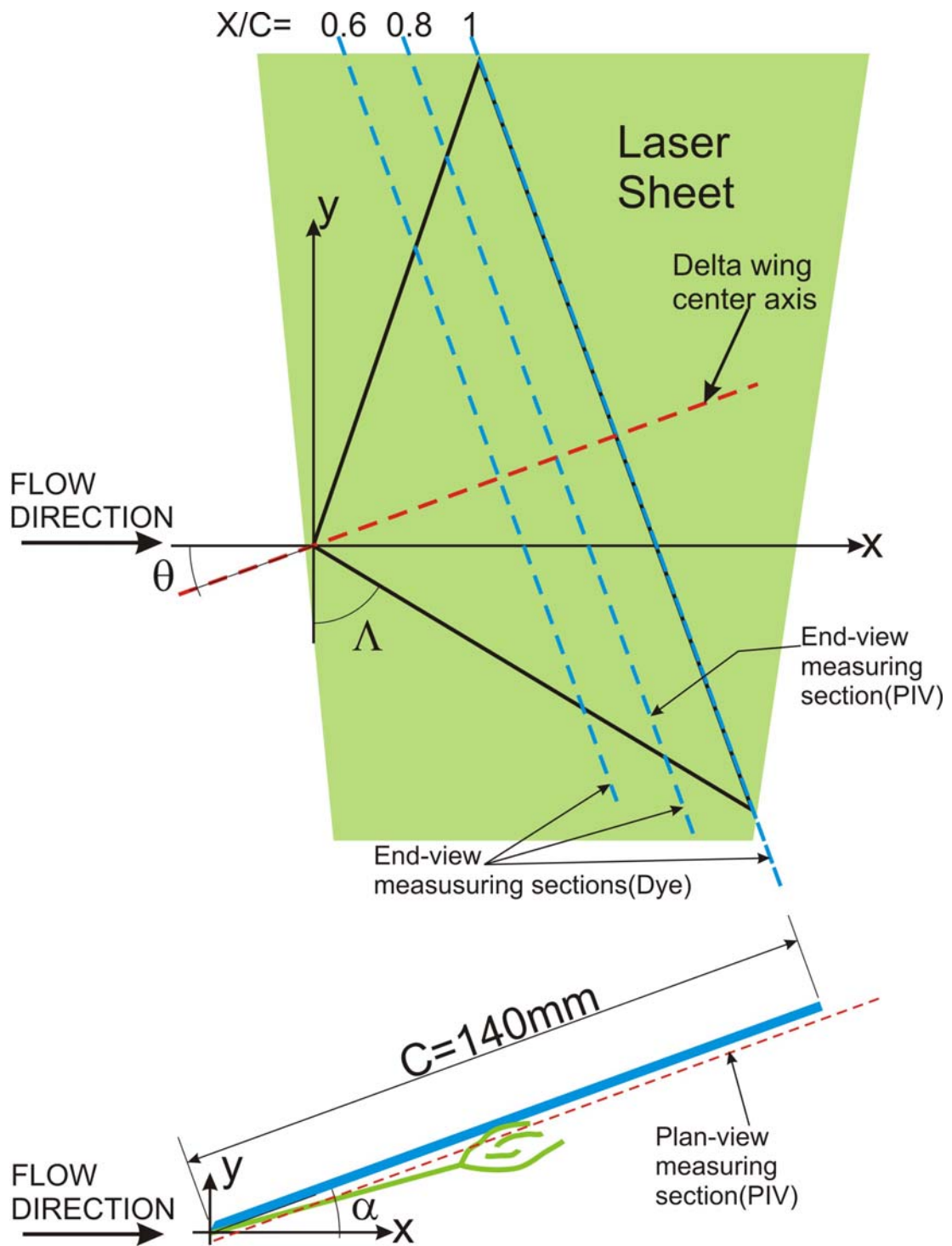


Fig 3.7. Schematic of experimental arrangement showing delta wing, laser sheet location, and definition of key parameters.

4. RESULTS AND DISCUSSION

4.1. Flow Structure on a Delta Wing of Low Sweep Angle

4.1.1. Dye Visualization Results

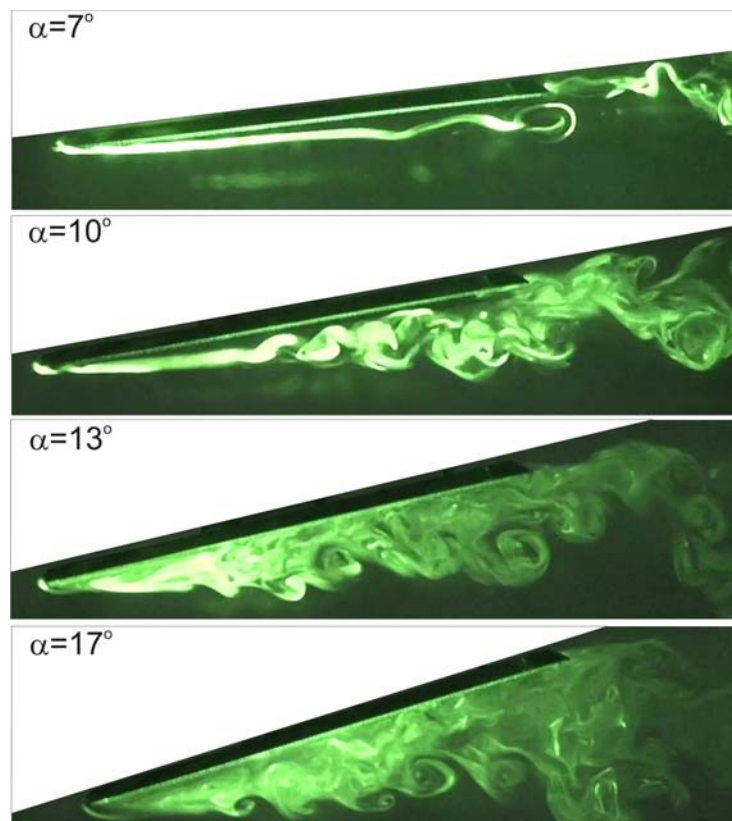


Figure 4.1. Dye visualization of flow in side-view plane over the delta wing

The behavior of flow structure below delta wings in side view planes are presented in Figure 4.1. As seen in the first image, spiral vortex is formed in close region of the delta wing surface having angle of attack as $\alpha = 7^\circ$. As it is known from the literature that the spiral vortex take place further away from the surface of the slender delta wing comparing to the present delta wing. The location of vortex breakdown moves in forward direction close to the leading edge of the delta wing when the attack angle increases. For example, the vortex breakdown occurs at delta

wing apex at a value of attack angle $\alpha=13^\circ$. The location of vortex breakdown moves forward and backward through its axis in unsteady mode. The flow structure of the delta wing becomes more complex and disorganized after occurrence of vortex breakdown. Furthermore, the delta wing produces separation vortices like submerged obstacle in flow field, when the angle of attack is $\alpha \geq 13^\circ$. Examining all images, it can be seen that, high scale Kelvin-Helmoltz vortex structure occurs at the bottom of the unstable flow region, especially for the attack angles of $\alpha=13^\circ$ and 17° . The leading edge vortices (spiral) places close to the surface of the delta wing. There is a strong interaction between vortical flow and wing surface. Angle between the delta wing and central axis of the spiral vortex slightly increases when the attack angle increases from $\alpha=7^\circ$ to 13° . Beyond $\alpha > 13^\circ$ the separated flow occupies the surface of the delta wing completely. Here the delta wing behaves like an obstacle placed in a free stream flow. Images of spiral vortex and vortex breakdown over the delta wing surface in the plan-view planes for attack angle $\alpha=10^\circ$ and yaw angle of $\theta=10^\circ$ are presented in Figure 4.2. As seen in this figure, there is a small size secondary spiral vortex on the upper side of the delta wing chord axis. This small size secondary vortex disappears after a definite time interval which is seen in second picture of the first row. After this disappearing of small secondary vortex, a reversed flow adjacent to the main spiral vortex is occurred in the certain period of time interval. Namely, circulatory flow is emanating from the main spiral vortex. After that, the small secondary vortex begins to appear. This small size circulating flow domain occurs due to the high yaw angle and it can also be seen at low yaw angles if all video recordings are observed. Since, the magnitude of this circulation is so weak, it is quite difficult to visualize at low yaw angles continuously.

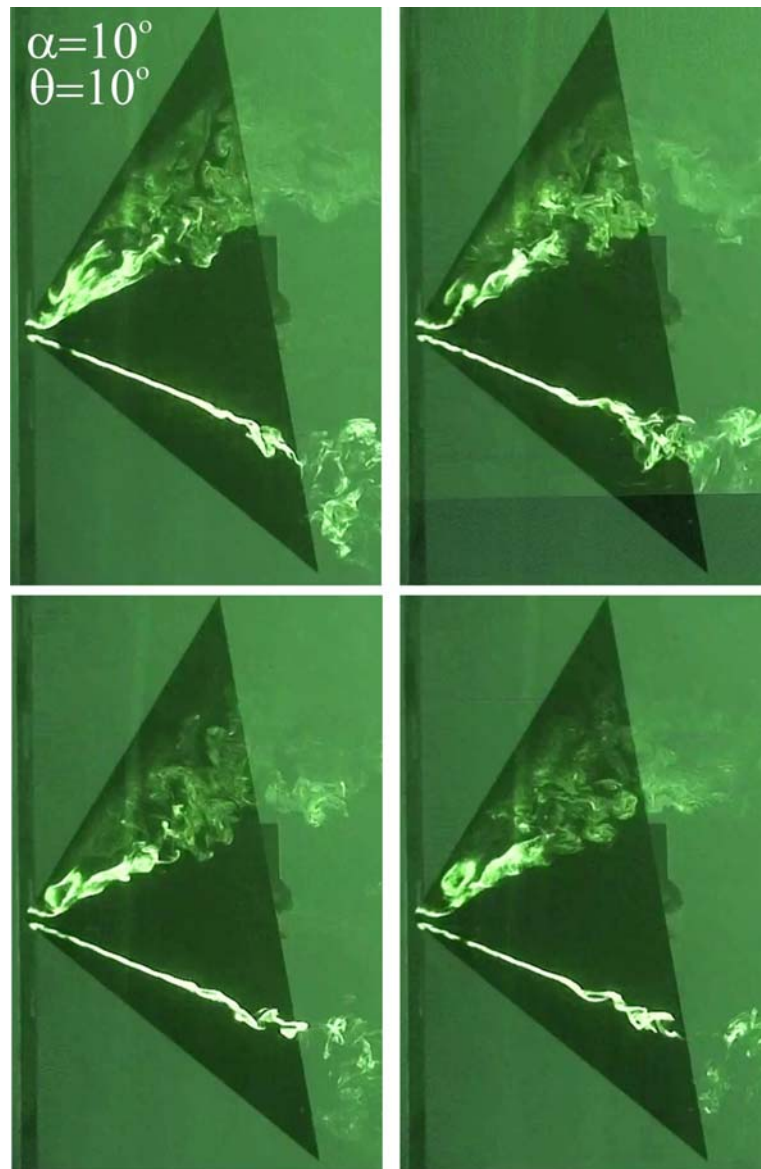


Figure 4.2. Formation and development of spiral vortex and vortex breakdown observed in plan-view plane.

The result of dye visualization experiments at angles of attack $\alpha=7^\circ$, 10° , 13° , 17° and having yaw angles as $\theta=0^\circ$, 2° , 4° , 6° , 8° , 10° and 15° are shown in Figures 4.3 and 4.4. In the first column of Figure 4.3 having $\alpha=7^\circ$ and 10° , the apparent centerlines of leading edge vortices are clearly identified and it is clear that, vortex breakdowns occurs after a definite distance from delta wing apex. The natural flow structure of the delta wing generally contains a pair of spiral vortices emanate from the leading edge of the delta wing and vortex breakdown occurs which is defined as decomposition of the spiral vortex at a definite distance from leading edge of the delta wing. As seen in the first row of the Figure 4.3, which is the case of zero yaw angle, the location of vortex breakdown comes closer to the delta wing apex as the attack angle is increased. Also, there is a symmetrical flow structure over the delta wing in the case of zero yaw angle. The vortex breakdown occurs at delta wing apex at a value of attack angle $\alpha=13^\circ$ as mentioned earlier. The wake flow region occupies the whole wing surface, as the angle of attack is increased to a value of $\alpha=17^\circ$. When the yaw angle increases, the symmetrical flow structure on both side of the chord axis of the delta wing deteriorates. The vortex breakdown location at the lower side of the delta wing chord axis is delayed comparing to opposite side. In other words, vortex breakdown occurs earlier at the upper side of the delta wing chord axis compared with the lower side. The secondary spiral vortex begins to appear at a yaw angle of $\theta=8^\circ$ for both cases of attack angles $\alpha=7^\circ$ and $\alpha=10^\circ$. At $\alpha=7^\circ$ and $\theta=15^\circ$, vortex breakdown occurs in the near region of delta wing's trailing edge. As seen in Figure 4.3 having the yaw angle less than $\theta=4^\circ$ the flow structure over the surface of the delta wing is symmetric. Examining the last row of images in Figure 4.3 indicates that there is a slight difference between flow structures on both side of the central chord axis of the delta wing. The yaw angle is more effective when the value of yaw angle is higher than $\theta=6^\circ$. For example, in the first column of Figure 4.3, the angle of attack is adjusted as $\alpha=7^\circ$ for all values of the yaw angle. As the yaw angle increases the central axes of both spiral vortices shift downward. Since the secondary vortex is not strong, it is quite difficult to identify by dye visualization, even though in the second column of images in Figure 4.3, a secondary vortex

appears at the upper side of the top spiral vortex. At $\theta=6^\circ$ locations of vortex breakdowns begin to change. For example, the location of the vortex breakdown for the lower spiral vortex takes place close to the trailing edge of the delta wing while the vortex breakdown at the top spiral vortex occurs further upstream close to the apex of the delta wing. As seen in the last image of the first column of Figure 4.4, the spiral vortex moves further down close to the lower side edge and the vortex breakdown occurs at a location further downstream of the trailing edge of the delta wing. In the second column of Figure 4.4, angle of attack is adjusted to $\alpha=10^\circ$ and yaw angle is varied from $\theta=6^\circ$ to $\theta=15^\circ$. It is interesting enough that through out the yaw angle range both spiral vortices are exist. The only thing is symmetrical structure of the vortical flow is not available any more. The top spiral vortex disappear when the yaw angle is set to $\theta=10^\circ$. Close to the apex of the delta wing, the top spiral vortex begins to create a reversed flow. The area of the circulatory flow region increases when the yaw angle increases to a value of $\theta=15^\circ$ as seen in the last image shown in the second column of Figure 4.4. The vortex breakdown location moves further downstream on the lower side spiral vortex. On the upper region of the midcord axis of the delta wing, a separated flow takes place at $\theta \geq 10^\circ$. Adjusting the angle of attack to a value of $\alpha=13^\circ$ and yaw angle to a value of $\theta=0^\circ$, a circulatory flow is developed in close region of the apex of the delta wing as seen in Figure 4.3. But having attack angle as $\alpha=13^\circ$ and yaw angle as $\theta=6^\circ$ as seen in Figure 4.4. The circulatory flow type only exists on the upper side of the central (midcord) axis of the delta wing. But on lower side the circulatory flow turns into the spiral vortex. The spiral vortex has a short length. Namely, vortex breakdown occurs close to the apex. Similar vortical flow structure takes places even increasing the yaw angle up to $\theta=15^\circ$ at an attack angle of $\alpha=13^\circ$. Increasing angle of attack furthermore to a value of $\alpha=17^\circ$, no more spiral vortex is developed over the delta wing. Separated flow is occupied whole surface of the wing surface. It is also quite difficult to see the circulatory flow motion close the apex of the delta wing.

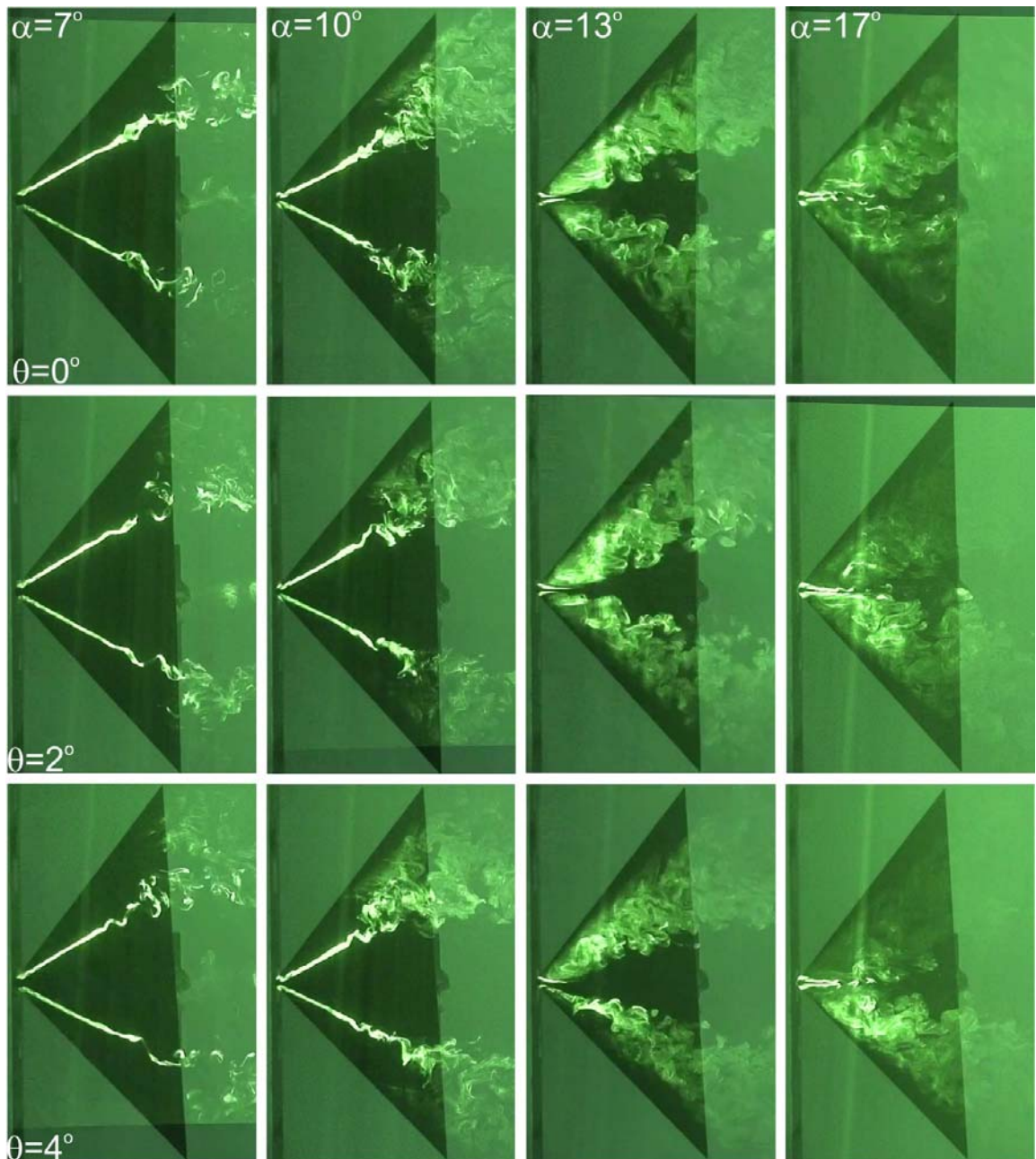


Figure 4.3. Formation and development of spiral vortex, vortex breakdown and separated flow region as a function of attack angle and yaw angle.

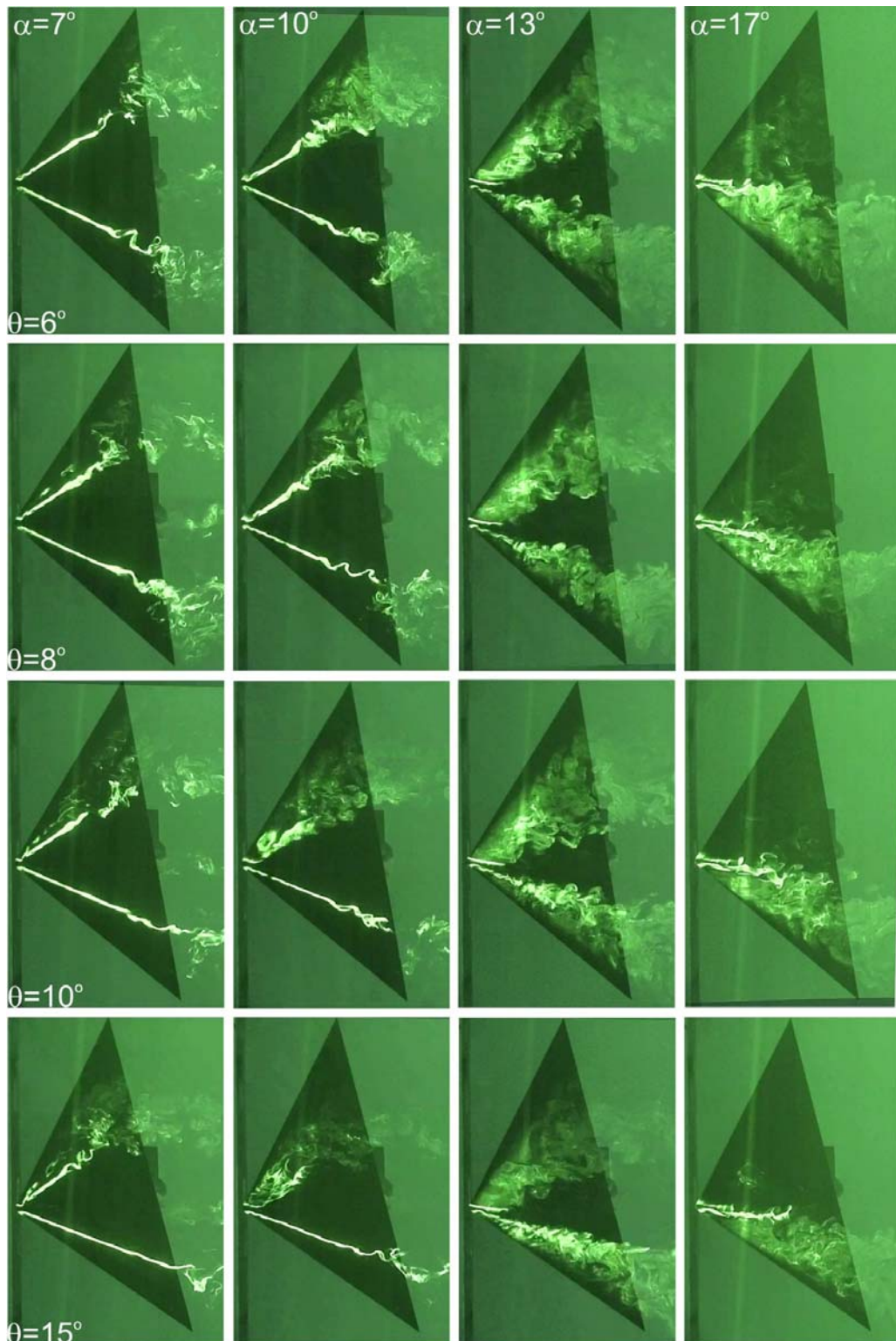


Figure 4.4. Formation and development of spiral vortex, vortex breakdown and separated flow region as a function of attack angle and yaw angle.

A representative images for the forward-backward motion of vortex breakdown locations in the free-stream flow direction in the case of zero yaw angle for attack angles of $\alpha=7^\circ$ and $\alpha=10^\circ$ is shown in Figure 4.5. The symmetry of the flow structure over the delta wing changes with time as seen in this figure. Generally, it can be seen that, the vortex breakdown occurs at the dimensionless chord axis of $X/C=0.8$ in the case of zero yaw angle. During the period of the observation, a spiral type vortex breakdown is observed in most of the time. The location of the vortex breakdown occurs on both upper and lower sides of spiral vortices changes disorderly. On both spiral vortices, a breakdown occurs at similar locations most of the time, or, have a same distance to the apex of the delta wing. At both angles of attack $\alpha=7^\circ$ and 10° , sometimes the upper vortex breakdown location is far away from the apex of the delta wing and sometimes lower vortex breakdown location is far away from the leading edge of the delta wing. Between central chord axis of the delta wing and the axes of both spiral vortices, the angle is 27° . On the other hand, the angle between side edges of the delta wing and the central axis of the spiral vortices is 23° . As long as the yaw angle is as $\theta=0^\circ$, these angles are continuously the same. When the attack angle increases to a value of $\alpha=10^\circ$ the vortical flow structure downstream of the vortex breakdown is more chaotic.

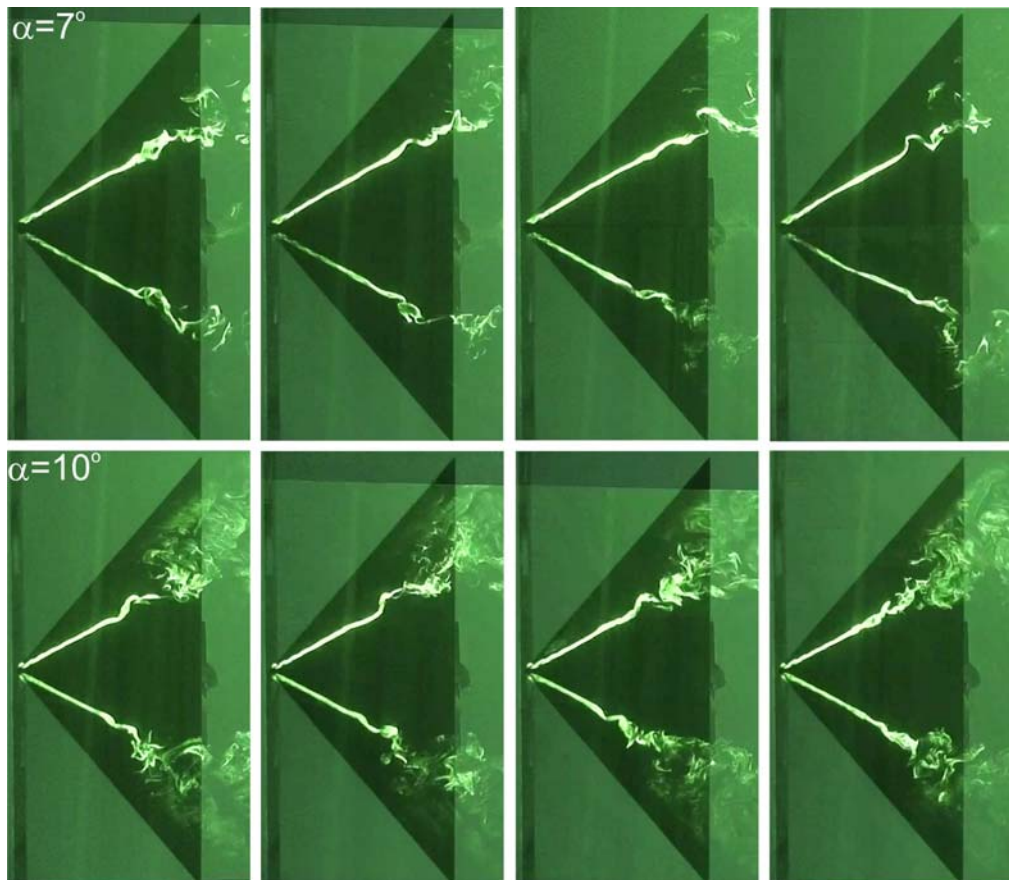


Figure 4.5. A representative images of vortex breakdown locations at $\theta=0^\circ$.

Dye observation was conducted in three different end-view planes such as $X/C=0.6, 0.8$ and 1 in order to study vortical flow structure at a crossflow plane further downstream of the vortex breakdown. As soon as spiral vortex breaks down a complex flow structure is developed. The main rotating vortices occur in the inner side of the leading edges close to the central axis of the delta wing. Small size vortices are also developed next to the main rotating vortices. These secondary vortices get smaller in size when it is moved close to the side edges of the delta wing. The outer line of the separated flow region gradually moves away from the surface of the delta wing as the end-view cross-section is moved further downstream in the free-stream flow direction. Namely, the diameter of the vortical flow structure downstream of the vortex breakdown increases gradually as this flow moves further downstream in the free-stream flow direction. Between surface of the delta wing and

vortical flow structure, there is a strong interaction. The intensity of this interaction gets lower at $X/C=1$ comparing to $X/C=0.6$. The non-steady flow structures caused by both spiral vortices are more or less is the same.

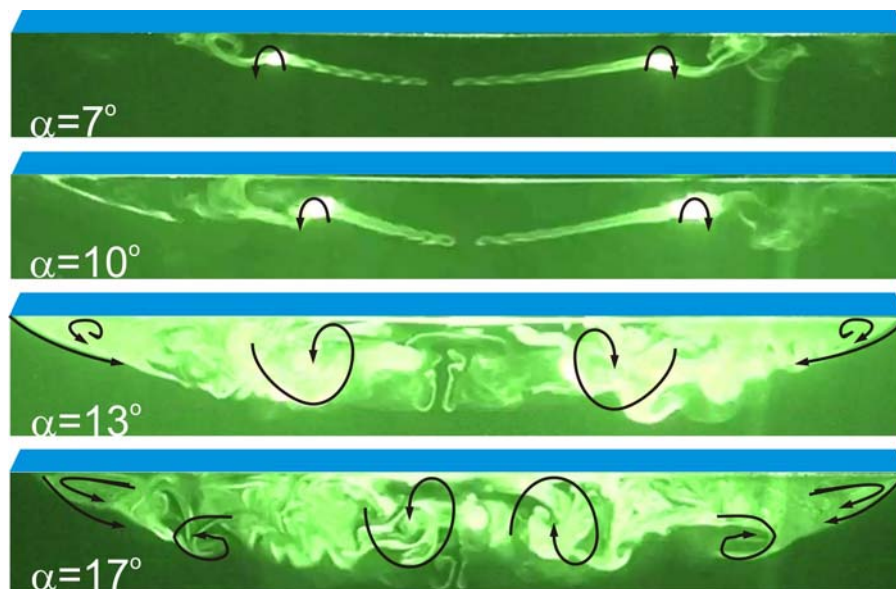


Figure 4.6. Formation and development of vortex structure in end-view plane at $X/C=0.6$, $\theta=0^\circ$.

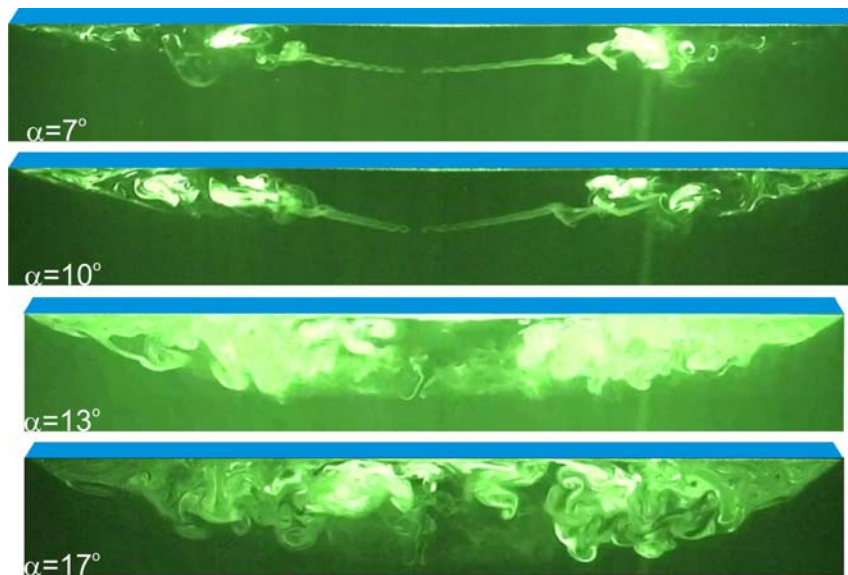


Figure 4.7. Formation and development of vortex structure in end-view plane at $X/C=0.8$, $\theta=0^\circ$.

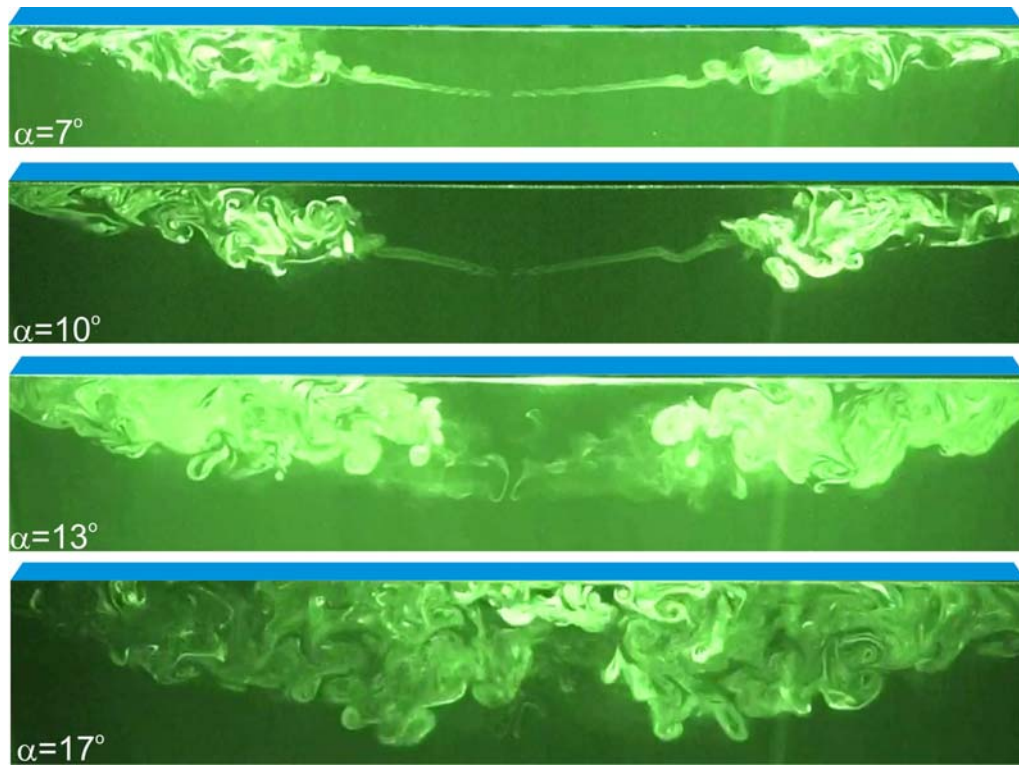


Figure 4.8. Formation and development of vortex structure in end-view plane at $X/C=1$, $\theta=0^\circ$.

4.1.2. Particle Image Velocimetry (PIV) Results

4.1.2.1. Patterns of Time-Averaged Vorticity, Streamline and Velocity Vectors Topology (End-View)

Patterns of time-averaged vorticity, $\langle\omega\rangle$, streamline, $\langle\Psi\rangle$, and velocity, $\langle V\rangle$ topology for angle of attack $\alpha=7^\circ, 10^\circ, 13^\circ$ and 17° in the cases of yaw angles such as $\theta=0^\circ, 6^\circ$ and 8° are shown in Figures 4.9-20. Laser sheet is located at $X/C = 0.8$ since previous dye experiments conducted on the same cross-section. The solid and dashed lines show the positive and negative time-averaged contours, respectively. To be able to make a comparison between experimental results, the minimum and incremental values of patterns of time-averaged vorticity are taken with same values for all experiments on end-view planes. For the time-averaged vorticity contours, minimum and incremental values are $[\langle\omega\rangle]_{\min}=0.3 \text{ s}^{-1}$ and $\Delta[\langle\omega\rangle]=0.3 \text{ s}^{-1}$, respectively. At first, end-view plane such as $X/C=0.8$, there is a symmetrical flow structure over the delta wing in the case of zero yaw angle as seen in Figure 4.8. The patterns of the time-averaged vorticity have an elongated shape with two vorticity extrema at zero yaw angle, $\theta=0^\circ$, and attack angle $\alpha=17^\circ$. In this case, there are three vorticity extrema.

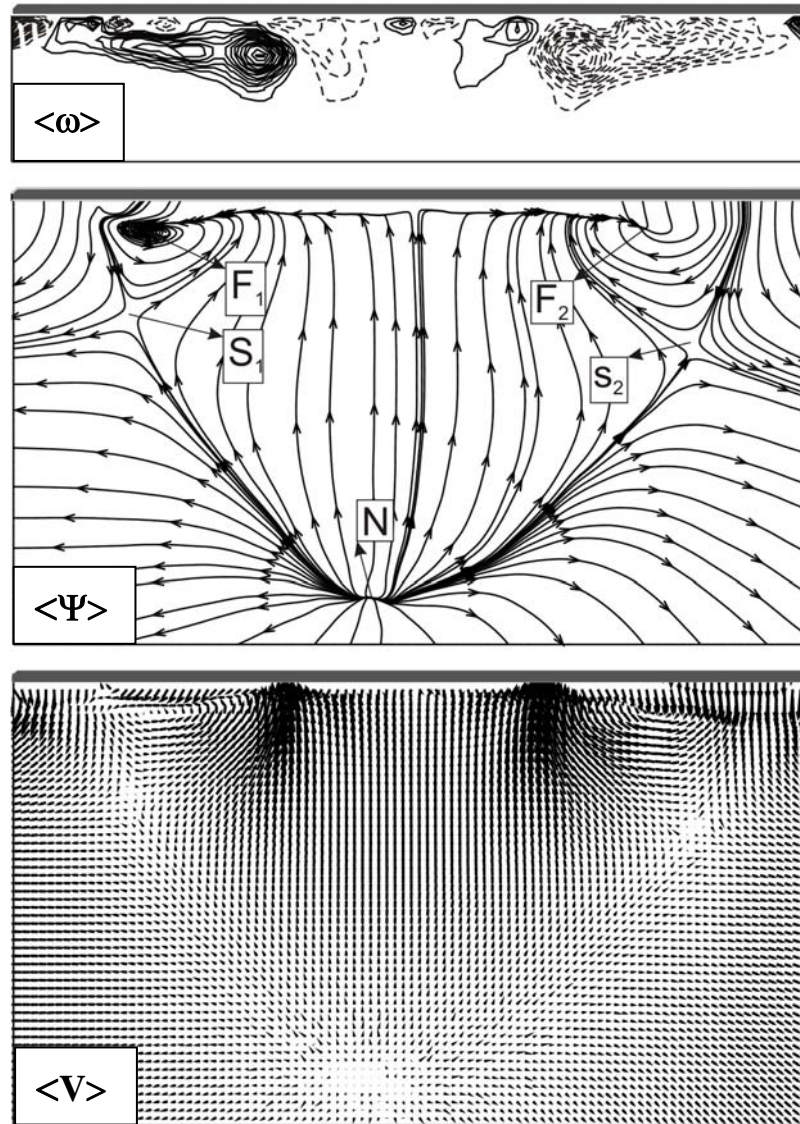


Figure 4.9. Patterns of time-averaged vorticity, $\langle \omega \rangle$, streamline, $\langle \Psi \rangle$, and distribution of velocity vectors, $\langle V \rangle$, for angle of attack $\alpha=7^\circ$, $\theta=0^\circ$. Laser sheet is located at $x/C = 0.8$. For contours of time-averaged vorticity, minimum and incremental values are $[\langle \omega \rangle]_{\min} = 0.3 \text{ s}^{-1}$ and $\Delta[\langle \omega \rangle] = 0.3 \text{ s}^{-1}$.

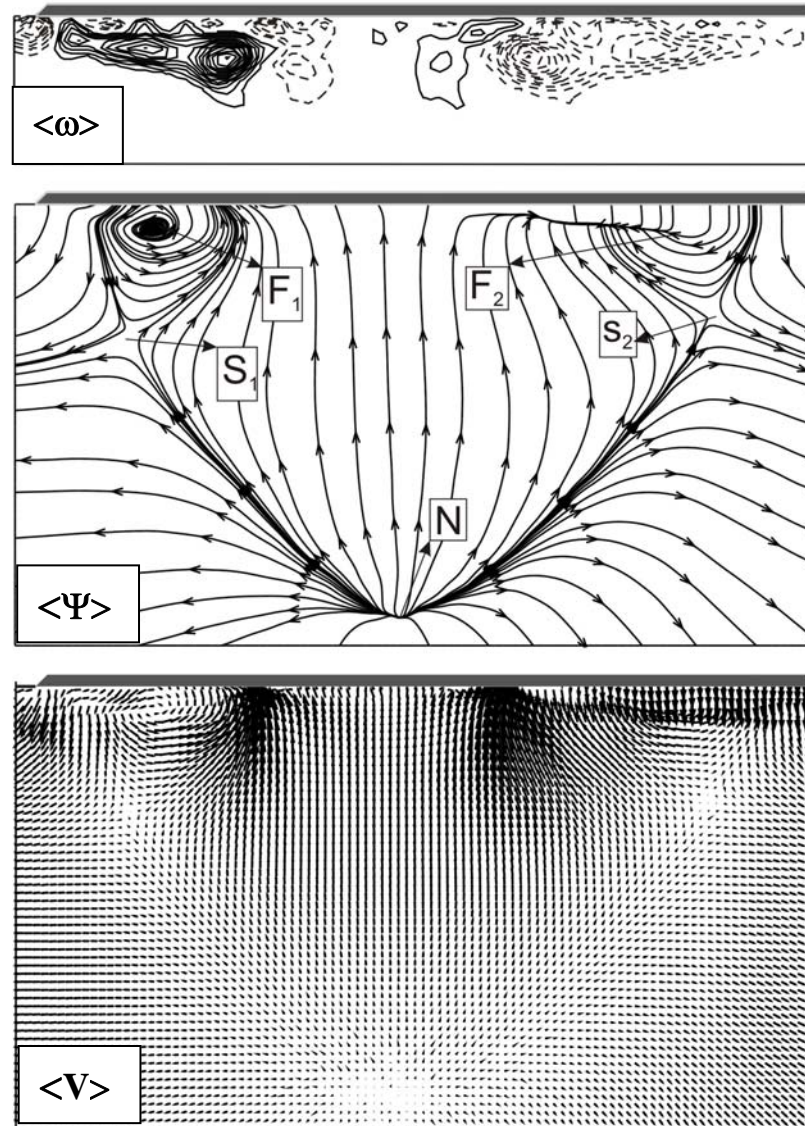


Figure 4.10. Patterns of time-averaged vorticity, $\langle \omega \rangle$, streamline, $\langle \Psi \rangle$, and distribution of velocity vectors, $\langle V \rangle$, for angle of attack $\alpha=7^\circ$, $\theta=6^\circ$. Laser sheet is located at $x/C = 0.8$. For contours of time-averaged vorticity, minimum and incremental values are $[\langle \omega \rangle]_{\min} = 0.3 \text{ s}^{-1}$ and $\Delta[\langle \omega \rangle] = 0.3 \text{ s}^{-1}$.

The patterns of time-averaged vorticity, $\langle \omega \rangle$, streamline, $\langle \Psi \rangle$, and velocity vectors distributions, $\langle V \rangle$, in end-view measuring cross-section at $X/C=0.8$ are presented in Figure 4.11 for angle of attack $\alpha=7^\circ$ and yaw angle $\theta=8^\circ$. Examination of this images in this figure reveals that location of foci, F_1 and F_2 , saddle points, S_1 and S_2 , nodal point N and lines of divergence did not alter when the yaw angle is moved from $\theta=6^\circ$ and $\theta=8^\circ$. The central points of main vortices move to the left-

hand-side of the wing as yaw angle is increased from $\theta=0^\circ$ to $\theta=8^\circ$. Actually, saddle points S_1 and S_2 , noddle points, N, occur on the boundary which is indicated by lines of divergence. This boundary identifies the border between weak flow region and free-stream flow region. It is know that flow structure is very sensitive to angle of attack, α . As the value of attack angle, α , increases from $\alpha=7^\circ$ to 10° topological characteristics of the vortical flow is clearly identifiable as seen in Figure 4.12. The time-averaged patterns of vorticity, $\langle\omega\rangle$, have an elongated shape and move slightly downward from the surface of the delta wing comparing to the case of $\alpha=7^\circ$. A well defined foci, F_1 and F_2 , are presented by patterns of streamlines, $\langle\Psi\rangle$. Yanıktepe and Rockwell (2004) indicated that location of an extremum of vorticity is not coincident with the locus of the streamline patterns. In addition, the spatial extent of the large-scale pattern of streamlines is substantially larger than the thickness of the elongated vorticity layer. In the present experiment, similar result has been obtained. Below foci, F_1 and F_2 , two saddle points, S_1 and S_2 , on the bifurcation lines take place. At the bottom of the image, a nodal point, N, is exist at the central axis of the cross-flow plane. Patterns of velocity vectors clearly indicate the locations of swirling which is coincident with the foci of the streamline patterns.

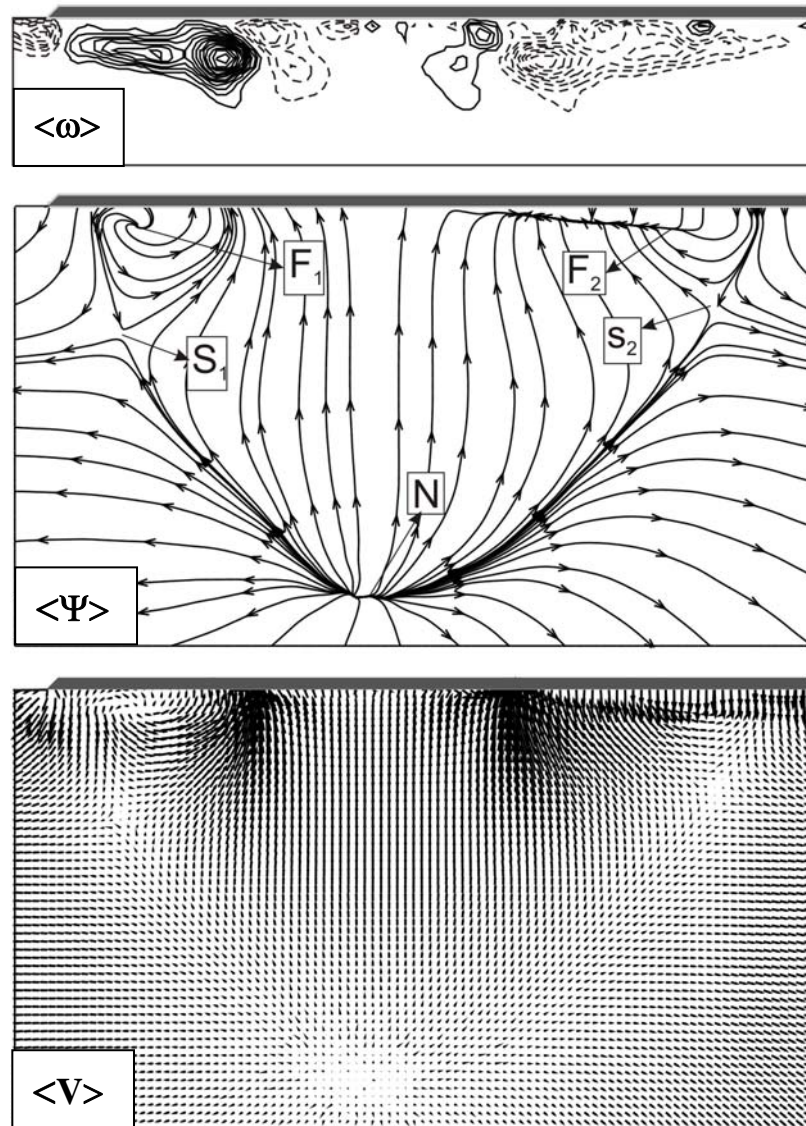


Figure 4.11. Patterns of time-averaged vorticity, $\langle \omega \rangle$, streamline, $\langle \Psi \rangle$, and distribution of velocity vectors, $\langle V \rangle$, for angle of attack $\alpha=7^\circ$, $\theta=8^\circ$. Laser sheet is located at $x/C = 0.8$. For contours of time-averaged vorticity, minimum and incremental values are $[\langle \omega \rangle]_{\min} = 0.3 \text{ s}^{-1}$ and $\Delta[\langle \omega \rangle] = 0.3 \text{ s}^{-1}$.

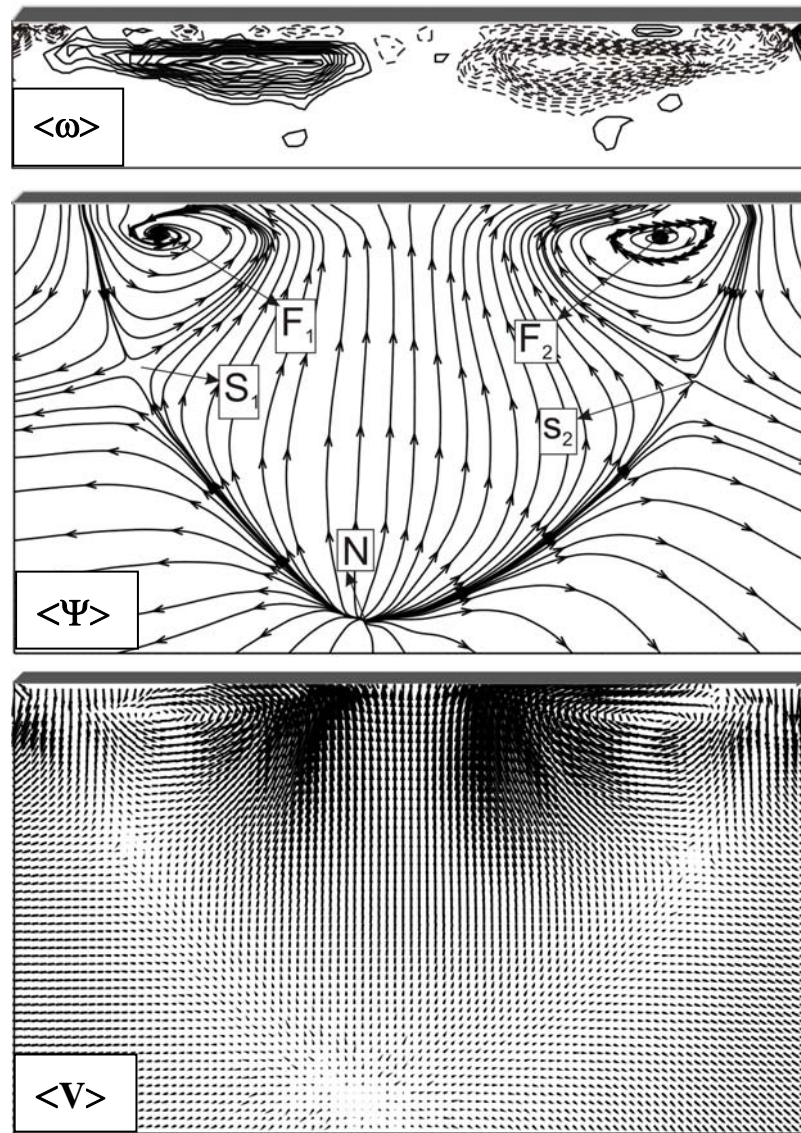


Figure 4.12. Patterns of time-averaged vorticity, $\langle \omega \rangle$, streamline, $\langle \Psi \rangle$, and distribution of velocity vectors, $\langle V \rangle$, for angle of attack $\alpha=10^\circ$, $\theta=0^\circ$. Laser sheet is located at $x/C = 0.8$. For contours of time-averaged vorticity, minimum and incremental values are $[\langle \omega \rangle]_{\min} = 0.3 \text{ s}^{-1}$ and $\Delta[\langle \omega \rangle] = 0.3 \text{ s}^{-1}$.

Figure 4.13 presents flow topology of the delta wing at a chordwise location $X/C=0.8$ in crossflow plane for $\alpha=10^\circ$ and $\theta=6^\circ$. Under this yaw angle, dye visualization indicates that the symmetrical vortical flow structure is developed on both side of the chord axis of the delta wing. PIV results in crossflow plane i.e. end-view plane also reveals that the domain of positive and negative vorticity shown in first image is not similar anymore. For example, negative vorticity extrema is enlarged compared with positive vorticity extrema under distortion of the delta wing position against free stream flow direction with yaw angle, $\theta=6^\circ$. Both vorticity extremas move to the left hand side in cross flow plane. Streamline patterns do not define foci F_1 and F_2 symmetrically. Saddle points, S_1 and S_2 , bifurcation line and nodal point, N , appear more or less at the same locations comparing to the case of yaw angle $\theta=0^\circ$. Velocity vectors distributions presented in the last images indicate a single swirl which coincides with the location of focus F_1 . Increasing the yaw angle, θ , from $\theta=6^\circ$ to $\theta=8^\circ$ the flow structure slightly alters as seen in Figure 4.14. Close to the surface of the delta wing a bifurcation line takes place with a half saddle point between foci F_1 and F_2 .

Increasing attack angle to a value of $\alpha=13^\circ$ and having $\theta=0^\circ$ yaw angle, a well defined positive and negative pair of vorticity cluster occur adjacent to the surface of the delta wing. Vortices are elongated and occupy nearly whole neighboring region of the region of the delta wing. Well defined foci, F_1 and F_2 , presented by patterns of streamline do not coincide with the central points of vorticity extrema, but they coincide with the central part of reversed flows indicated by distributions of velocity vectors. When the delta wing is yawed by 6 degree under the same attack angle ($\alpha=13^\circ$) the topology of the flow indicates that vortical flow structure is symmetric in the crossflow plane as seen in Figure 4.16. But, in the case of yaw angle $\theta=8^\circ$ the symmetrical structure of flow is deteriorated.

Setting the angle of attack to a value of $\alpha=17^\circ$ and with zero yaw angle. The central points of foci F_1 and F_2 move to each other comparing to the case of $\alpha=7^\circ$ and $\theta=0^\circ$. It is worth to mention that the location of an extremum of vorticity is coincident with foci of the streamline patterns and reversed flow presented by

velocity vectors distribution shown in Figure 4.19. Here, angle of attack is taken as $\alpha=17^\circ$ and $\theta=6^\circ$. In Figure 4.19, a well defined vorticity remains when the yaw angle is increased to a value of $\theta=8^\circ$. Maximum velocity values usually appear in the region of maximum vorticity.

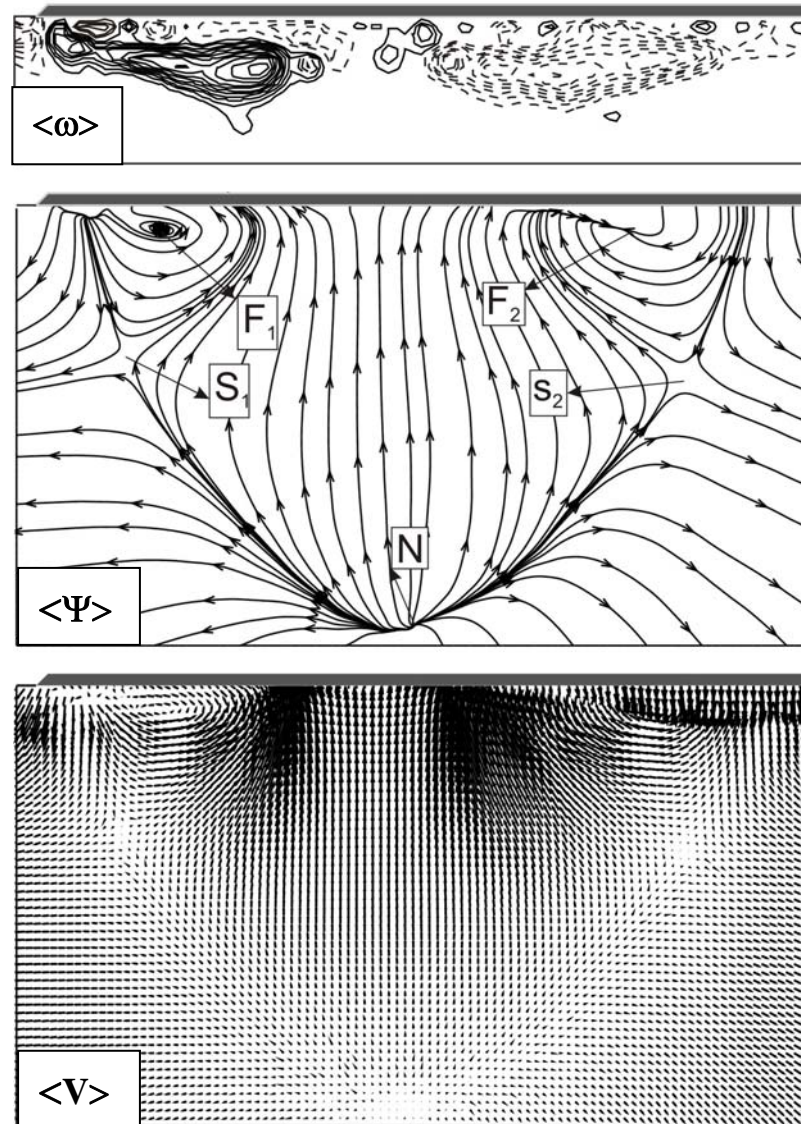


Figure 4.13. Patterns of time-averaged vorticity, $\langle \omega \rangle$, streamline, $\langle \Psi \rangle$, and distribution of velocity vectors, $\langle V \rangle$, for angle of attack $\alpha=10^\circ$, $\theta=6^\circ$. Laser sheet is located at $x/C = 0.8$. For contours of time-averaged vorticity, minimum and incremental values are $[\langle \omega \rangle]_{\min} = 0.3 \text{ s}^{-1}$ and $\Delta[\langle \omega \rangle] = 0.3 \text{ s}^{-1}$.

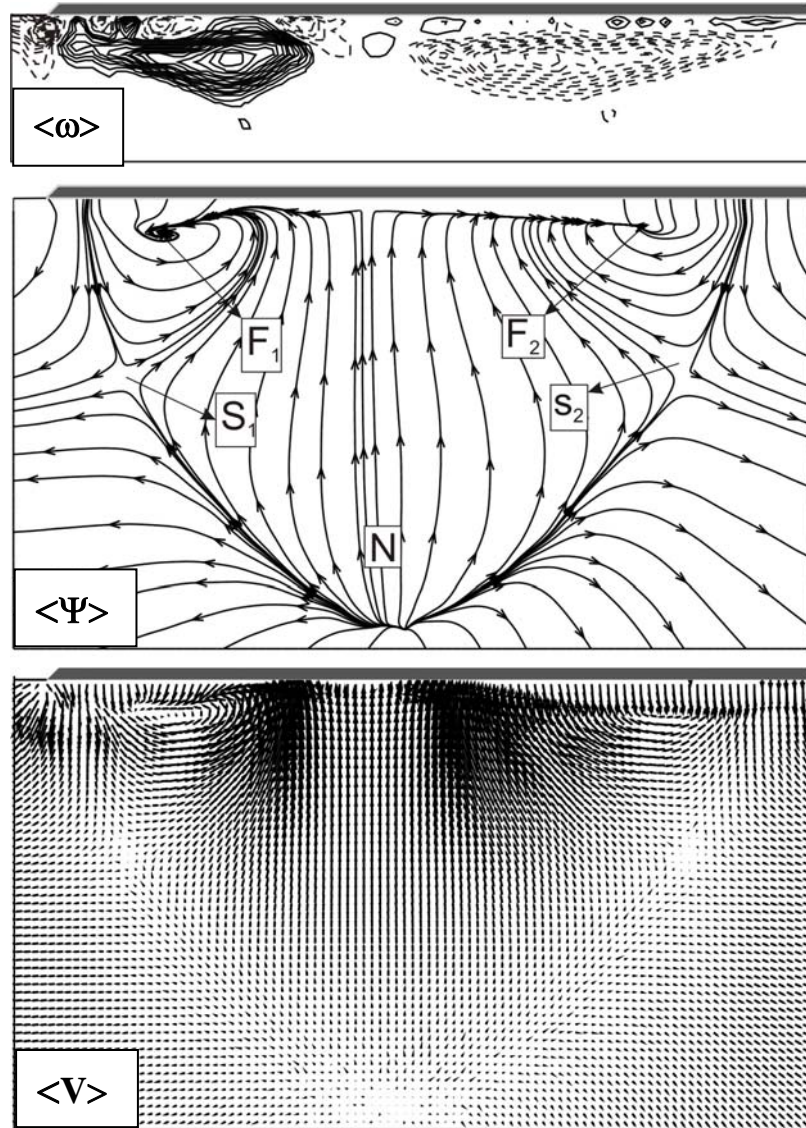


Figure 4.14. Patterns of time-averaged vorticity, $\langle \omega \rangle$, streamline, $\langle \Psi \rangle$, and distribution of velocity vectors, $\langle V \rangle$, for angle of attack $\alpha=10^\circ$, $\theta=8^\circ$. Laser sheet is located at $x/C = 0.8$. For contours of time-averaged vorticity, minimum and incremental values are $[\langle \omega \rangle]_{\min}=0.3 \text{ s}^{-1}$ and $\Delta[\langle \omega \rangle]=0.3 \text{ s}^{-1}$.

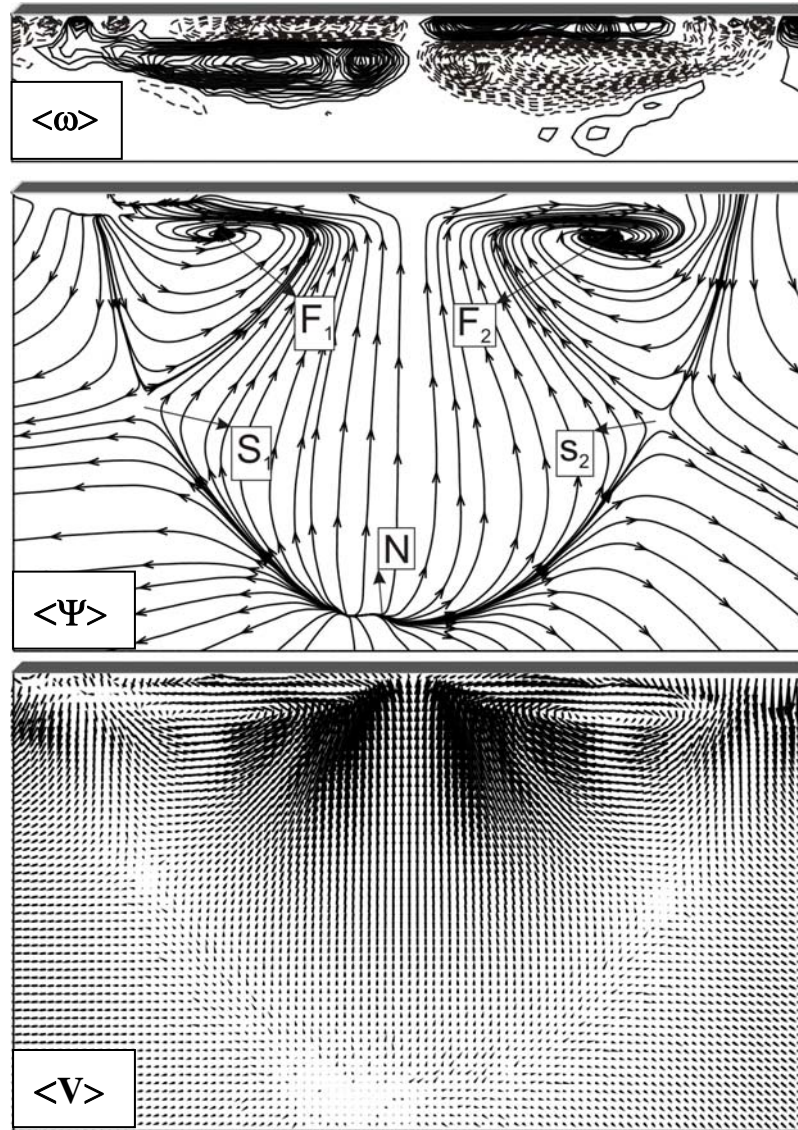


Figure 4.15. Patterns of time-averaged vorticity, $\langle \omega \rangle$, streamline, $\langle \Psi \rangle$, and distribution of velocity vectors, $\langle V \rangle$, for angle of attack $\alpha=13^\circ$, $\theta=0^\circ$. Laser sheet is located at $x/C = 0.8$. For contours of time-averaged vorticity, minimum and incremental values are $[\langle \omega \rangle]_{\min} = 0.3 \text{ s}^{-1}$ and $\Delta[\langle \omega \rangle] = 0.3 \text{ s}^{-1}$.

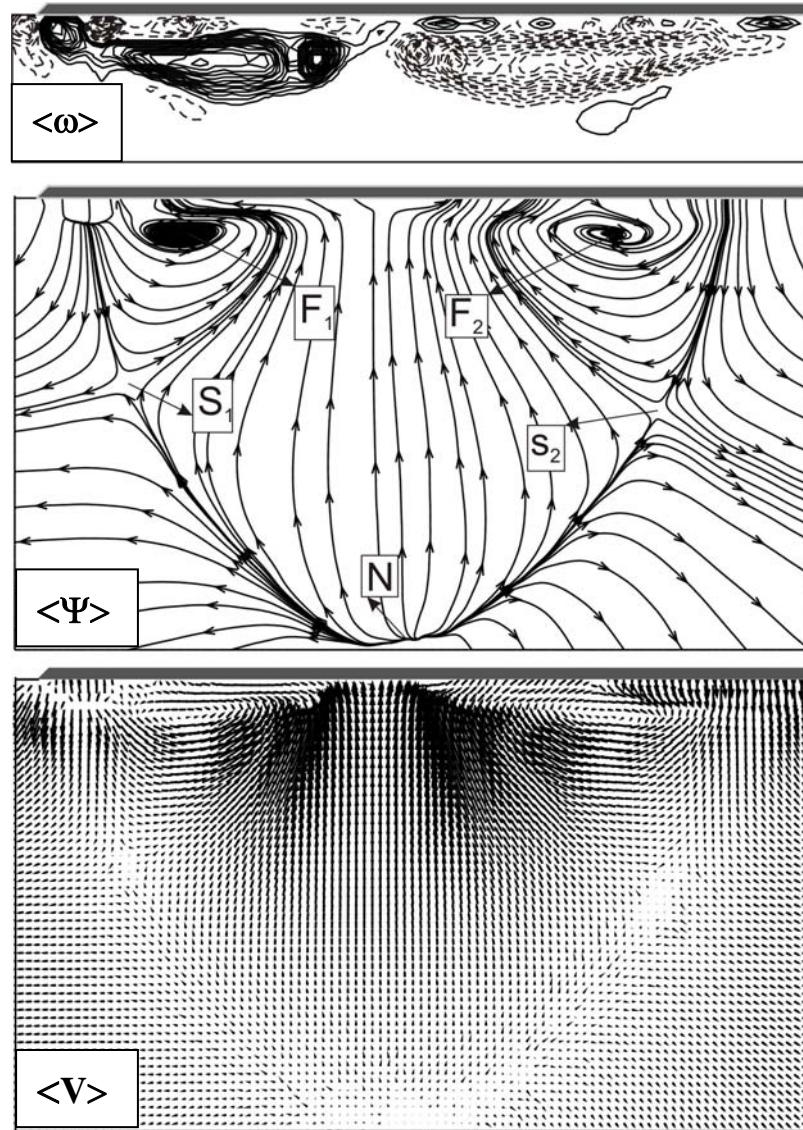


Figure 4.16. Patterns of time-averaged vorticity, $\langle \omega \rangle$, streamline, $\langle \Psi \rangle$, and distribution of velocity vectors, $\langle V \rangle$, for angle of attack $\alpha=13^\circ$, $\theta=6^\circ$. Laser sheet is located at $x/C = 0.8$. For contours of time-averaged vorticity, minimum and incremental values are $[\langle \omega \rangle]_{\min} = 0.3 \text{ s}^{-1}$ and $\Delta[\langle \omega \rangle] = 0.3 \text{ s}^{-1}$.

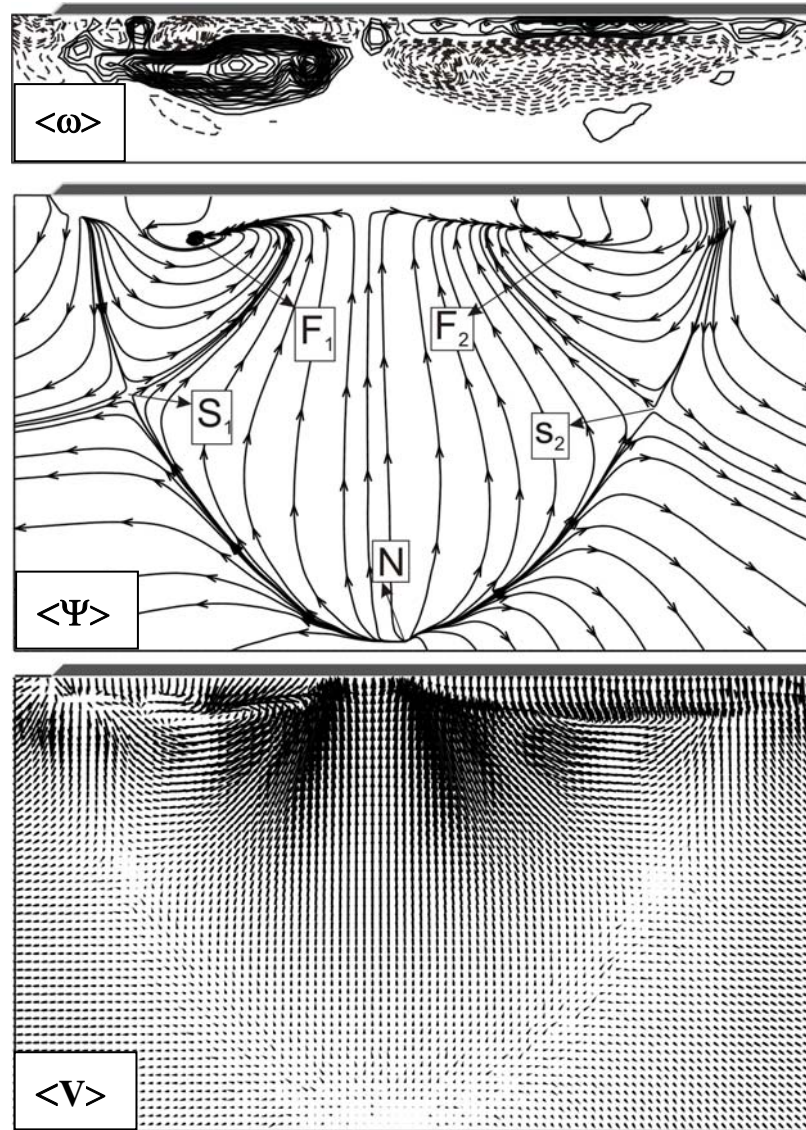


Figure 4.17. Patterns of time-averaged vorticity, $\langle \omega \rangle$, streamline, $\langle \Psi \rangle$, and distribution of velocity vectors, $\langle V \rangle$, for angle of attack $\alpha=13^\circ$, $\theta=8^\circ$. Laser sheet is located at $x/C = 0.8$. For contours of time-averaged vorticity, minimum and incremental values are $[\langle \omega \rangle]_{\min} = 0.3 \text{ s}^{-1}$ and $\Delta[\langle \omega \rangle] = 0.3 \text{ s}^{-1}$.

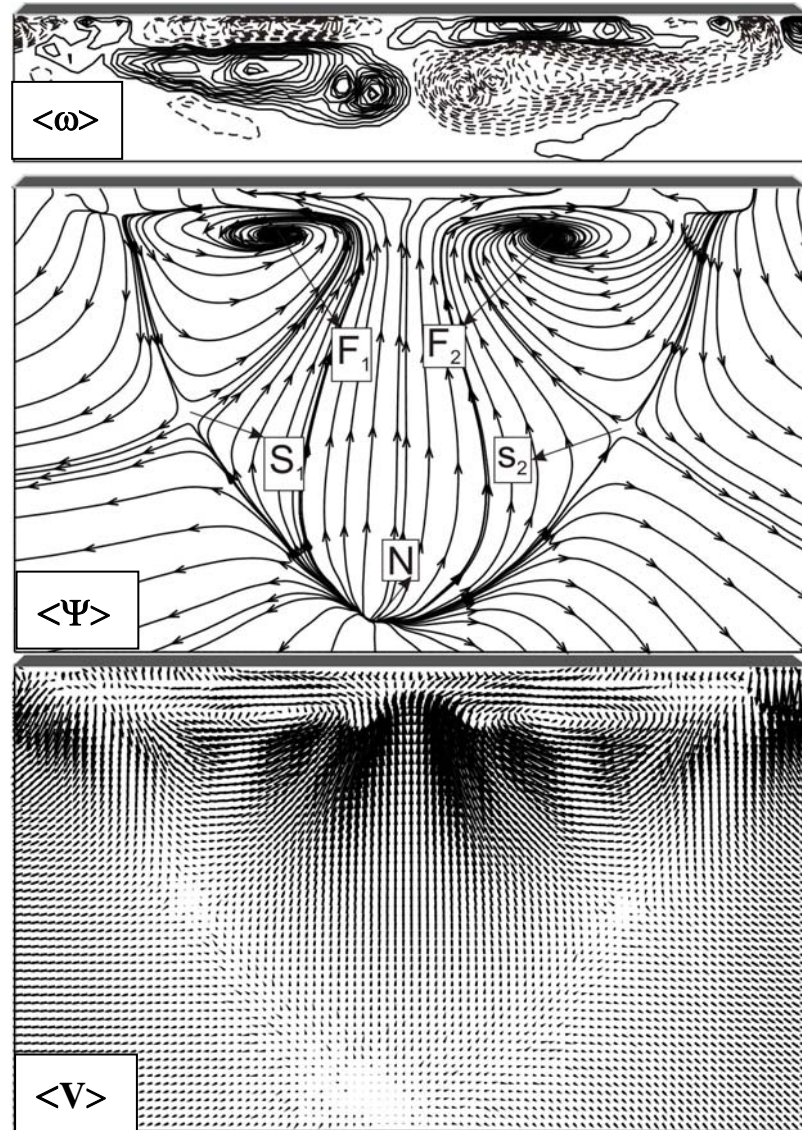


Figure 4.18. Patterns of time-averaged vorticity, $\langle \omega \rangle$, streamline, $\langle \Psi \rangle$, and distribution of velocity vectors, $\langle V \rangle$, for angle of attack $\alpha=17^\circ$, $\theta=0^\circ$. Laser sheet is located at $x/C = 0.8$. For contours of time-averaged vorticity, minimum and incremental values are $[\langle \omega \rangle]_{\min} = 0.3 \text{ s}^{-1}$ and $\Delta[\langle \omega \rangle] = 0.3 \text{ s}^{-1}$.

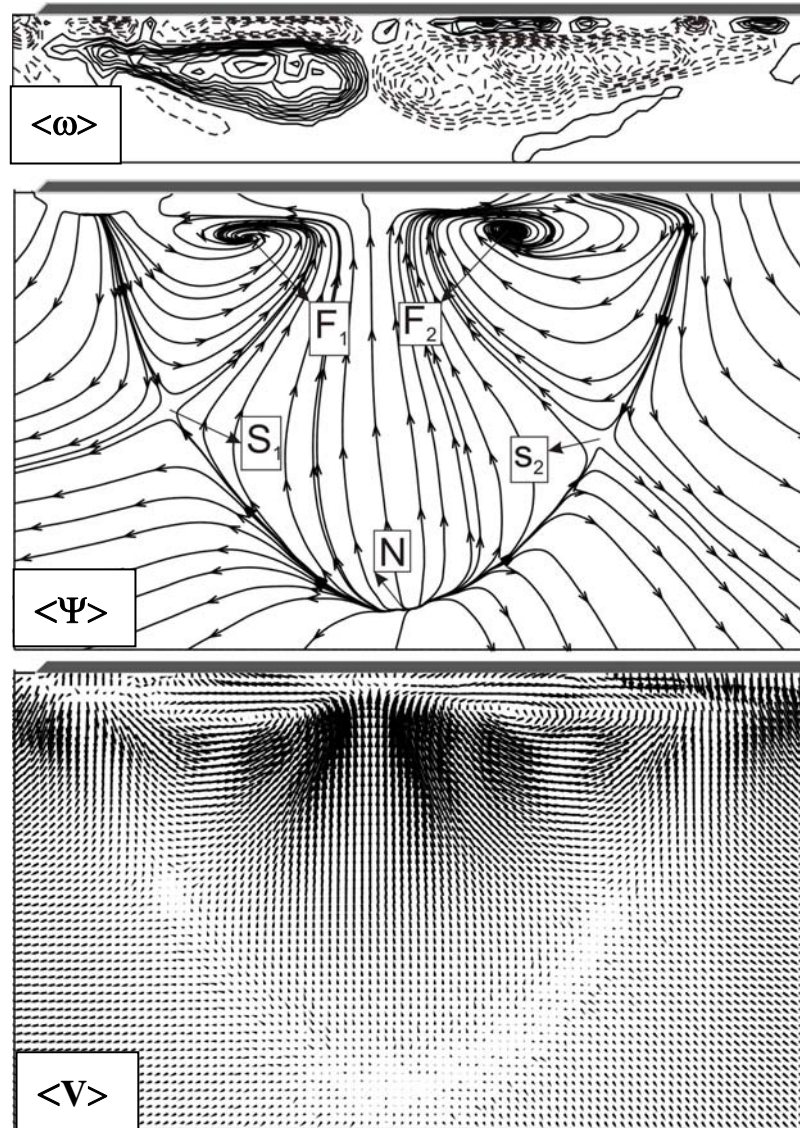


Figure 4.19. Patterns of time-averaged vorticity, $\langle \omega \rangle$, streamline, $\langle \Psi \rangle$, and distribution of velocity vectors, $\langle V \rangle$, for angle of attack $\alpha=17^\circ$, $\theta=6^\circ$. Laser sheet is located at $x/C = 0.8$. For contours of time-averaged vorticity, minimum and incremental values are $[\langle \omega \rangle]_{\min}=0.3 \text{ s}^{-1}$ and $\Delta[\langle \omega \rangle]=0.3 \text{ s}^{-1}$.

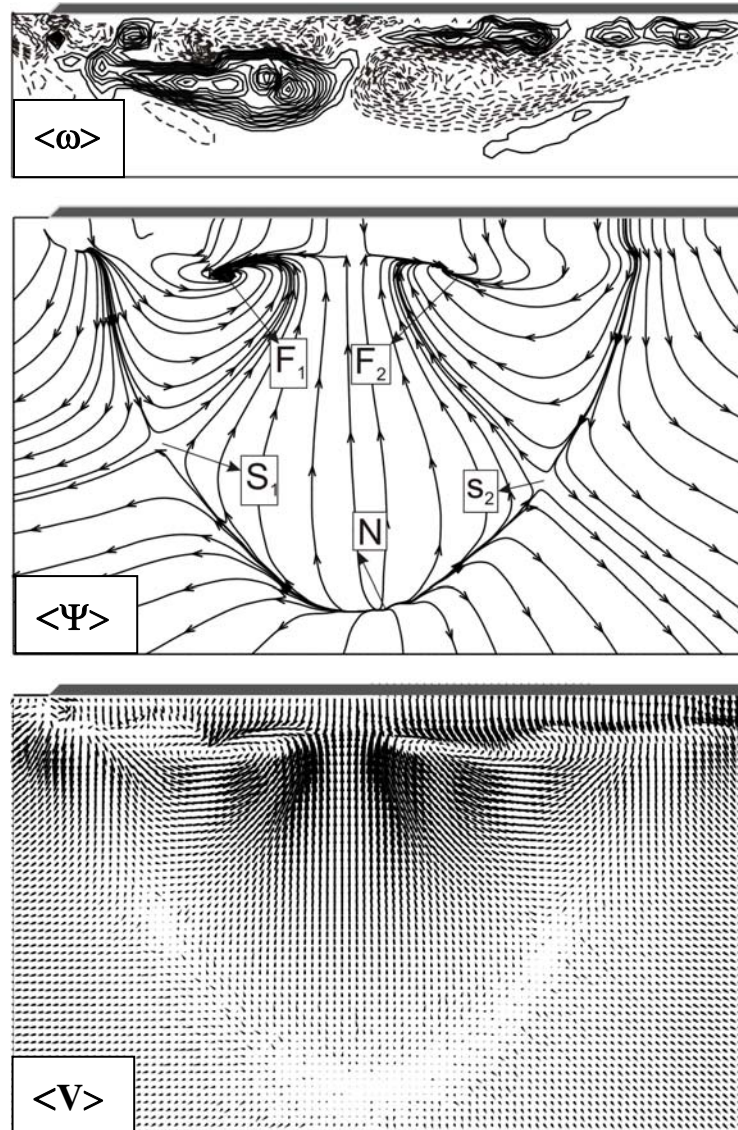


Figure 4.20. Patterns of time-averaged vorticity, $\langle \omega \rangle$, streamline, $\langle \Psi \rangle$, and distribution of velocity vectors, $\langle V \rangle$, for angle of attack $\alpha=17^\circ$, $\theta=8^\circ$. Laser sheet is located at $x/C = 0.8$. For contours of time-averaged vorticity, minimum and incremental values are $[\langle \omega \rangle]_{\min} = 0.3 \text{ s}^{-1}$ and $\Delta[\langle \omega \rangle] = 0.3 \text{ s}^{-1}$.

Flow structure on the right-hand-side of the delta wing in end-view planes shown in Figures 4.9-20 is under effect of yaw angle. Generally, the elongated layer widens when yaw angle increases on the right-hand-side of time-averaged vorticity contours. If the patterns of the time-averaged vorticity are observed in detail, there are two vorticity extrema which can be called as main (high) and slave (low). While the time-averaged vector fields are viewed, there is an identifiable interface exists

between a region of high velocity flow below the wing. The corresponding streamline topology, which is constructed from these time-averaged velocity fields, indicates two saddle points and foci which are designated as S_1 , S_2 , F_1 , F_2 , respectively. Saddle points are appeared well below the foci. The streamline patterns inside the major streamlines that connect to the saddle points exhibit a well defined swirl pattern. Centers of the foci do not coincide with the maxima of time-averaged vortices. Saddle points take a place further down in vertical direction and get closer to each other while angle of attack is increased. Center of foci get closer to each other as the angle of attack is increased. In addition, there is a pair of vortices between main vortices and the delta wing surface, if the time-averaged vortex contours are observed. These vortices can be seen clearly especially at high angle of attacks. This pair of vortices rotates in opposite direction of the main vortex. When the delta wing is kept stationary at attack angle $\alpha=7^\circ$ and yaw angle $\theta=6^\circ$ elongated positive and negative vorticity are developed below the delta wing close to the surface of the delta wing. Due to the effect of yaw angle, $\theta=6^\circ$, focus F_1 is more identifiable than F_2 . At the bottom of foci saddle points S_1 and S_2 exist at the same positions. A line of divergence or bifurcation emanate from the noddle point N cross these saddle points. On the other side of saddle points, lines of bifurcation move downward close to saddle points S_1 and S_2 . Patterns of velocity vectors also indicate that vortical flow structure takes place in the region where primary vortices take place. Lines of bifurcation and location of noddle points, N, are clearly seen.

4.1.2.2. Patterns of Time-Averaged Vorticity, Streamline and Velocity Vectors Topology (Plan-View)

Patterns of the time-averaged vorticity, $\langle\omega\rangle$, streamline, $\langle\Psi\rangle$, and velocity, $\langle V\rangle$ topology for angles of attack $\alpha=7^\circ$, 10° , 13° and 17° for the cases of $\theta=0^\circ$, 6° , 8° and 15° are shown in Figures 4.21-36. The laser sheet which defines the measurement plane is 0.5 mm below the delta wing surface. This means that, these results show the near-surface flow topology or flow structure over the delta wing. The experiments were conducted at the same attack and yaw angles as taken for the end-view experiments to be able to understand the flow structure on delta wing fully. Here, $\theta=15^\circ$ yaw angle was taken additionally. The first images show the patterns of time-averaged vorticity, $\langle\omega\rangle$, for each attack and yaw angles. To be able to make direct comparison, for the contours of time-averaged vorticity, $\langle\omega\rangle$, minimum and incremental values was taken same values as $[\langle\omega\rangle]_{\min}=0.4 \text{ s}^{-1}$ and $\Delta[\langle\omega\rangle]=1 \text{ s}^{-1}$, respectively. The contours of solid and dashed lines show the positive and negative contours, respectively. At first view, there is a pair of spiral vortices which emanate from the leading edge of the delta wing and two well-defined clusters of negative and positive time-averaged vorticity, $\langle\omega\rangle$, $[L_E, L_R]$, occur along the leading edges of the delta wing. They occur due to the three dimensional instability of the shear layer separating from the windward surface of the delta wing. These vortices have an elongated form which can be understood from corresponding dye visualization experiments. A symmetrical flow topology dominates whole wing surface in the case of zero yaw angle. Also, there is a pair of vortices which are located at the middle region of the wing surface. These counter-rotating vortices are adjacent to the main leading vortices, M. These middle vortices can be seen clearly at attack angles $\alpha=7^\circ$ and 10° . As the angle of attack is increased they begin to disappear. They are rarely seen at attack angle of $\alpha=13^\circ$. In all cases of attack angle of $\alpha=17^\circ$ these vortices can not be seen, anymore. At $\alpha=7^\circ$, there is no apparent swirl in close region of the leading edge of the delta wing. Also, the extrama of the leading edge (main) vortices, M, move downward towards the trailing edge of the delta wing. But these extramas can not move further downstream of the middle region of the delta wing.

The second image of Figure 4.21 shows the patterns of the time-averaged streamlines, $\langle\Psi\rangle$. There is a symmetrical flow structure in the case of zero yaw angle. In all cases of attack angle $\alpha=7^\circ$, there is no apparent swirl in close region of the leading edge of the delta wing which is mentioned earlier. But, a pair of focus begins to be appear from attack angle $\alpha=10^\circ$ which are designated as F_1 and F_2 , the centers of foci, F_1 and F_2 , get closer to each other as the angle of attack, α , is increased. The inner line of each vortex, L_i , which shows the large amplitude velocity region on the wing surface, gets closer to each other because of the approximation of the foci, F_1 and F_2 , with vortices.

Figure 4.21 shows the time-averaged patterns of time-averaged vorticity, $\langle\omega\rangle$, streamline, $\langle\Psi\rangle$, and velocity vector distributions, $\langle V\rangle$, having the angle of attack as $\alpha=7^\circ$ and yaw angle $\theta=0^\circ$. In the first image, patterns of time-averaged vorticity, $\langle\omega\rangle$, occupied whole surface of the delta wing. Along the leading edges, elongated vortices, L_E and L_R , occur with relatively high intensity. Just downstream of the apex, well defined positive and negative vortices, $\langle\omega\rangle$, $[M]$, take place. In between these primary pair of vortices, $\langle\omega\rangle$, $[M]$, small size positive and negative vortices occur. In the second image, patterns of streamlines, $\langle\Psi\rangle$, are presented. At $\alpha=7^\circ$ onset of vortex breakdown occurs close to the trailing edge of the delta wing. For this reason, structure is not very complex. Last image presents the distribution of velocity vectors, $\langle V\rangle$, show that the velocity vectors have relatively high magnitude on both side of the mid-chord axis, but along the leading edges on both sides the magnitude of velocity become very small indicating that there are secondary vortices, V_s , which coincide with bifurcation lines. The third image of Figure 4.21 shows the time-averaged velocity, $\langle V\rangle$, field over the delta wing. The symmetrical flow topology can be seen here, in the case of zero yaw angle, too. This image indicates that, the velocity vectors have relatively large amplitude in the central portion of the delta wing. However, farther outboard from the plane of symmetry, the magnitude of velocity becomes relatively small. At all values of attack angle, α , and yaw angle, θ , the magnitude of velocity vectors, $\langle V\rangle$, show an abrupt decrease immediately downstream of the leading edge which is indication of the secondary

vortex. As the value of attack angle, α , increases, the spatial extent of the region of very low velocity increases. Furthermore, a well-defined swirl pattern of velocity is evident in the near region of the apex, except at $\alpha=7^\circ$. This swirl pattern gets larger, as α is increased. In the central portion of each of these swirl patterns, the magnitude of, $\langle V \rangle$, is very small. When attack angle is increased, the region of low velocity also emanates the whole surface of the wing. At attack angle $\alpha=17^\circ$, the low velocity region dominates the whole surface of the delta wing.

While yaw angle is applied to the delta wing, the symmetry of the flow topology is deteriorated. Generally, the streamline pattern, $\langle \Psi \rangle$, tends to be linear through its lengthwise direction at the opposite side of yawed side of the delta wing. Because of this reason, focus, F, located at this side begins to disappear. However, diameter of the focus located at yawed side is increased as the yaw angle is increased. This situation causes the large low velocity region at yawed side of the delta wing, but it is not the case for the other side. At angle of attack $\alpha=17^\circ$, the separated flow region dominates the whole wing surface. So that, yawing effect, mentioned before, does not cause any difference in size between the two separated flow regions for the yaw angle range $0^\circ \leq \theta \leq 6^\circ$.

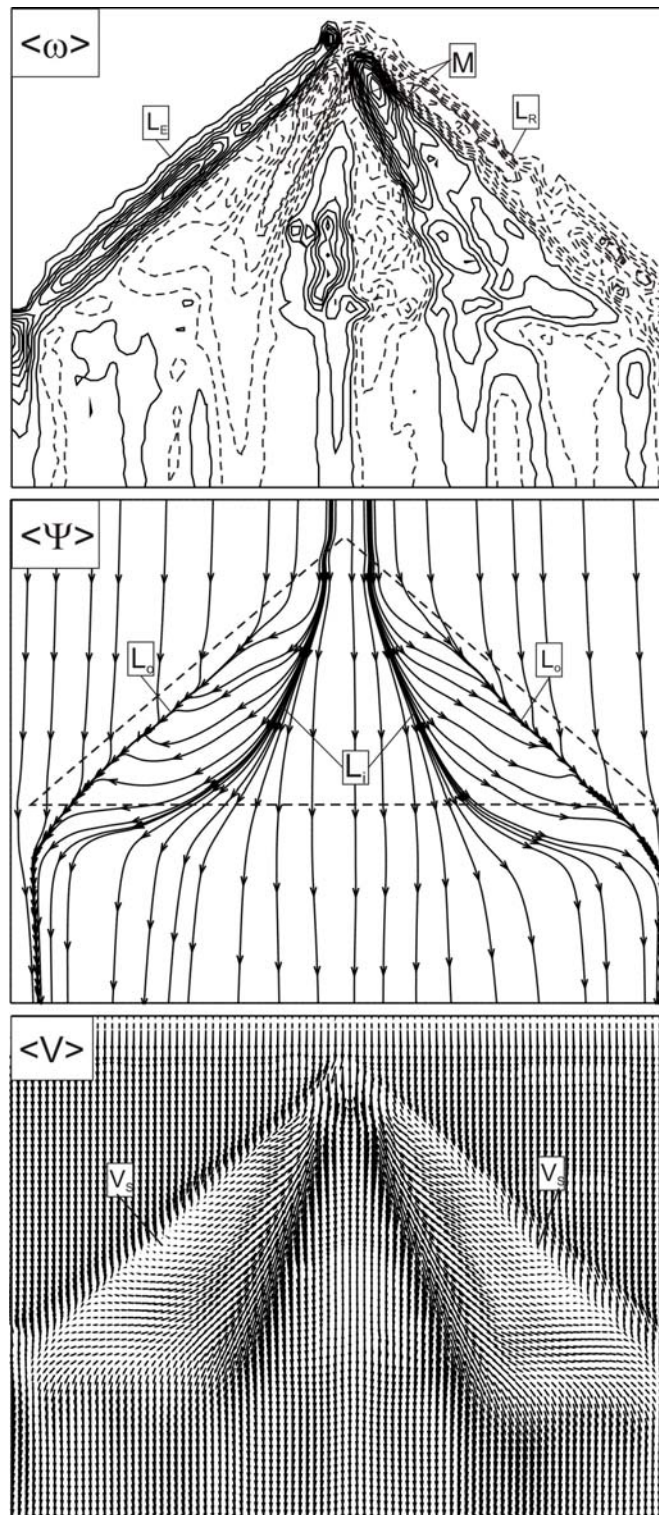


Figure 4.21. Patterns of time-averaged vorticity, $\langle \omega \rangle$, streamline, $\langle \Psi \rangle$, and distribution of velocity vectors, $\langle V \rangle$, for angle of attack $\alpha=7^\circ$, $\theta=0^\circ$. For contours of time-averaged vorticity, minimum and incremental values are $[\langle \omega \rangle]_{\min} = 0.4 \text{ s}^{-1}$ and $\Delta[\langle \omega \rangle] = 1 \text{ s}^{-1}$.

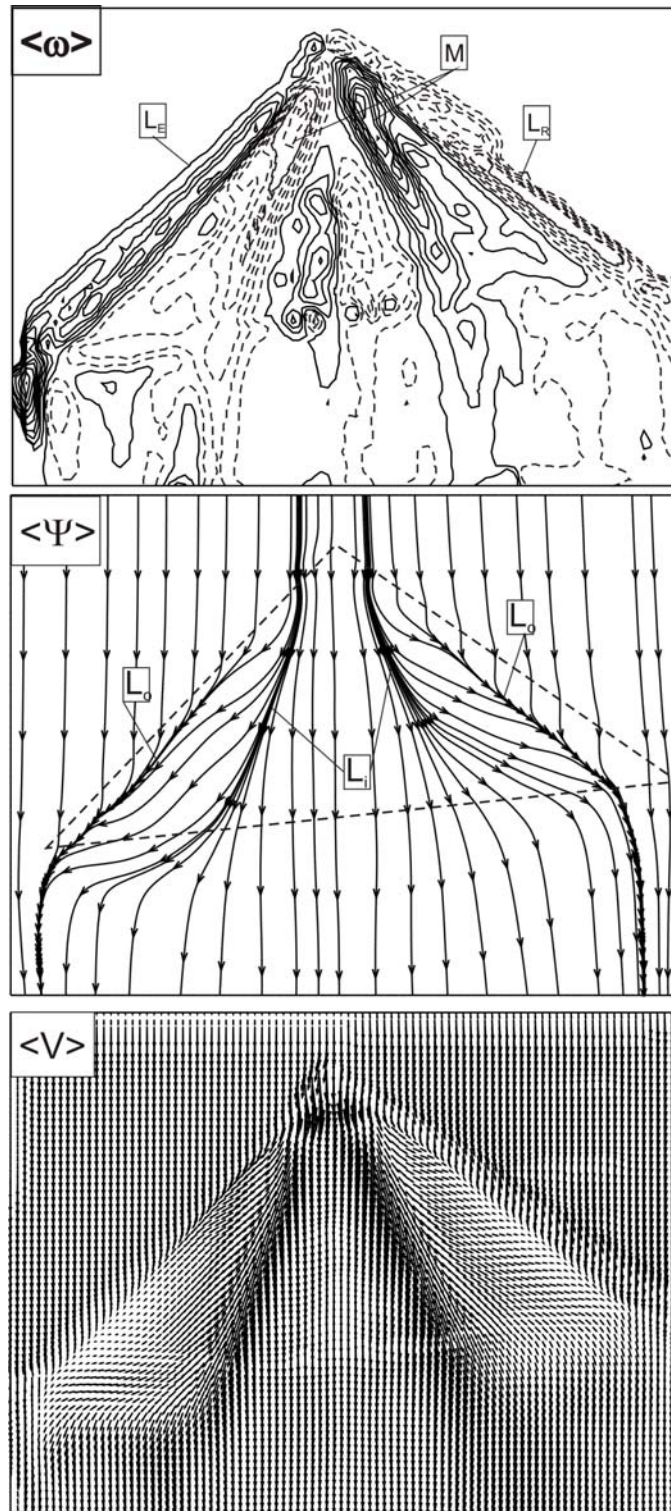


Figure 4.22. Patterns of time-averaged vorticity, $\langle \omega \rangle$, streamline, $\langle \Psi \rangle$, and distribution of velocity vectors, $\langle V \rangle$, for angle of attack $\alpha=7^\circ$, $\theta=6^\circ$. For contours of time-averaged vorticity, minimum and incremental values are $[\langle \omega \rangle]_{\min} = 0.4 \text{ s}^{-1}$ and $\Delta[\langle \omega \rangle] = 1 \text{ s}^{-1}$.

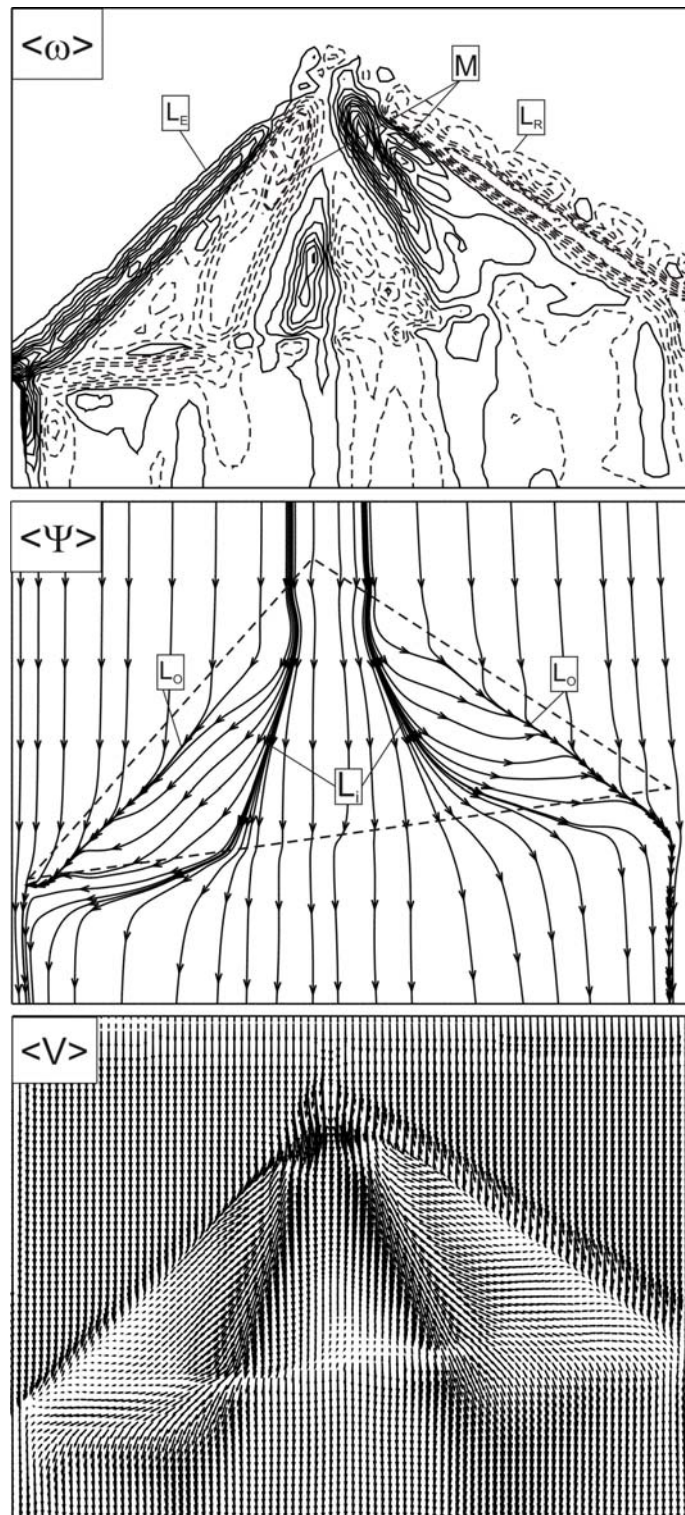


Figure 4.23. Patterns of time-averaged vorticity, $\langle \omega \rangle$, streamline, $\langle \Psi \rangle$, and distribution of velocity vectors, $\langle V \rangle$, for angle of attack $\alpha=7^\circ$, $\theta=8^\circ$. For contours of time-averaged vorticity, minimum and incremental values are $[\langle \omega \rangle]_{\min} = 0.4 \text{ s}^{-1}$ and $\Delta[\langle \omega \rangle] = 1 \text{ s}^{-1}$.

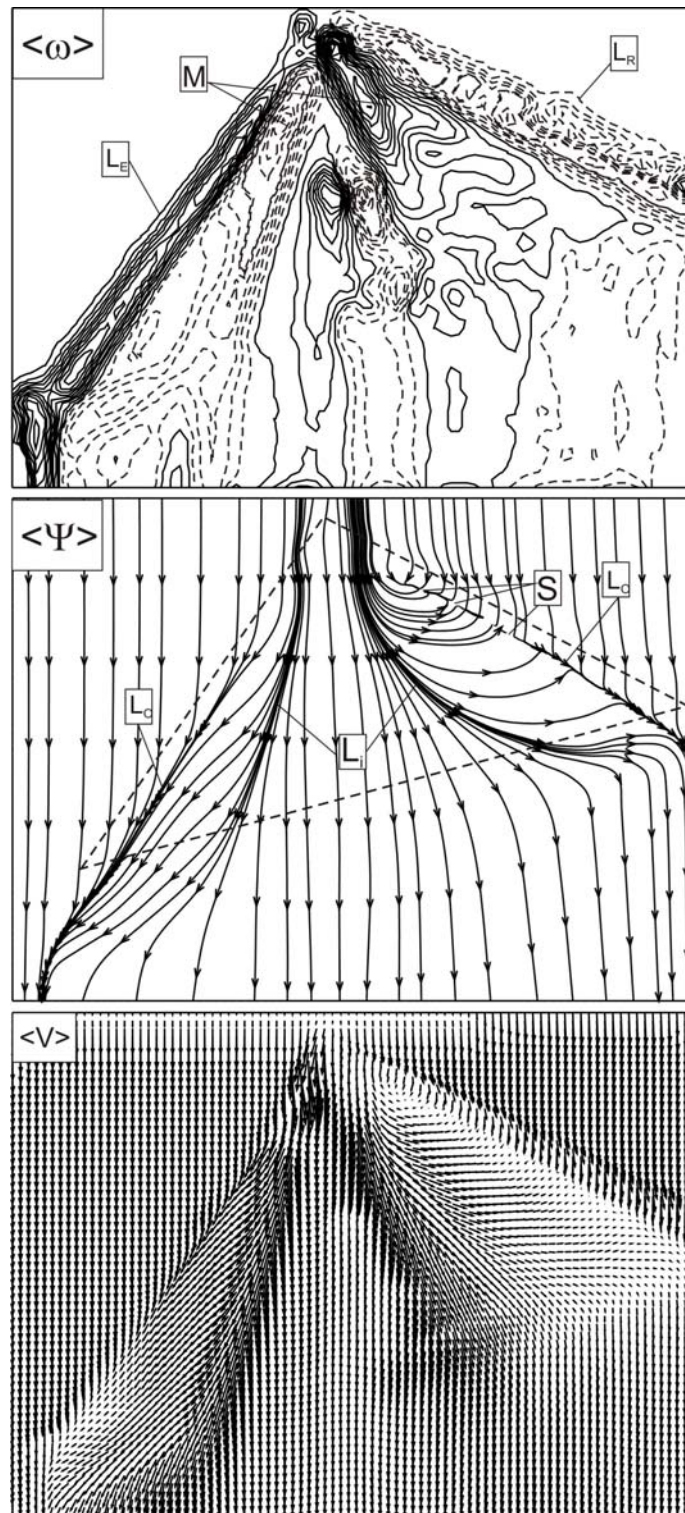


Figure 4.24. Patterns of time-averaged vorticity, $\langle \omega \rangle$, streamline, $\langle \Psi \rangle$, and distribution of velocity vectors, $\langle V \rangle$, for angle of attack $\alpha=7^\circ$, $\theta=15^\circ$. For contours of time-averaged vorticity, minimum and incremental values are $[\langle \omega \rangle]_{\min} = 0.4 \text{ s}^{-1}$ and $\Delta[\langle \omega \rangle] = 1 \text{ s}^{-1}$.

In the case of yaw angle $\theta=6^\circ$ and $\theta=8^\circ$ at $\alpha=7^\circ$, vortical flow structures over the delta wing shown in Figure 4.22 and 4.23 do not change in a large scale. For example, in both yaw angle cases, $\theta=6^\circ$ and $\theta=8^\circ$, leading edge vortices, L_E and L_R , and other vortices appear at the same locations comparing to the case of $\theta=0^\circ$. Patterns of streamline, $\langle\Psi\rangle$, and velocity vectors, $\langle V\rangle$, indicate that the flow structures on both sides of mid-chord axis is not symmetric when yaw angle is bigger than $\theta=6^\circ$. When the yaw angle is set to $\theta=15^\circ$, non-symmetrical flow structure over the delta wing is increased as seen in Figure 4.24.

At the higher angle of attack for example, $\alpha=10^\circ$ shown in Figure 4.25, the flow structure is more complex comparing to the case of $\alpha=7^\circ$, $\theta=0^\circ$ vortex breakdown occurs at mid-point of the central axis of spiral vortices. Patterns of vortices in the first image of Figure 4.25 indicates that primary pair of vortices occur immediately downstream of the tip of the wing. Well defined foci, F_1 and F_2 , which represent the center of reversed flow appear just downstream of the apex of the wing. Along the leading edges, bifurcation lines, L_o , are formed. On these bifurcation lines, L_o , saddle points, S_1 and S_2 , take place. The magnitude of velocity vectors around the line of divergence, L_i , is relatively higher. These saddle points, S_1 and S_2 , occur near the trailing edge of the delta wing. At $\alpha=10^\circ$ and $\theta=0^\circ$ as seen in Figure 4.25, a negative bifurcation line, L_o , extends over a substantial extent of the leading edge. It corresponds to the merging of streamlines towards single line, and represents a line of separation. Saddle points, S_1 and S_2 , are evident in the outboard region of the wing. In addition, a positive bifurcation lines, L_i , are evident. It can be recognized from the diverging motion of streamlines toward single line. They show line of the attachment.

As seen in the case of $\alpha=7^\circ$ and $\theta=0^\circ$, 7° , 10° , 15° , the flow structure adjacent to the surface of the delta wing is more sensitive with yaw angle. At $\alpha=10^\circ$ and $\theta=6^\circ$ a well defined focus, F_1 and F_2 , is formed on the on the yawing side of the wing immediately downstream of the apex of the wing.

At attack angle $\alpha=17^\circ$, these lines, L_i , disappear and a saddle point, S , occurs between foci, F , as seen in Figure 4.33. This saddle point, S , disappears at attack

angle $\alpha=17^\circ$ and yaw angle $\theta=15^\circ$. Because, one of the foci, F_1 and F_2 , disappears due to the yawing effect. There are also other saddle points, designated as S, which are on the apparent intersections of the bifurcation lines. A well defined nodal point, N, is also apparent on the midcord axis close to the trailing edge of the delta wing. A bifurcation line is formed at $\alpha=17^\circ$ for all cases of yaw angle, θ . Relatively weak positive and negative vortices is formed which covers whole surface of the delta wing.

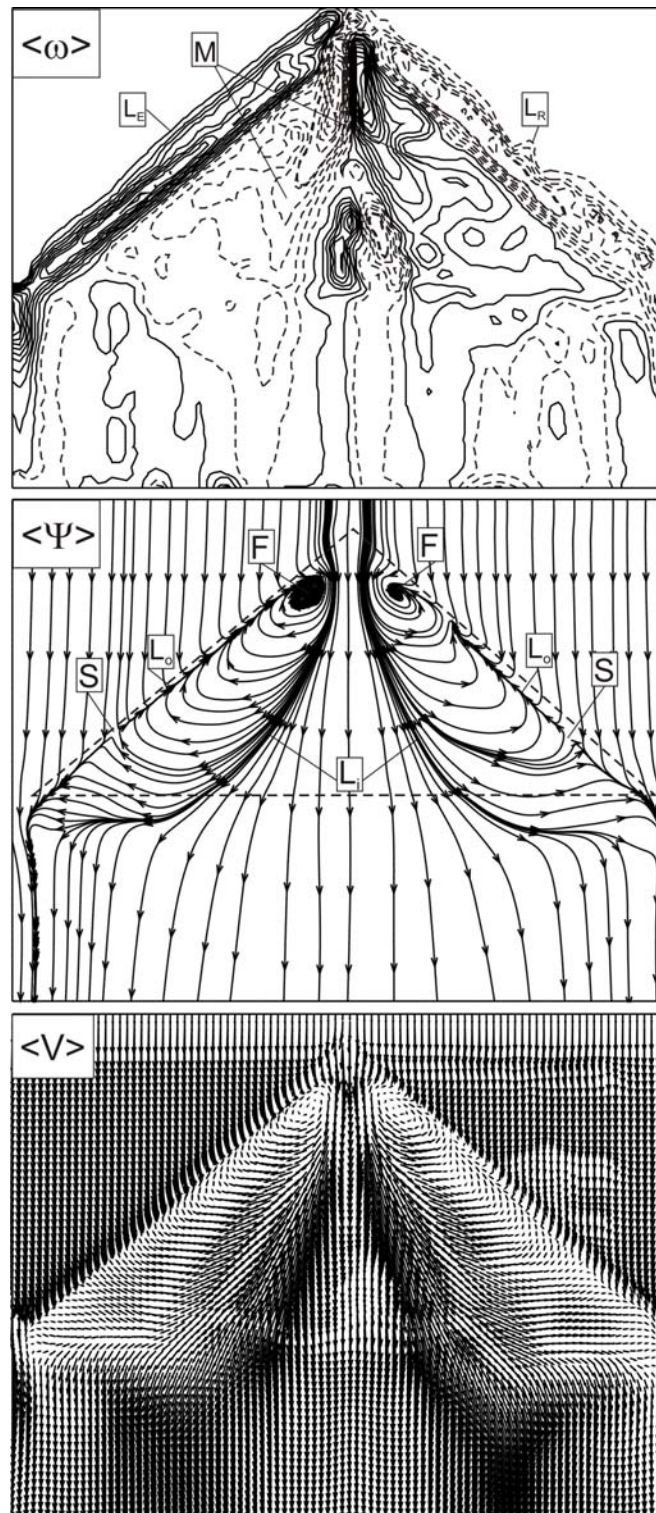


Figure 4.25. Patterns of time-averaged vorticity, $\langle \omega \rangle$, streamline, $\langle \Psi \rangle$, and distribution of velocity vectors, $\langle V \rangle$, for angle of attack $\alpha=10^\circ$, $\theta=0^\circ$. For contours of time-averaged vorticity, minimum and incremental values are $[\langle \omega \rangle]_{\min} = 0.4 \text{ s}^{-1}$ and $\Delta[\langle \omega \rangle] = 1 \text{ s}^{-1}$.

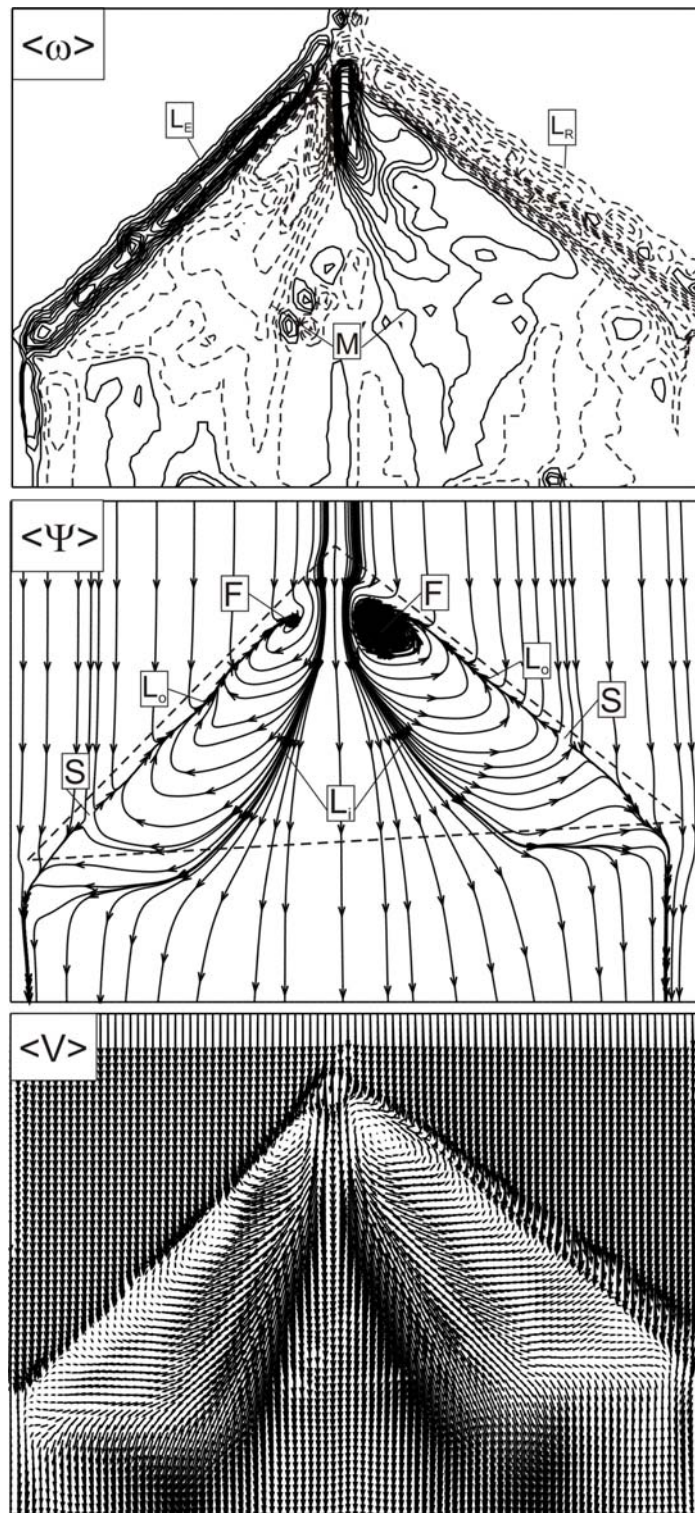


Figure 4.26. Patterns of time-averaged vorticity, $\langle \omega \rangle$, streamline, $\langle \Psi \rangle$, and distribution of velocity vectors, $\langle V \rangle$, for angle of attack $\alpha=10^\circ$, $\theta=6^\circ$. For contours of time-averaged vorticity, minimum and incremental values are $[\langle \omega \rangle]_{\min} = 0.4 \text{ s}^{-1}$ and $\Delta[\langle \omega \rangle] = 1 \text{ s}^{-1}$

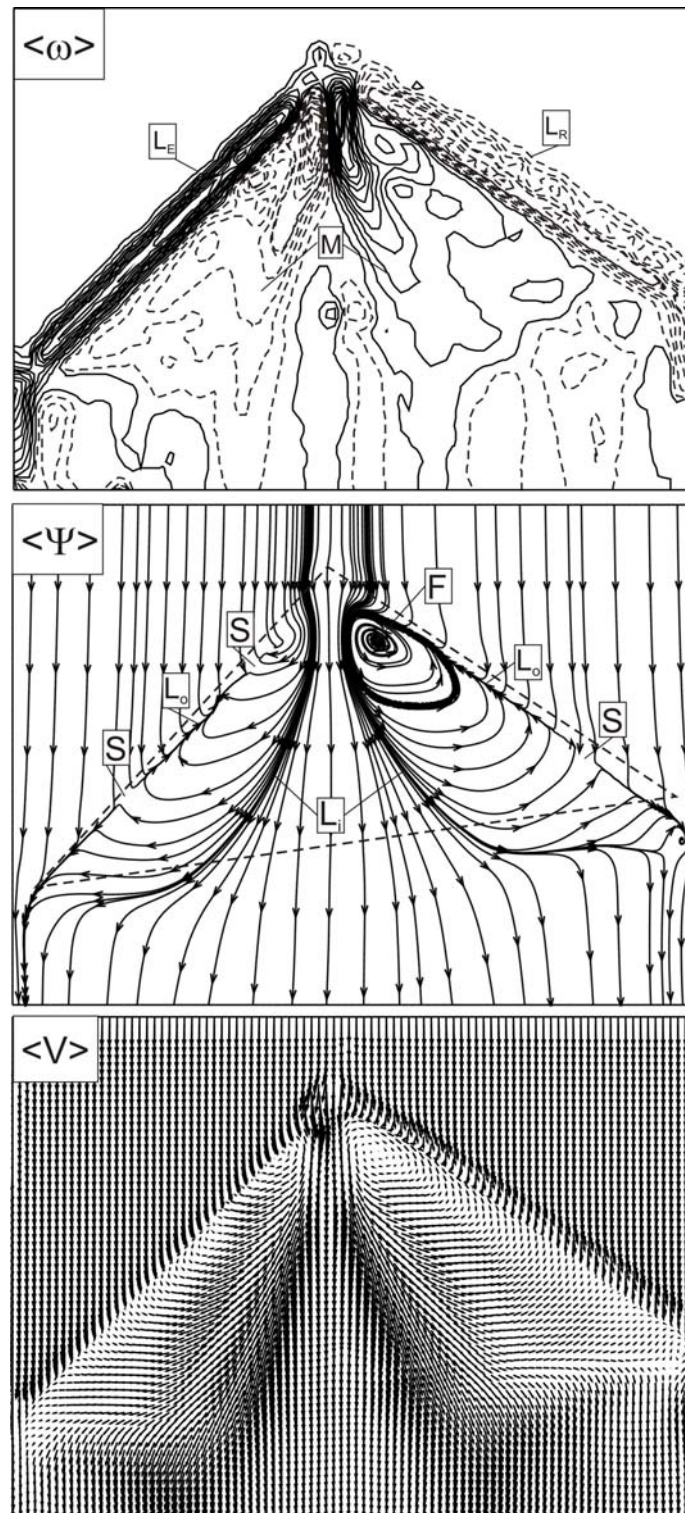


Figure 4.27. Patterns of time-averaged vorticity, $\langle \omega \rangle$, streamline, $\langle \Psi \rangle$, and distribution of velocity vectors, $\langle V \rangle$, for angle of attack $\alpha=10^\circ$, $\theta=8^\circ$. For contours of time-averaged vorticity, minimum and incremental values are $[\langle \omega \rangle]_{\min} = 0.4 \text{ s}^{-1}$ and $\Delta[\langle \omega \rangle] = 1 \text{ s}^{-1}$.

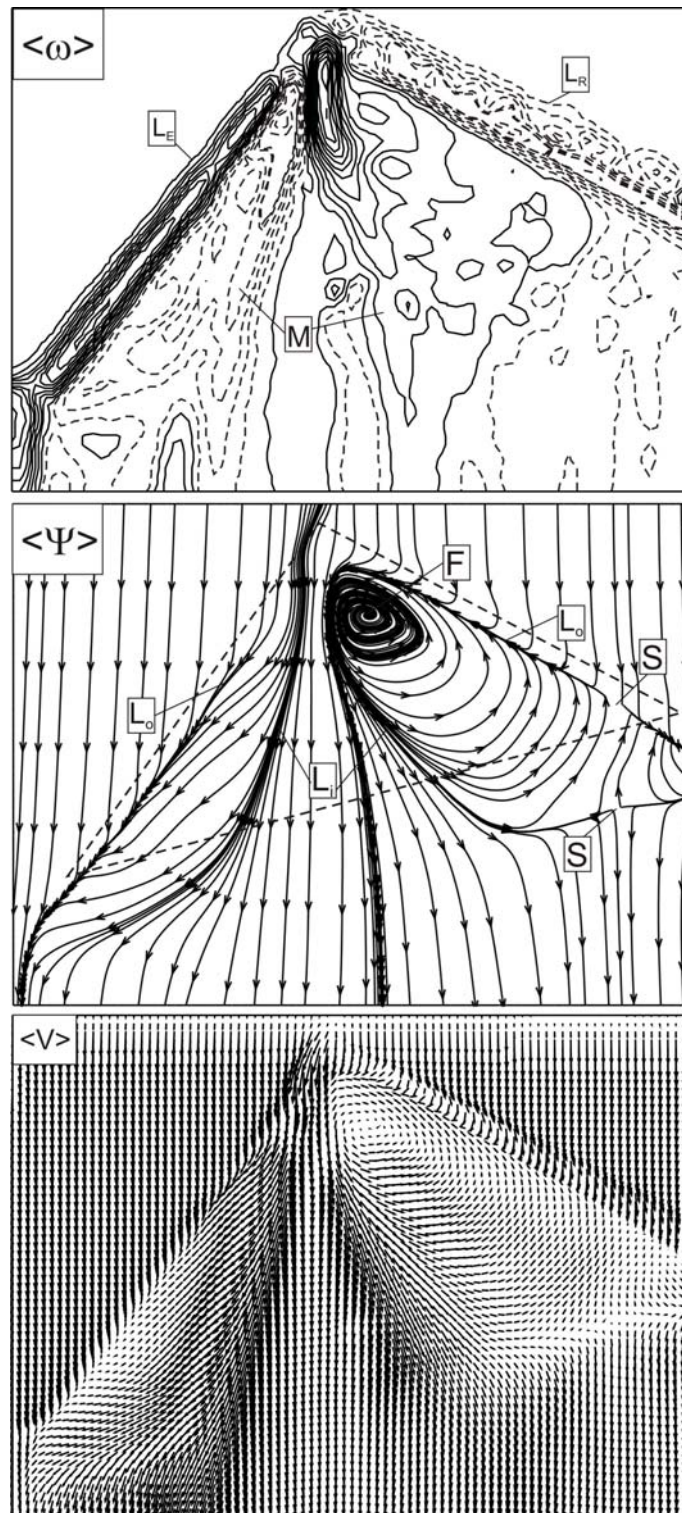


Figure 4.28. Patterns of time-averaged vorticity, $\langle \omega \rangle$, streamline, $\langle \Psi \rangle$, and distribution of velocity vectors, $\langle V \rangle$, angle of attack $\alpha=10^\circ$, $\theta=15^\circ$. For contours of time-averaged vorticity, minimum and incremental values are $[\langle \omega \rangle]_{\min} = 0.4 \text{ s}^{-1}$ and $\Delta[\langle \omega \rangle] = 1 \text{ s}^{-1}$.

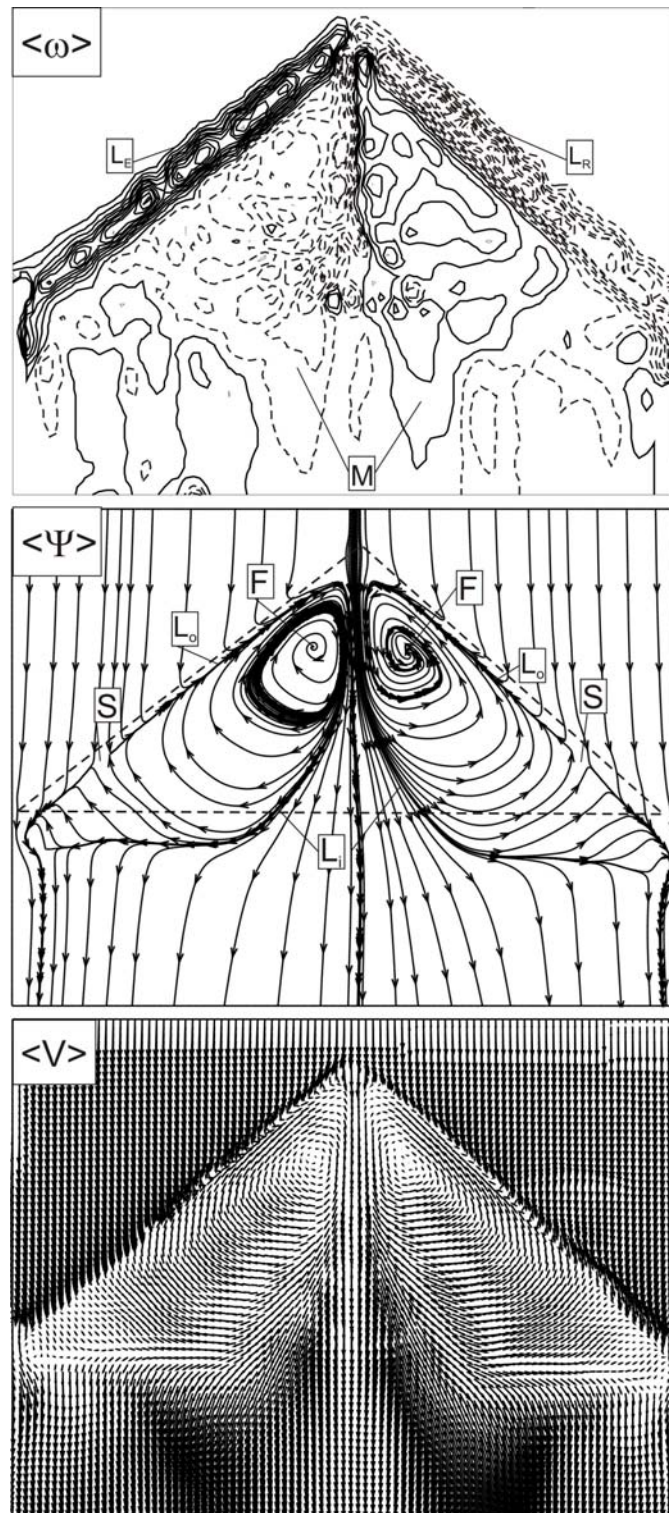


Figure 4.29. Patterns of time-averaged vorticity, $\langle \omega \rangle$, streamline, $\langle \Psi \rangle$, and distribution of velocity vectors, $\langle V \rangle$, for angle of attack $\alpha = 13^\circ$, $\theta = 0^\circ$. For contours of time-averaged vorticity, minimum and incremental values are $[\langle \omega \rangle]_{\min} = 0.4 \text{ s}^{-1}$ and $\Delta[\langle \omega \rangle] = 1 \text{ s}^{-1}$.

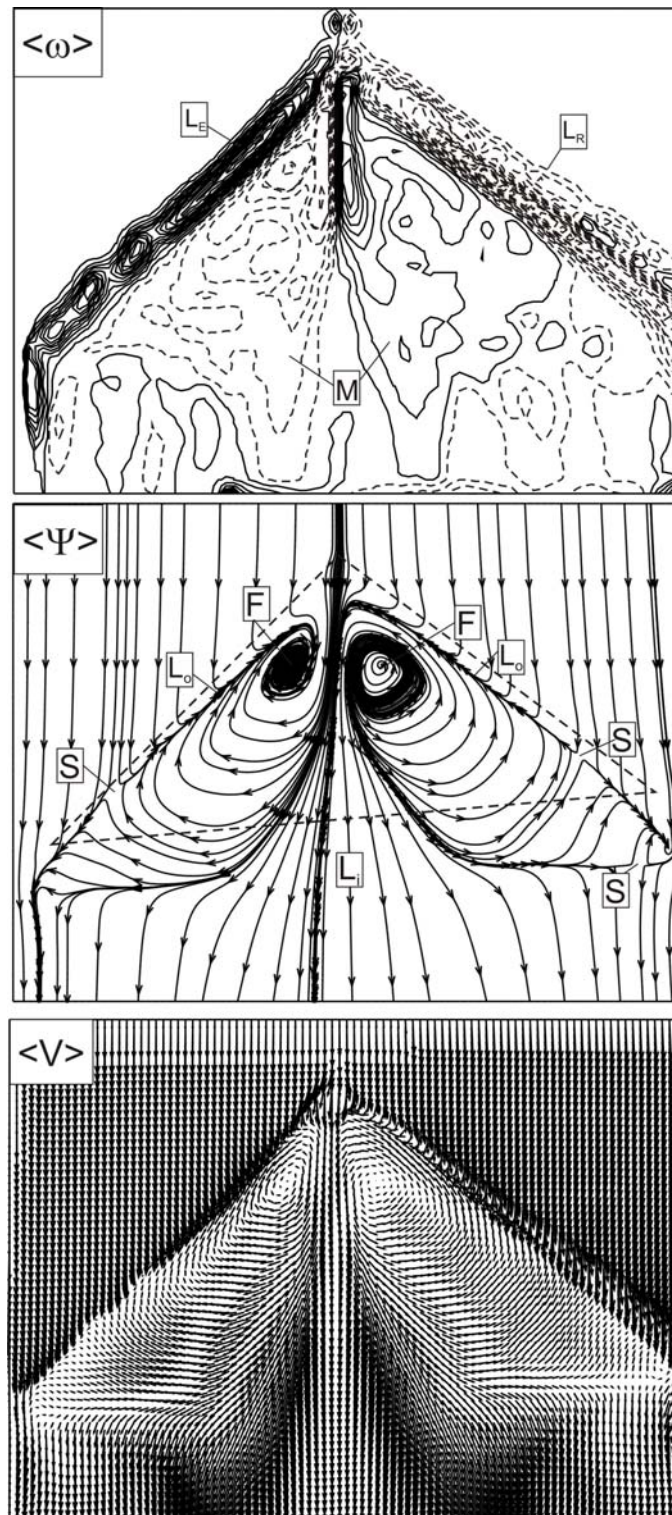


Figure 4.30. Patterns of time-averaged vorticity, $\langle \omega \rangle$, streamline, $\langle \Psi \rangle$, and distribution of velocity vectors, $\langle V \rangle$, for angle of attack $\alpha=13^\circ$, $\theta=6^\circ$. For contours of time-averaged vorticity, minimum and incremental values are $[\langle \omega \rangle]_{\min} = 0.4 \text{ s}^{-1}$ and $\Delta[\langle \omega \rangle] = 1 \text{ s}^{-1}$.

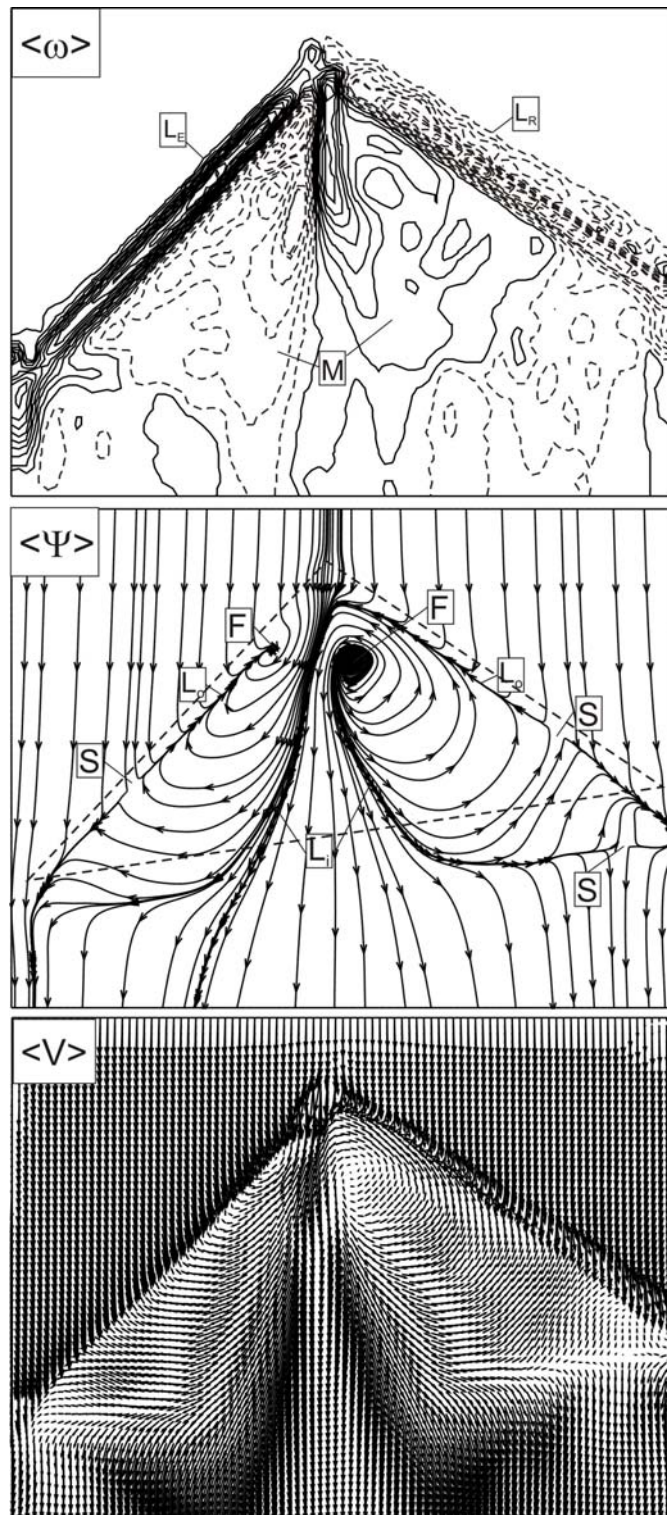


Figure 4.31. Patterns of time-averaged vorticity, $\langle \omega \rangle$, streamline, $\langle \Psi \rangle$, and distribution of velocity vectors, $\langle V \rangle$, for angle of attack $\alpha=13^\circ$, $\theta=8^\circ$. For contours of time-averaged vorticity, minimum and incremental values are $[\langle \omega \rangle]_{\min} = 0.4 \text{ s}^{-1}$ and $\Delta[\langle \omega \rangle] = 1 \text{ s}^{-1}$.

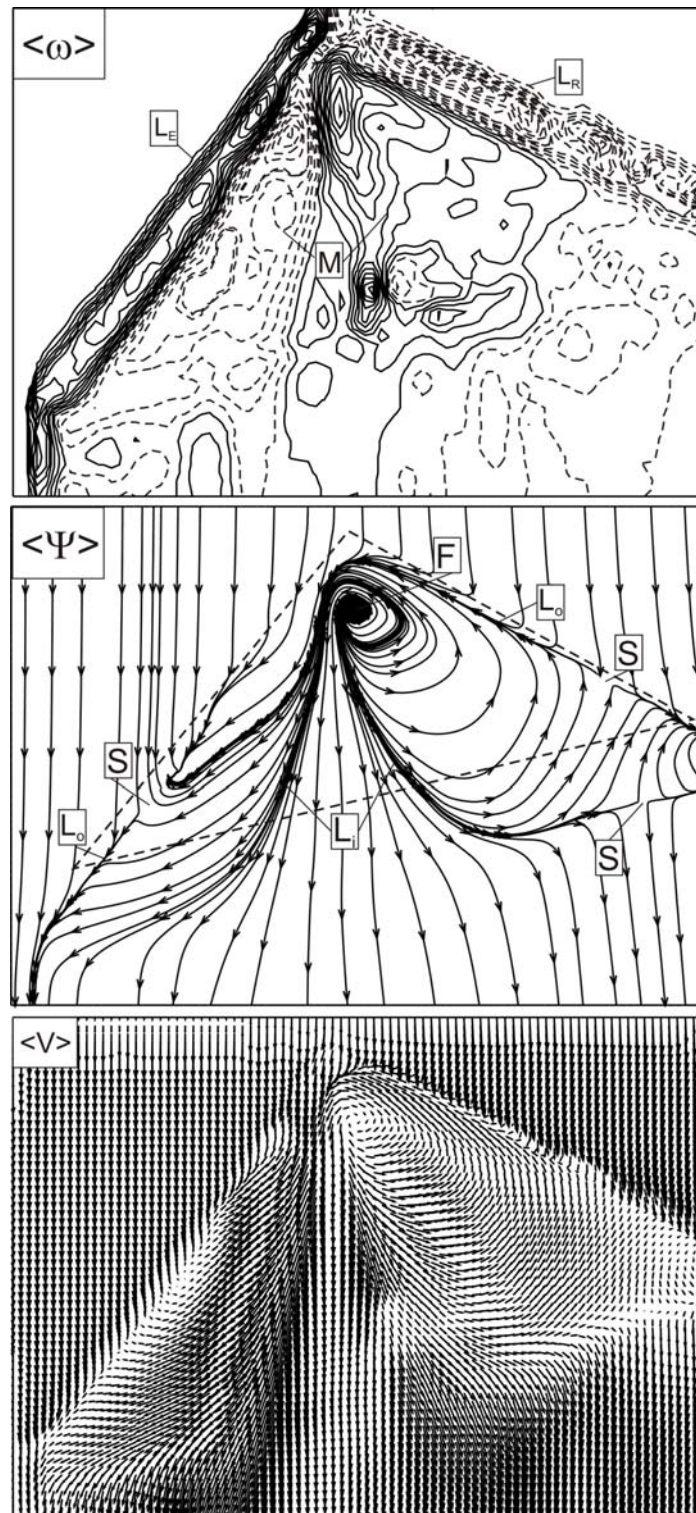


Figure 4.32. Patterns of time-averaged vorticity, $\langle \omega \rangle$, streamline, $\langle \Psi \rangle$, and distribution of velocity vectors, $\langle V \rangle$, for angle of attack $\alpha=13^\circ$, $\theta=15^\circ$. For contours of time-averaged vorticity, minimum and incremental values are $[\langle \omega \rangle]_{\min} = 0.4 \text{ s}^{-1}$ and $\Delta[\langle \omega \rangle] = 1 \text{ s}^{-1}$.

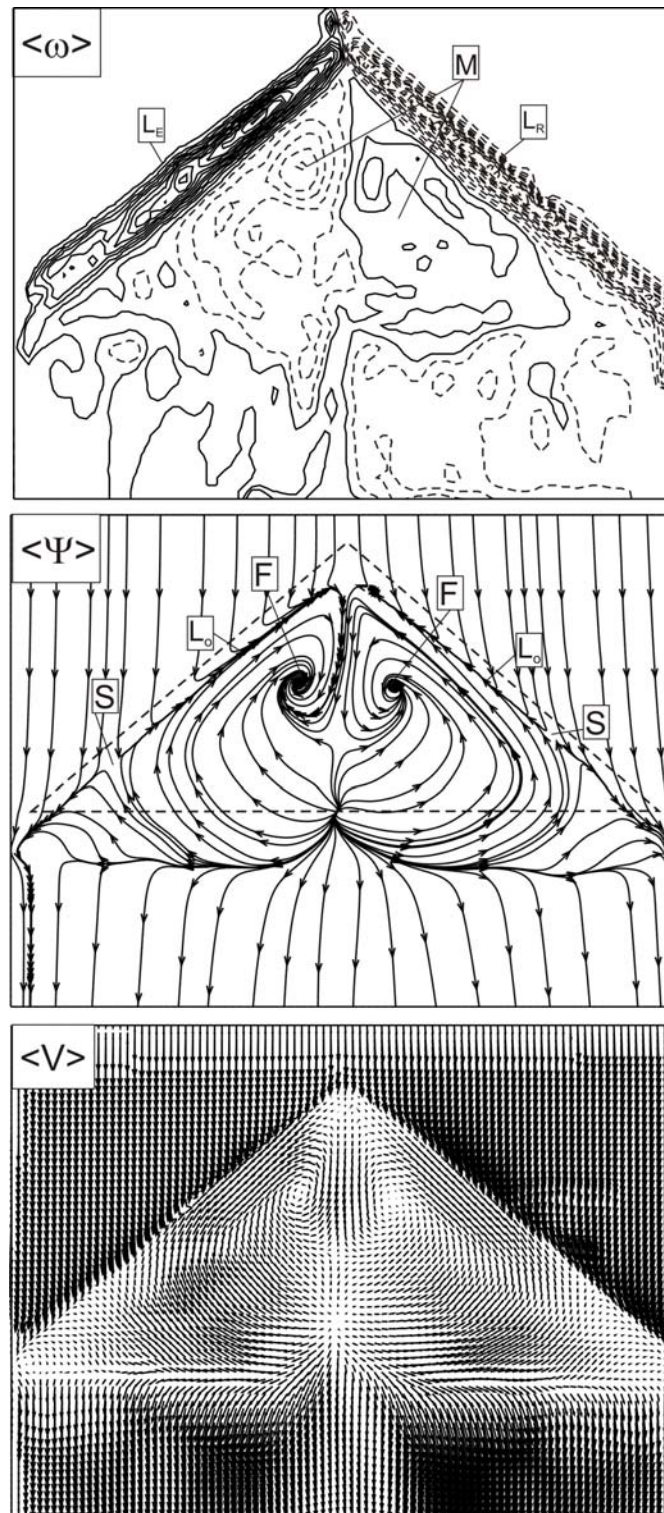


Figure 4.33. Patterns of time-averaged vorticity, $\langle \omega \rangle$, streamline, $\langle \Psi \rangle$, and distribution of velocity vectors, $\langle V \rangle$, for angle of attack $\alpha=17^\circ$, $\theta=0^\circ$. For contours of time-averaged vorticity, minimum and incremental values are $[\langle \omega \rangle]_{\min} = 0.4 \text{ s}^{-1}$ and $\Delta[\langle \omega \rangle] = 1 \text{ s}^{-1}$.

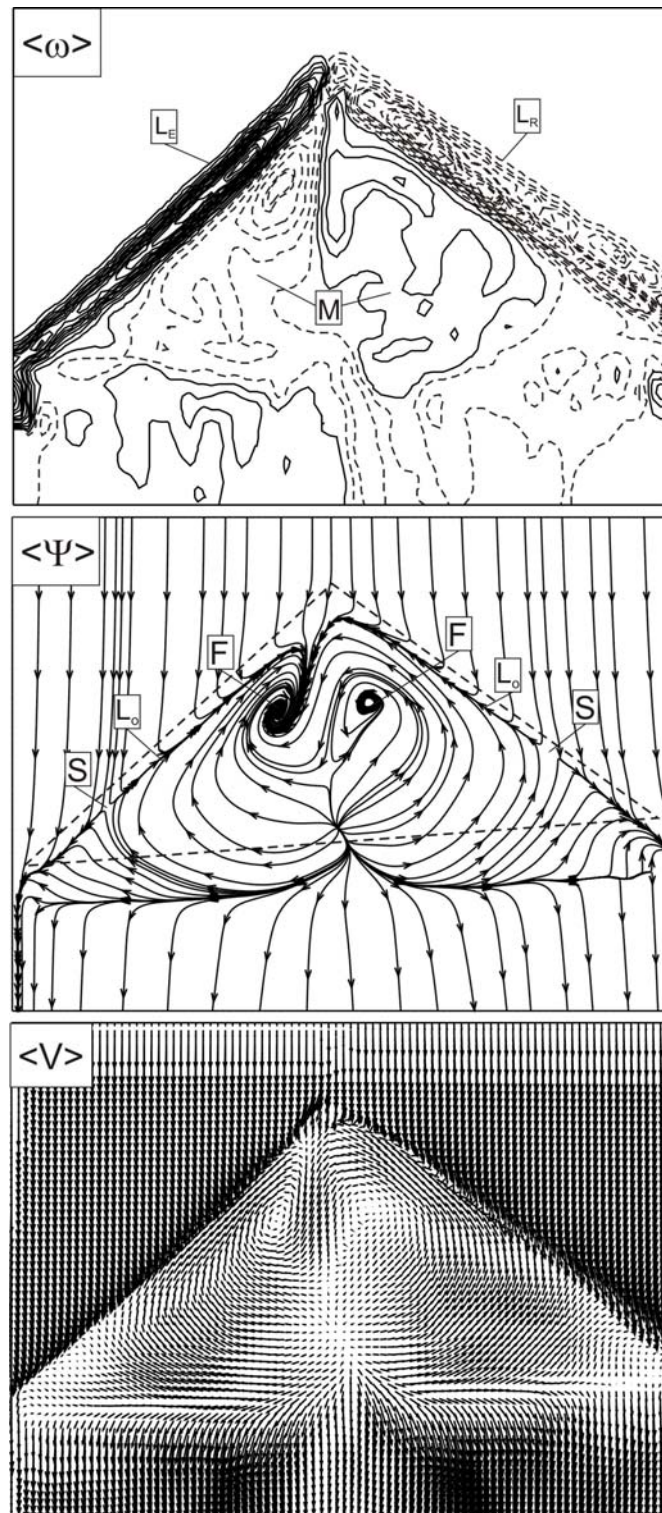


Figure 4.34. Patterns of time-averaged vorticity, $\langle \omega \rangle$, streamline, $\langle \Psi \rangle$, and distribution of velocity vectors, $\langle V \rangle$, for angle of attack $\alpha=17^\circ$, $\theta=6^\circ$. For contours of time-averaged vorticity, minimum and incremental values are $[\langle \omega \rangle]_{\min} = 0.4 \text{ s}^{-1}$ and $\Delta[\langle \omega \rangle] = 1 \text{ s}^{-1}$

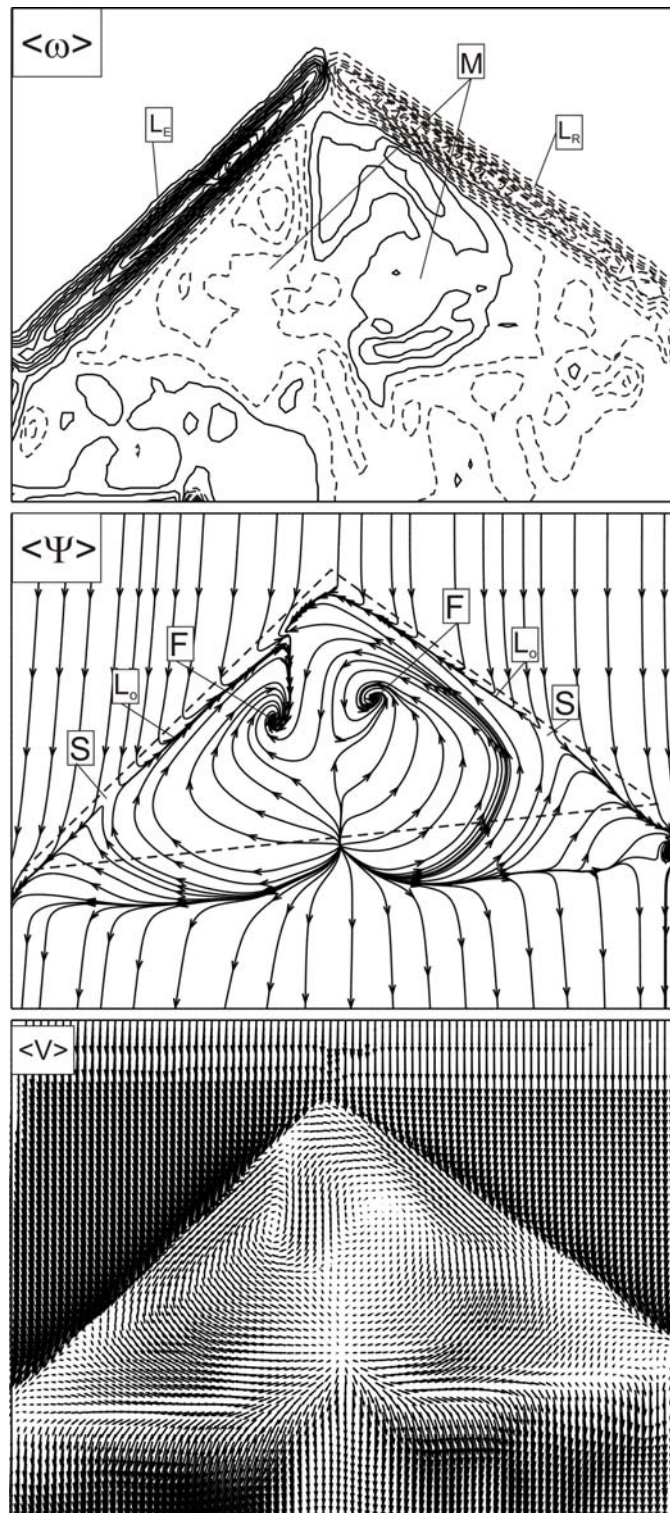


Figure 4.35. Patterns of time-averaged vorticity, $\langle \omega \rangle$, streamline, $\langle \Psi \rangle$, and distribution of velocity vectors, $\langle V \rangle$, for angle of attack $\alpha=17^\circ$, $\theta=8^\circ$. For contours of time-averaged vorticity, minimum and incremental values are $[\langle \omega \rangle]_{\min} = 0.4 \text{ s}^{-1}$ and $\Delta[\langle \omega \rangle] = 1 \text{ s}^{-1}$

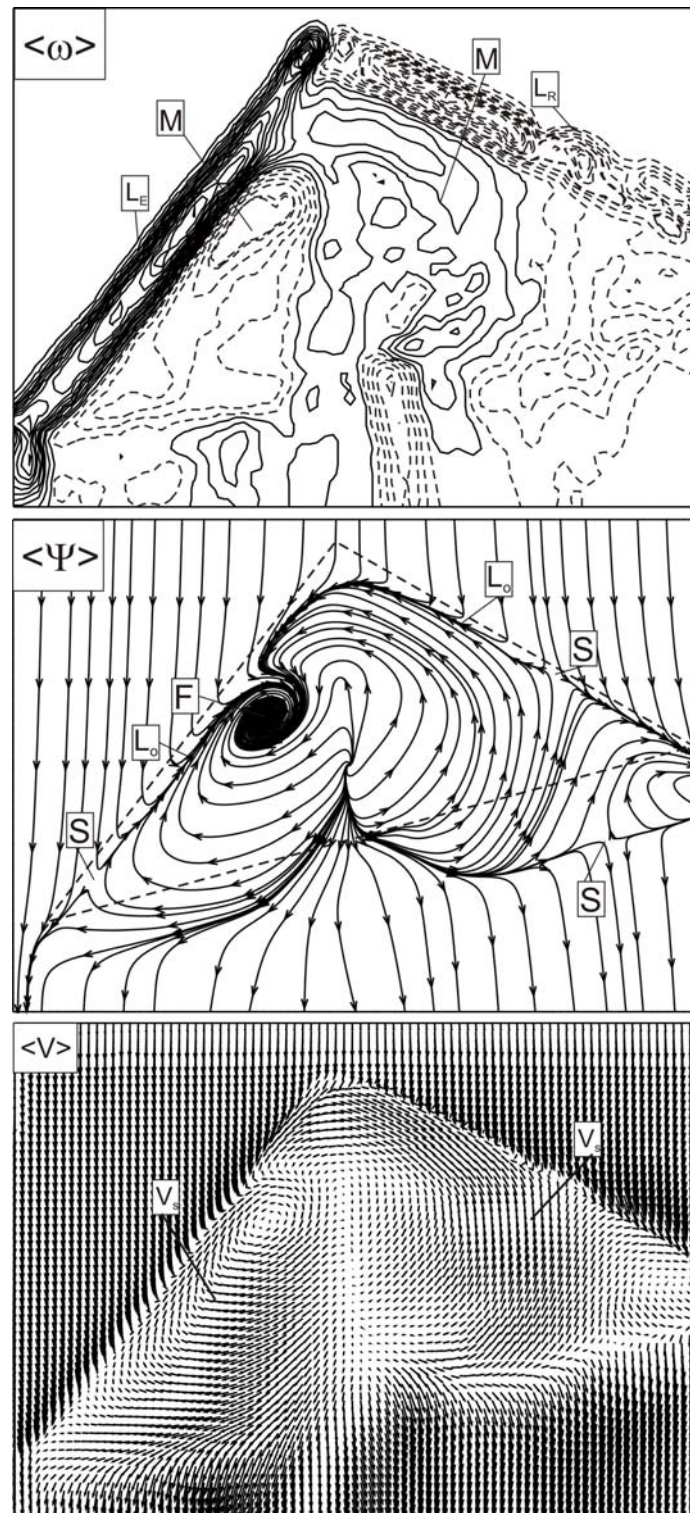


Figure 4.36. Patterns of time-averaged vorticity, $\langle \omega \rangle$, streamline, $\langle \Psi \rangle$, and distribution of velocity vectors, $\langle V \rangle$, for angle of attack $\alpha=17^\circ$, $\theta=15^\circ$. For contours of time-averaged vorticity, minimum and incremental values are $[\langle \omega \rangle]_{\min} = 0.4 \text{ s}^{-1}$ and $\Delta[\langle \omega \rangle] = 1 \text{ s}^{-1}$

4.1.2.3. Patterns of Time-Averaged Component of Transverse Velocity

Patterns of time-averaged component of transverse velocity for various angles of attack shown in Figures 4.37-40. The contours are represented by negative and positive $\langle v \rangle / U$. The positive and negative contours are demonstrated by solid and dashed lines, respectively. To be able to make a direct comparison between the minimum and incremental values of contours of time-averaged component of transverse velocity kept constant. The values of minimum and incremental values are $[\langle v \rangle / U]_{\min} = 0.03 \text{ s}^{-1}$ and $\Delta[\langle v \rangle / U] = 0.03 \text{ s}^{-1}$. There are two well-defined clusters of main positive and negative contours at both side of the delta wing chord axis. There is a symmetrical structure under delta wing surface in the case of zero yaw angles for all attack angles. While the delta wing is under effect of yaw angle, the distribution of $\langle v \rangle / U$ contours changes. At attack angle $\alpha = 7^\circ$ and yaw angle $\theta = 0^\circ$, there are two extrema at both side of the delta wing chord axis. Examining all images, the contours have an elongated form starting from leading edge of the delta wing. Also, there is a pair of contours at immediately downstream of the delta wing apex. They widen along the leading edge of delta wing and get stronger while angle of attack increases. As seen in Figure 4.38, at attack angle $\alpha = 7^\circ$ and yaw angle $\theta = 15^\circ$, the positive contours located immediately downstream of the delta wing apex unites with the main contours which rotates about positive direction. The extrema of positive and negative contours move further downstream in the free-stream flow direction while yaw angle increases at attack angle $\alpha = 10^\circ$. The main positively rotated contours do not unite with the positively rotated secondary contours located at immediately downstream of the delta wing apex, at attack angles $\alpha = 10^\circ, 13^\circ$ and 17° and yaw angle $\theta = 15^\circ$. As seen in Figure 4.41, the extrema of main positive and negative contours is located at outer region of the delta wing. Also, the secondary positively and negatively rotated time-averaged components of transverse velocity are evident near the leading edge of the delta wing. The extrema of the main positively and negatively rotated contours move through upstream direction as seen in Figure 4.39. At $\alpha = 17^\circ$, as seen in Figure 4.40, patterns of the time-averaged transverse velocity component shows that central point of primary transverse velocity component moves

further downstream of the trailing edge of the delta wing and have very complex distribution and positively and negatively secondary rotated contours get stronger comparing to the case of low angle of attack. The extrema of main contours are located at outer region of delta wing.

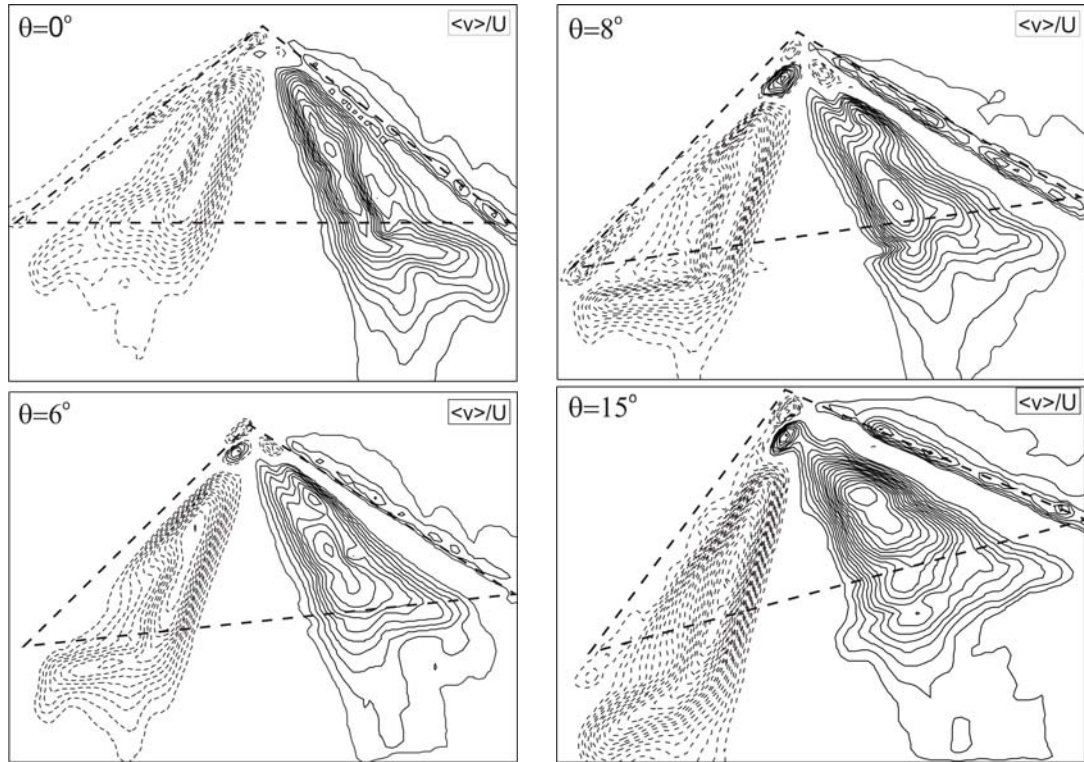


Figure 4.37. Patterns of time-averaged component of transverse, $\langle v \rangle / U$, velocity for attack angle $\alpha = 7^\circ$. Minimum and incremental values are $\langle v \rangle / U_{\min} = 0.03 \text{ s}^{-1}$ and $\Delta \langle v \rangle / U = 0.03 \text{ s}^{-1}$

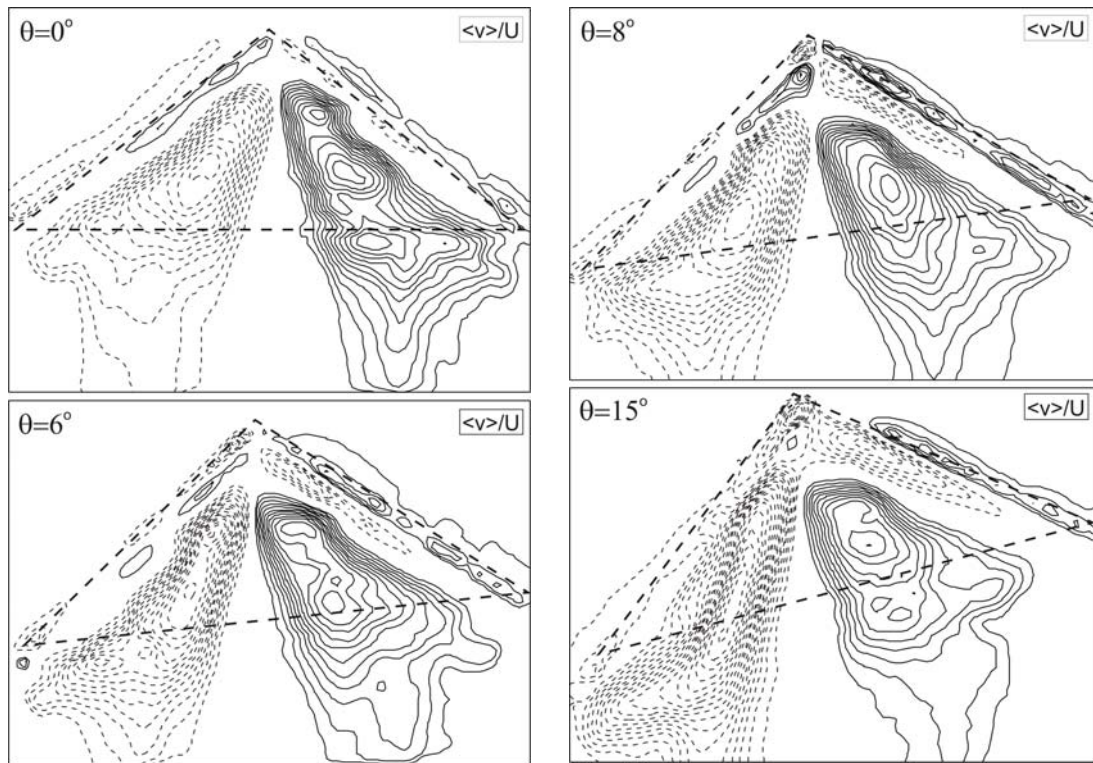


Figure 4.38. Patterns of time-averaged component of transverse velocity, $[\langle v \rangle / U]$, for attack angle $\alpha = 10^\circ$. Minimum and incremental values are $[\langle v \rangle / U]_{\min} = 0.03 \text{ s}^{-1}$ and $\Delta[\langle v \rangle / U] = 0.03 \text{ s}^{-1}$

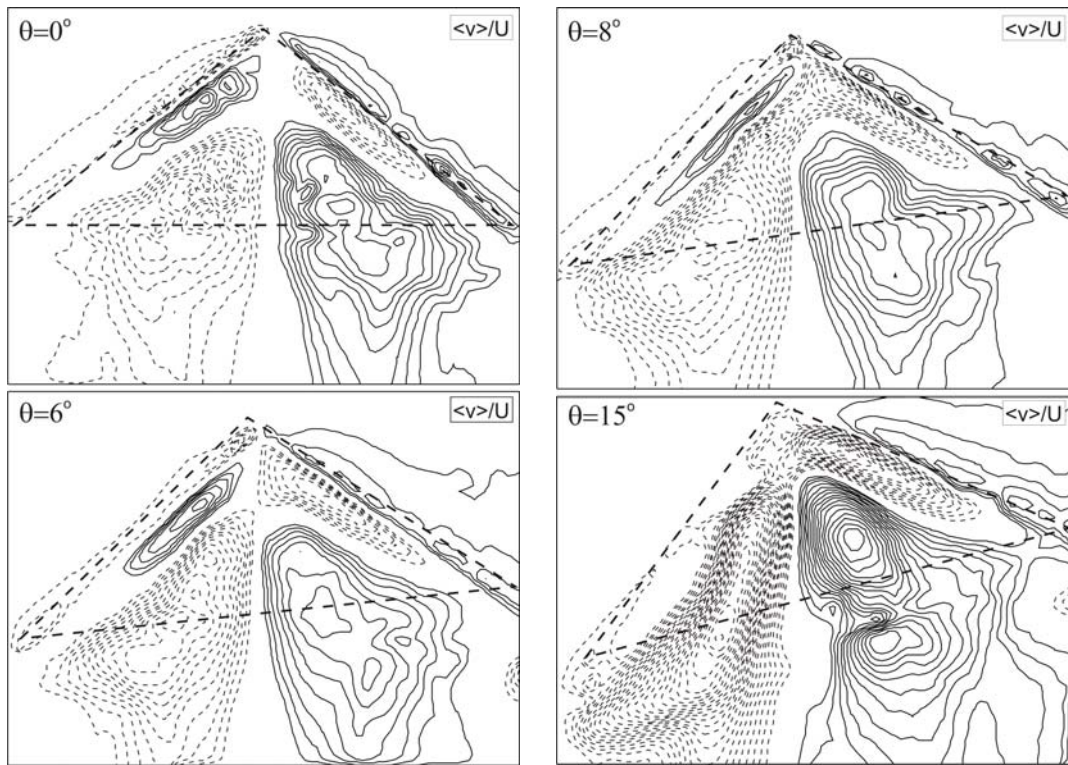


Figure 4.39. Patterns of time-averaged component of transverse velocity, $[\langle v \rangle / U]$, for attack angle $\alpha = 13^\circ$. Minimum and incremental values are $[\langle v \rangle / U]_{\min} = 0.03 \text{ s}^{-1}$ and $\Delta[\langle v \rangle / U] = 0.03 \text{ s}^{-1}$

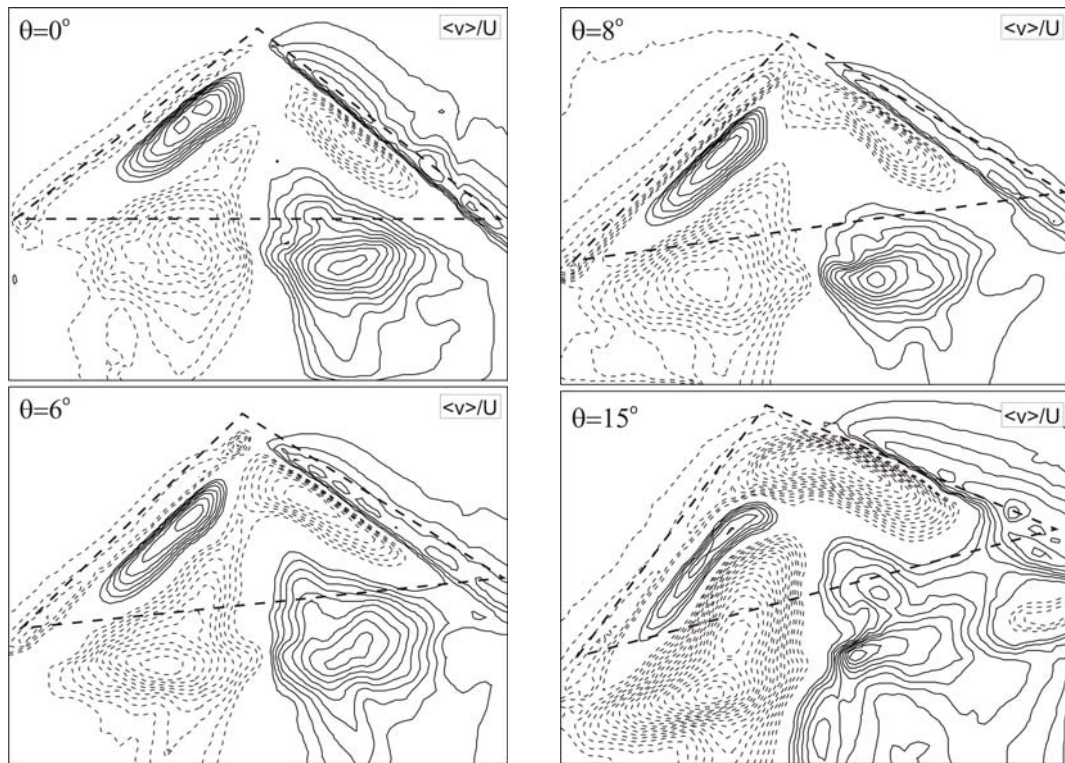


Figure 4.40. Patterns of time-averaged component of transverse velocity, $[\langle v \rangle / U]$, for attack angle $\alpha = 17^\circ$. Minimum and incremental values are $[\langle v \rangle / U]_{\min} = 0.03 \text{ s}^{-1}$ and $\Delta[\langle v \rangle / U] = 0.03 \text{ s}^{-1}$

5. CONCLUSIONS

The present investigation focuses on a fundamental phenomena, which are formation and development of leading-edge vortices, vortex breakdown and three dimensional separation and stall, of the complex and disorganized flow structure over the delta wing which have leading edge sweep angle $\Lambda=40^\circ$ investigated both qualitatively and quantitatively using dye visualization and the Particle Image Velicimetry (PIV) technique. Firstly, the flow structure in close region of the stationary delta wing, interaction of vorticity generated by vortex breakdown with the delta wing and formation of vortex breakdown were visualized by varying angle of attack within the range of $7^\circ \leq \alpha \leq 17^\circ$. Secondly, changes in flow structure were also observed varying yaw angle of the delta wing within the range of $0^\circ \leq \theta \leq 15^\circ$. Patterns of the time-averaged vorticity, $\langle \omega \rangle$, streamline, $\langle \Psi \rangle$, distribution of velocity vectors, $\langle V \rangle$, and corresponding transverse velocity component, $\langle v \rangle / U$, for various angles of attack and yaw angles were obtained in order to reveal the flow mechanism on plan-view plane adjacent to the surface of the wing and over the crossflow planes.

Examining all dye visualization experiments, there is a symmetrical flow structure on the delta wing in the case of zero yaw angle. Also, there is a pair of spiral vortices starting from the apex of the delta wing. The structure of these spiral vortices decomposes after a definite distance from the delta wing apex. This decomposition is called as “vortex breakdown”. The location of vortex breakdown moves in forward direction close to the leading edge of the delta wing when the attack angle increases along its central axis in unsteady mode. The flow structure of the delta wing becomes more complex and disorganized after occurrence of vortex breakdown. Examining all images, it can be seen that, high scale Kelvin-Helmoltz vortex structure occurs at the bottom of the unstable flow region, especially for the attack angles of $\alpha=13^\circ$ and 17° . When the delta wing is under effect of yaw angle, the symmetrical flow structure is corrupted and vortex breakdown occurs earlier at the upper side of the delta wing chord axis compared with the opposite side.

In the end-view plane [$X/C=0.8$], there is a symmetrical flow structure over the delta wing in the case of zero yaw angle. The patterns of the time-averaged vorticity have an elongated shape with two vorticity extrema under the zero yaw angle and attack angle of $\alpha=17^\circ$. In this case, there are three vorticity extrema. Generally, the elongated layer widens when yaw angle is increased as shown by time-averaged vorticity contours. The corresponding streamline topology indicates two saddle points, S_1 and S_2 , and foci, F_1 and F_2 . Saddle points, S_1 and S_2 , are appeared well below the foci, F_1 and F_2 . The streamline patterns exhibit a well defined swirl pattern. The centers of the foci never coincide with the maxima of the time-averaged vortices. The saddle points, S_1 and S_2 , and center of foci, F_1 and F_2 , gradually move downward and get closer to each other as angle of attack is increased.

On the plan-view plane, there is a pair of spiral vortices which emanate from the leading edge of the delta wing and two well-defined clusters of negative and positive time-averaged vorticity, $\langle\omega\rangle$, occur along the leading edge of the delta wing. These vortices have an elongated form which can also be seen from corresponding dye visualization experiments. A symmetrical flow structure dominates whole wing surface in the case of zero yaw angle. Also, there is a pair of vortices which are located at the middle region of the wing surface. These counter-rotating vortices are adjacent to the primary vortices. These middle vortices disappear as the attack angle increases. The symmetrical flow structure deteriorates when yaw angle increases. Generally, the streamline pattern, $\langle\Psi\rangle$, tends to be linear through its lengthwise direction at the opposite side of yawed side of the delta wing. The domain of the focus located at yawed side is increased as the yaw angle is increased. This situation causes the large low velocity region at yawed side of the delta wing, but this is not the case for the other side. At angle of attack $\alpha=17^\circ$, the separated flow region dominates the whole wing surface.

REFERENCES

- AKILLI, H., SAHIN, B. AND ROCKWELL, D., “Control of Vortex Breakdown by a Transversely-Oriented Wire”, *Physics of Fluids*, Vol.13, No.2, pp.452-463, 2001.
- ANDERSON, J.D., *Fundamentals of aerodynamics*. McGraw-Hill Higher Education, ISBN 0-07-118146-6, 2001.
- ATASHBAZ G., OMMIAN M., “Experimental Investigation of Vortex Flow over an 80 Degree/60 Degree Double Delta Wing at Sideslip”, *Journal of Aircraft* , Vol. 43, No. 3, 2006.
- BREITSAMTER C., “Unsteady flow phenomena associated with leading-edge vortices”, *Progress in Aerospace Sciences*, Vol.44, pp.48–65, 2008.
- CAI, J., LUO, S., AND LIU, F., “Stability of symmetric vortices in two dimensions and over three-dimensional slender conical bodies,” *Physics of Fluids*, Vol. 16, No. 2, Feb. 2003, pp. 424–432.
- “Stability of Symmetric and Asymmetric Vortices over Slender Conical Wing–Body Combinations,” *AIAA Journal*, Vol. 44, No. 7, July 2004, pp. 1601–1608.
- CAI J., TSAI H. M., LUO S., LIU F., “Stability of Vortex Pairs over Slender Conical Bodies: Analysis and Numerical Computation”, *AIAA JOURNAL*, Vol. 46, No. 3, 2008.
- CUI Y. D., LIM T. T., TSAI H. M., “Control of Vortex Breakdown over Delta Wing Using Freebody Slot Blowing”, *AIAA Journal*, Vol 45, No.1, 2007.
- “Freebody Slot Blowing on Vortex Breakdown and Load Over a Delta Wing”, *AIAA Journal*, Vol 46, No.3, 2008.

DANTEC DYNAMICS v4.71 Flowmap Software Manual.

DEGANI, D., “Effect of Geometrical Disturbance on Vortex Asymmetry,” AIAA Journal, Vol. 29, No. 4, pp. 560–566, 1991.

———“Instabilities of Flows over Bodies at Large Incidence,” AIAA Journal, Vol. 30, No. 1, pp. 94–100, 1992.

DEGANI, D., AND TOBAK, M., “Experimental Study of Controlled Tip Disturbance Effect on Flow Asymmetry,” Physics of Fluids A, Vol. 4, No. 12, pp. 2825–2832, 1992.

DELERY, J. M., “Aspects of Vortex Breakdown”, Progress in Aerospace Sciences, Vol. 30, pp. 1-59, 1994.

ERICKSON, G.E., Schreiner, J. A., and Rogers, L. W., “On the Structure, Interaction, and Breakdown Characteristics of Slender Wing Vortices at Subsonic, Transonic, and Supersonic Speeds,” AIAA ,1989-3345, 1989.

ERICSSON, L.E., Challenges in high-alpha vehicle dynamics, Prog. Aerospace Sci. Vol.31, pp.291-334, 1995.

ELKHOURY, M. AND ROCKWELL, D., “Visualized Vortices on Unmanned Combat Air Vehicles Planform: Effect of Reynolds Number. Journal of Aircraft”, Vol. 41, No. 5, pp. 1244-1246, 2004.

ELKHOURY, M., YAVUZ, M. M. AND ROCKWELL, D., “Near-Surface Topology of a Unmanned Combat Air Vehicles Planform: Reynolds Number Dependence”, Journal of Aircraft, Vol. 42, No. 5, September/October, 2005, 1318-1330, 2005.

- GHEE T. A., TAYLOR N. J., “Low-Speed Wind Tunnel Tests on a Lambda Wing High-Lift Configuration” , 22nd Applied Aerodynamics Conference and Exhibit, Providence, Rhode Island; AIAA 2004-4843, 2004.
- GONG N. I., JIEKE L. U., DINGDING XIN., “Two Optical Techniques Appropriate for Visualizing the Steady/Unsteady Vertical Flow past a Highly Swept Delta-Wing Equipped with Double Vortex-Flaps in Low and High Speed Wind-Tunnel”, *Communications in Nonlinear Science & Numerical Simulation* Vol.3, No.3 , Sep. 1998.
- GURSUL, I. AND YANG, H., “On Fluctuations of Vortex Breakdown Location”, *Physics of Fluids*, Vol. 7, No. 1, January, pp. 229-231, 1995.
- GURSUL, I., TAYLOR, G., AND WOODING, C. L., “Vortex Flows over Fixed-Wing Micro Air Vehicle”, AIAA Paper 0648 2002.
- GURSUL I., “Review of Unsteady Vortex Flows over Slender DeltaWings” *Journal of Aircraft*, Vol. 42, No. 2, 2005.
- GURSUL, I., GORDNIER, R. AND VISBAL, M., “Unsteady aerodynamics of nonslender delta wings”, *Progress in Aerospace Sciences* 41, pp.515–557 2005.
- HONKAN, A., AND ANDREOPOULOS, J., 1997. Instantaneous Three-Dimensional Vorticity Measurements in Vortical Flow over a Delta Wing. *AIAA Journal*, Vol. 35, No. 10, October, 1997, pp. 1612-1620.
- KEGELMAN, J., AND ROOS, F., “Effects of Leading-Edge Shape and Vortex Burst on the Flow Field of a 70 Degree Sweep Delta Wing,” AIAA, 89-0086, Jan. 1989.

- KONRATH R., KLEIN C., SCHRÖDER A., KOMPENHANS J., “Combined application of pressure sensitive paint and particle image velocimetry to the flow above a delta wing”, *Exp. Fluids*, Vol. 44, pp. 357–366 ,2008.
- LEVY, Y., HESSELINK, L., AND DEGANI, D., “Systematic Study of the Correlation Between Geometrical Disturbances and Flow Asymmetries,” *AIAA Journal*, Vol. 34, No. 4, pp. 772–777, 1996.
- OL, M. V., AND GHARIB, M., “The Passage Toward Stall of Nonslendar Delta Wings at Low Reynolds Number.” *AIAA Paper 2001-2843*, 2001.
- “Leading-Edge Vortex Structure of Nonslender Delta Wings at Low Reynolds Number” *AIAA JOURNAL*, Vol. 41, No. 1, 2003.
- OZGOREN, M., SAHIN, B., AND ROCKWELL, D., “Vortex Structure on a Delta Wing at High Angle-of-Attack”, *AIAA Journal*, Vol.40, No.2, pp.285-292, 2002.
- PAYNE FM, NG TT, NELSON RC, SCHIFF LB. Visualisation and wake surveys of vortical flow over a delta wing. *AIAA* , Vol.26, No.2, pp.137-43, 1988.
- PIDD, M., AND SMITH, J. H. B., “Asymmetric Vortex Flow over Circular Cones,” *Vortex Flow Aerodynamics*, AGARD AGARD-CP-494, Neuilly sur Seine, France, July 1991, pp. 18–1–11.
- RILEY, A. J., AND LOWSON, M. V., Development of a Three-Dimensional Free Shear Layer. *Journal of Fluid Mechanics*, Vol. 369, pp. 49-89, 1998.
- SAHIN, B., AKILLI, H., LIN, J.-C. AND ROCKWELL, D., “Vortex breakdown edge ineraction: consequence of edge oscillations”, *AIAA Journal*, Vol. 39, No.55, 865-876, 1999.

- SARPKAYA, T., "On Stationary and Traveling Vortex Breakdowns", *Journal of Fluid Mechanics*, Vol. 45, No. 3, pp. 545-559, 1971.
- "Turbulent vortex breakdown, *Physics of Fluids*, 10:2301-2303, 1995.
- SHIH, C., AND DING, Z., "Unsteady Structure of Leading-Edge Vortex", *Flow over a Delta Wing*," AIAA Paper 96-0664, 1996.
- SOHN, M. H., LEE, K. Y., AND CHANG, J. W., *Vortex Flow Visualization of a Yawed Delta Wing with Leading-Edge Extension. Journal of Aircraft*, Vol. 41, No. 2, 2004.
- TAYLOR, G. S., SCHNORBUS, T., AND GURSUL, I., "An Investigation of Vortex Flows over Low Sweep Delta Wings", AIAA-2003-4021, AIAA Fluid Dynamics Conference, 23-26 June, Orlando, FL, 2003.
- TAYLOR, G.S., GURSUL, I., *Buffeting flows over a low-sweep delta wing. AIAA Journal*, Vol. 42, No. 9, 2004.
- YANIKTEPE B. AND ROCKWELL D., "Flow Structure on a Delta Wing of Low Sweep Angle" *AIAA JOURNAL*, Vol. 42, No. 3, March 2004.
- "Flow Structure on Diamond and Lambda Planforms:Trailing-Edge Region" *AIAA JOURNAL*, Vol. 43, No. 7, 2005.
- YANIKTEPE B. "Origin and Control of vortex breakdown of unmanned combat air vehicles" Ph. D. Thesis, pp.3, 2006.
- YAVUZ, M., ELKHOORY, M., and Rockwell, D., "Near-Surface Topology and Flow Structure on a Delta Wing", *AIAA Journal*, Vol. 42, No. 2, pp. 332-340, 2004.
- WOODS M. I., WOOD N. J., "Aerodynamic Characteristics of Lambda Wings", *The Aeronautical Journal*, Vol. 104, No.1034, pp. 165-174, 2000.

CURRICULUM VITAE

Çetin CANPOLAT graduated from Daniřment Gazi Anatolian High School in Adana in 2002. Same year, he enrolled in Mechanical Engineering Department of Çukurova University in Adana. He graduated from the department of Mechanical Engineering in 2006 and began his Master of Science. Presently, he takes in a TUBITAK Project.

APPENDIX

3D stereo PIV measurements are based on the same fundamental principles as human eye-sight; i.e. stereo vision. “When we look at a given object, our left and right eyes see two similar but not identical images. The brain compares the two images and interprets the slight variations to re-build the 3-dimensional information of the object observed.” Similarly, Stereo-PIV system measures particles displacements using two CCD/CMOS Cameras (Dantec Dynamics Software Manual):

- Each camera plays the role of the human eye, looking at the flowfield from different angles.
- The software plays the role of the brain, relating the observed (2x2D) displacements to 3D displacements.

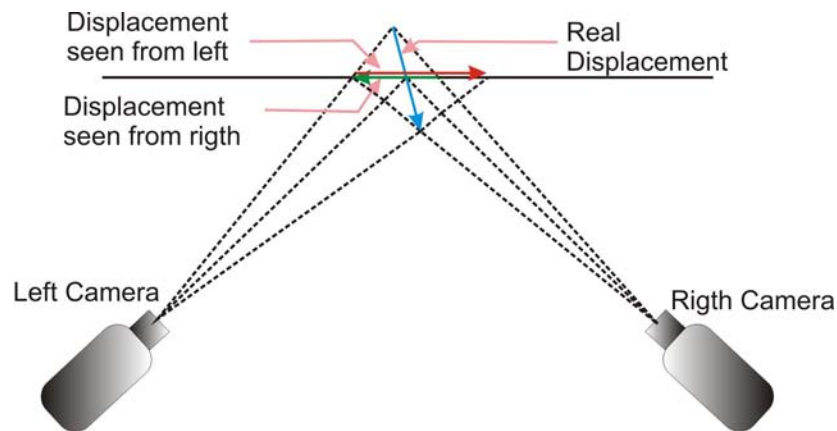


Figure 1. Principle of stereo-vision.

Mathematically, the most accurate determination of particles displacements (and thereby velocities) is obtained when the angle between the two cameras is set to 90° . In the case of a restricted optical access, stereoscopic imaging at smaller angles has been demonstrated at the cost of a somewhat reduced accuracy. Further, experience indicates that excellent 3D stereo PIV measurements can also be performed with camera viewing angles of $\pm 30^\circ$. In practice, the two camera views are calibrated by

recording images of a calibration target and fitting an imaging model on the top of the records. This calibration target contains markers with well-defined (X, Y, Z)-positions/coordinates and the model parameters are calculated by comparing the positions of these markers on each camera images (Dantec Dynamics Software Manual).

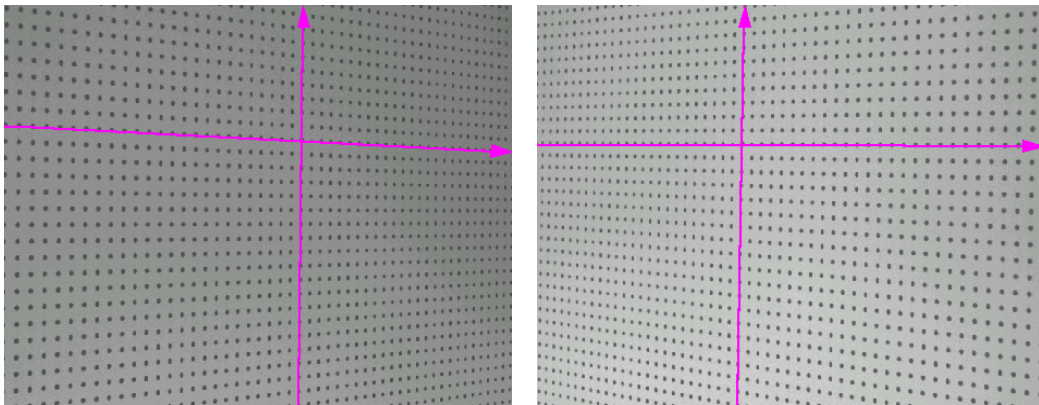


Figure 2. Example of calibration images recorded from camera 1 and camera 2.

Stereo-measurements start with conventional 2D PIV processing of PIV images recorded (simultaneously) with the two cameras. This produces two 2D vector maps representing the instantaneous flowfield as seen from the cameras. Using the camera view calibrations calculated earlier, these two 2D vector maps are then combined into one single 3D vector map. Due to perspective distortion, each camera covers a trapezoidal region of the light sheet. This means only partial overlap (see Figure 3.9) is obtained when recombine the camera views for 3D-PIV data calculations (Dantec Dynamics Software Manual).

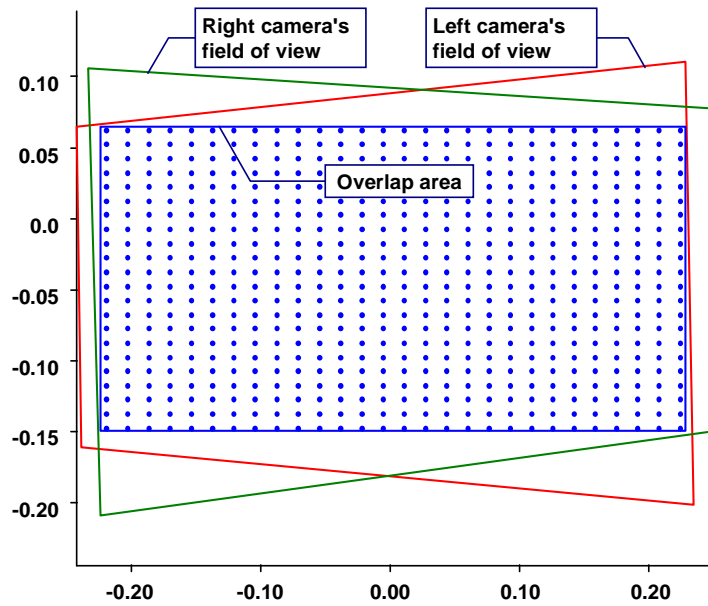


Figure 3. Overlapping fields of view.

Within this region of overlap, interrogation points are chosen in a rectangular grid. In principle 3D calculations can be performed on an infinitely dense grid. In practice, however, the 2D results have limited spatial resolution, and using a very dense grid for 3D evaluation will not improve the fundamental spatial resolution of the technique. Beside, this will considerably reduce the accuracy of particle displacement identification and thereby raw 2D-velocity determination (Dantec Dynamics Software Manual).

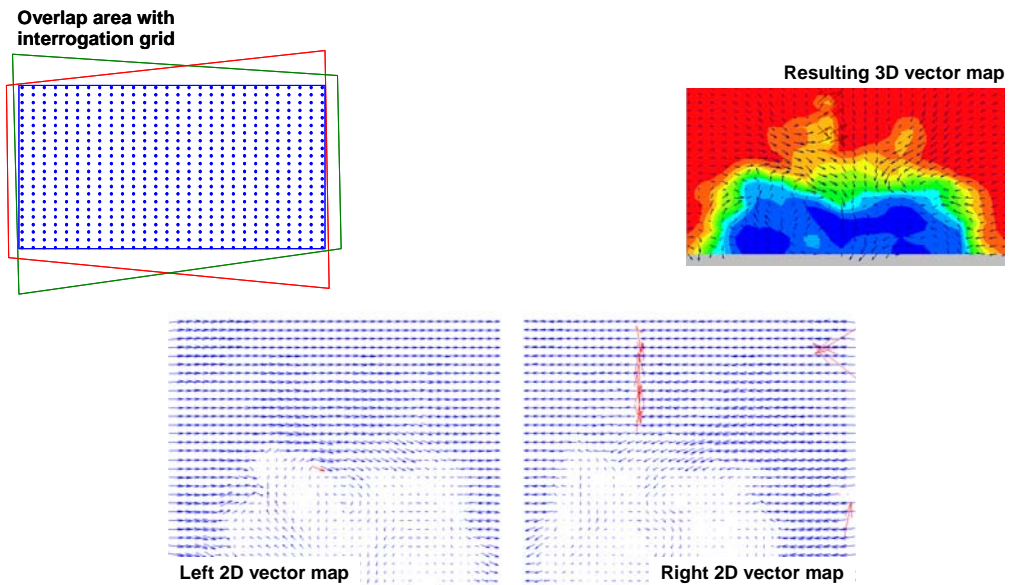


Figure 4. 3D PIV data reconstruction (Dantec Dynamics Software Manual).

To enforce the Scheimpflug condition (which requires that the object plane, the lens plane and the image plane are collinear) a special camera mount is required. In principle, the two cameras point at the calibration target at an optional angle. Both have one CCD/CMOS tilt axis and in this plane the Scheimpflug condition is satisfied and the cameras are tilted according to the object-plane or calibration target (Dantec Dynamics Software Manual).

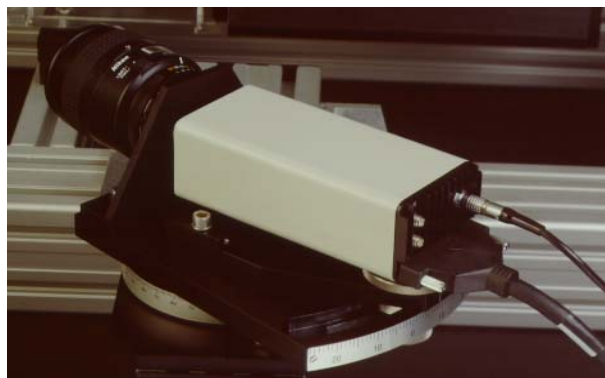


Figure 5. Scheimpflug condition camera plane.

The calibration uses a well defined grid of dots usually mounted on a traverse system. The calibration target is aligned with the light sheet and normally traversed through the light sheet in several positions. The dots on the calibration target are used to calculate linear or higher order calibration equations for each camera. The linear calibration compensates for differences in scale and lack of orthogonality while higher order calibration equations compensate for non-linear distortions like radial and barrel distortion (Dantec Dynamics Software Manual).

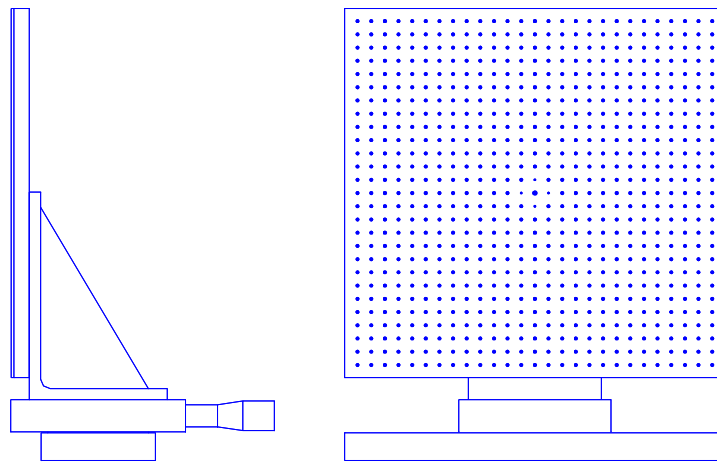


Figure 6. Standard calibration target mounted on traverse.